



## End of Summer REU Symposium

**Thursday, August 3, 2023, 10:00 am – 12:00 pm (CST)**

**In Person:** Whitaker Hall, Room 100

**or Virtual:** [Zoom Link](#) (Meeting ID 946 3273 8759, Passcode: 471834)

**10:00 am - 10:15 – Welcoming Remarks**

Ram Dixit, PhD, CEMB Associate Director of Education

Patricia Widder, CEMB Education Program Coordinator and Senior Lecturer in Biomedical Engineering

**10:15 am - 10:30 am – Emily Chen, Washington University in St. Louis**

Jessica Wagenseil Lab

*“Preventative and Restorative Effects of Epigallocatechin Gallate (EGCG) on Mechanical Behavior Associated with Elastic Fiber Fragmentation in the Mouse Ascending Aorta”*

[Abstract](#) | [Poster](#)

**10:30 am - 10:45 am – Maya Evohr, Worcester Polytechnic Institute**

Nathaniel Huebsch Lab

*“3D Printed System for Simultaneous Stretch and Imaging of Engineered Microtissues”*

[Abstract](#) | [Poster](#)

**10:50 am - 11:05 am – Calvin Paulsen, Clemson University**

Amit Pathak Lab

*“Novel 3D Ex-Vivo Model for Delivering Radial Compressive Stress”*

[Abstract](#) | [Poster](#)

**11:05 - 11:15 – Break**

**11:15 am - 11:30 am – Daichi Kobayashi, Washington University in St. Louis**

Marcus Foston Lab

*“Effects of Magnetic Field-Induced Alignment on Cellulose Nanocrystal and Soy Protein Nanocomposite Mechanical Properties”*

[Abstract](#) | [Poster](#)

**11:30 am - 11:45 am – Alexandra Perez, University of Puerto Rico - Mayagüez**

Guy Genin Lab

*“Flow fields in connector based vascular anastomosis”*

[Abstract](#) | [Poster](#)

**11:45 am - 12:00 pm – Nathalia Liu-DeRestrepo, University of Puerto Rico-Cayey**

Hani Suleiman Lab

*“Unraveling the Role of Formins in Podocyte Dynamics and Function”*

[Abstract](#) | [Poster](#)



**12:00 - 12:10 – Closing Remarks**

Ram Dixit, PhD, CEMB Associate Director of Education

Patricia Widder, CEMB Education Program Coordinator and Senior Lecturer in Biomedical Engineering

*Lunch and beverages will be available afterwards in Green Hall, 2<sup>nd</sup> Floor Collaboration Space Lounge.* Snacks and beverages will be available during the symposium on the table outside of Whitaker 100 in the Whitaker Hall atrium.

# **Preventative and Restorative Effects of Epigallocatechin Gallate (EGCG) on Mechanical Behavior Associated with Elastic Fiber Fragmentation in the Mouse Ascending Aorta**

Dongfang E. Chen<sup>1</sup>, Aidan O'Scannlain<sup>1,2</sup>, and Jessica E. Wagenseil<sup>1</sup>

Washington University in St. Louis<sup>1</sup>, and the University of Notre Dame<sup>2</sup>

## **Introduction**

Thoracic aortic aneurysm (TAA) is a prominent health concern affecting 5.3 per 100,000 people/year. It is characterized by aortic dilation that can lead to aortic dissection and death in patients. A main contributor to TAAs are defects in the extracellular matrix, specifically, the elastic fibers. Previous research shows that TAA-linked genetic mutations affect pathways involved in elastic fiber formation and cross-linking. A common histopathological finding in TAAs is elastic fiber fragmentation. Elastic fibers are essential to the aorta as they provide the elastic properties that allow the aorta to respond to large pressure and volume changes.<sup>2</sup> Despite its prevalence, there are limited effective drug therapy treatments to prevent or restore mechanical changes associated with TAA<sup>1</sup>.

Epigallocatechin gallate (EGCG) is a plant-based polyphenol that binds to extracellular matrix protein. It has been shown to attenuate abdominal aortic aneurysm (AAA) progression in a rat model.<sup>4</sup> Polyphenols including EGCG and pentagalloyl glucose (PGG) are listed as a cross-linking agent for collagen.<sup>3</sup> It is potentially useful in treating TAA by stabilizing the extracellular matrix. EGCG has not been tested in TAA models and the mechanical effects of the drug on the vessel wall are unknown. PGG was tested previously and showed potential as a treatment option as it prevented and restored mechanical properties after elastic fiber degradation.<sup>2</sup> Based on the PGG results, we hypothesize that EGCG, in a chemical TAA model, can restore and/or prevent mechanical changes caused by elastic fiber fragmentation.

## **Materials and Methods**

3–4 month-old male C57BL6/J mice were euthanized by carbon dioxide inhalation in compliance with the Institutional Animal Care and Use Committee. Ascending thoracic aortas (ATAs) were dissected and mounted on a pressure myograph system (DMT) for biaxial mechanical testing. Each ATA served as its own untreated (UNT) control. ATAs were subject to 3 axial stretch-controlled tests while varying pressure and 3 pressure-controlled tests while varying axial stretch ratio. Data for pressure, outer diameter, axial stretch, and axial force were recorded. Compliance was calculated as the change in diameter for each 15 mmHg pressure step. UNT (N=17) were tested and placed into treatment groups (N=3-5). Elastase was used to simulate the elastic fiber degradation associated with TAAs. A pilot study determined the optimal concentration and timing for ELA and EGCG treatments. For ELA treatment, 7.5 U/ml of ELA was applied for 6 minutes followed by 100 mM of NaCl for 6 minutes to neutralize the ELA. For EGCG treatment, 2.0 mg/ml of EGCG was applied for 30 minutes. Treatments were delivered through the aortic lumen and held at 100 mmHg to mimic clinical treatment methods. The four treatment groups included ELA, EGCG, EGCG+ELA (preventative), and ELA+EGCG (restorative). After treatment, the mechanical properties of the ATAs were tested again. The

unloaded dimensions were measured post-testing by imaging cross-sectional cut rings of the ATA.

## **Results, Conclusions, Discussions**

Single-factor ANOVA tests show significant differences ( $p < 0.05$ ) between diameter or compliance ( $\Delta D/\Delta P$ ) versus pressure for all treatment groups at all pressures (Fig. 1). T-tests were performed between UNT and all treatment groups as well as ELA and all treatment groups as a post-hoc comparison. Statistical analysis was limited due to software availability. After treatment, ATAs were tested at lower stretch ratios to avoid tearing the ATA. The results show that EGCG ATAs are significantly different at low pressures compared to UNT for diameter versus pressure; this can be attributed to the difference in stretch ratios before and after treatment. The ELA treated ATAs have a significant increase in diameter at lower pressures and lower compliance at higher pressures compared to UNT. The preventative (EGCG+ELA) treatment successfully maintained diameter and compliance in the physiological pressure range (90 – 120 mmHg) compared to UNT. The restorative (ELA+EGCG) treatment results are not significantly different from the ELA group for diameter or compliance versus pressure. Comparing the EGCG+ELA and ELA+EGCG, the EGCG+ELA curves are closer to UNT while the ELA+EGCG curves are closer to ELA.

Additionally, circumferential stress and stretch were calculated from the mechanical test data and unloaded dimensions (Fig.2). As the stretch and stress for each ATA depend on the unloaded dimensions, the stretch-stress curves are not quantitatively compared. Each ATA served as its own UNT so there were no ring measurements to calculate UNT stress and stretch. Qualitatively, the EGCG+ELA ATA is closer to EGCG, which resembles previous UNT ATA data, while the ELA+EGCG ATA is closer to ELA.

EGCG treatment of the ATA before chemically degrading elastic fibers was successful in preventing some mechanical changes. This suggests that EGCG may be an effective pharmaceutical treatment option for TAA. Ongoing research includes constitutive modeling to further characterize the mechanical changes and histological staining of polyphenols to visualize where the EGCG is in the ATA wall. Future work includes the *in vivo* delivery of EGCG to treat fragmented elastic fibers in genetic models of TAA.

## **Tables/Figures:**

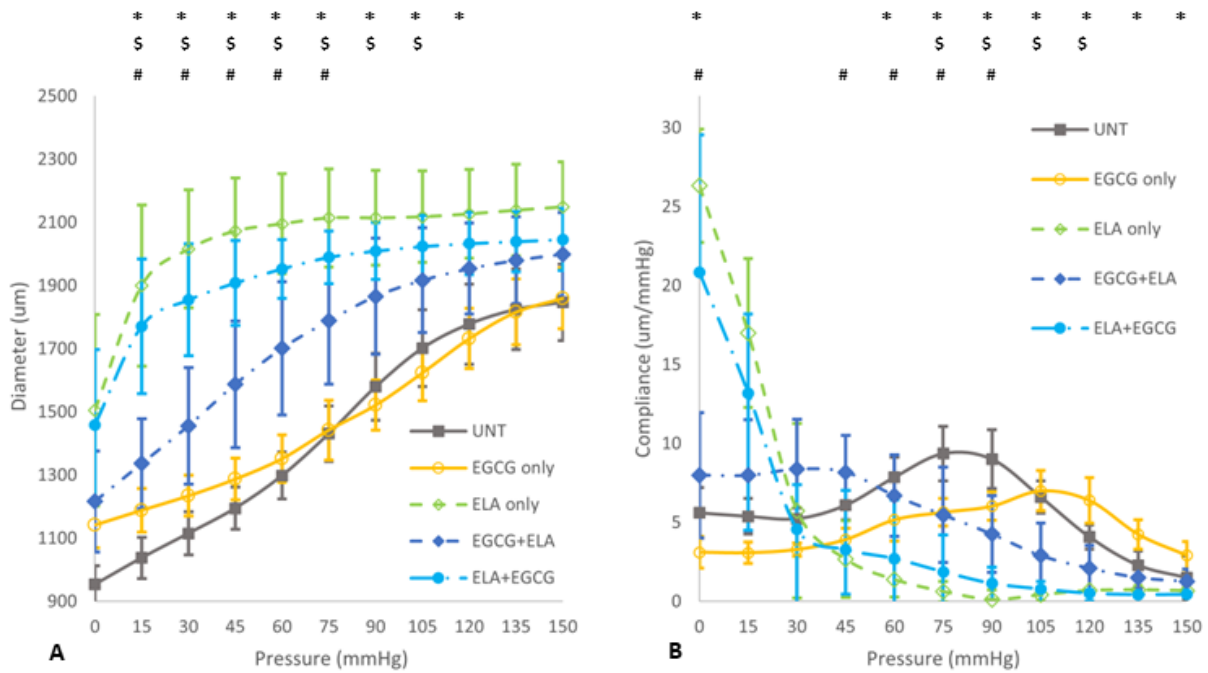


**Figure 1.** Average data from the cyclic pressurization protocol at the lowest constant axial stretch. Diameter-pressure (A), and compliance-pressure (B) for experimental groups. Comparisons are made to the UNT and ELA group using one-way ANOVA and t-tests. P-values <0.05 are noted by \*,\$,# for UNT vs ELA, UNT vs EGCG+ELA, and ELA vs EGCG+ELA, respectively. N=17 for UNT, N=3-5/group for all others.

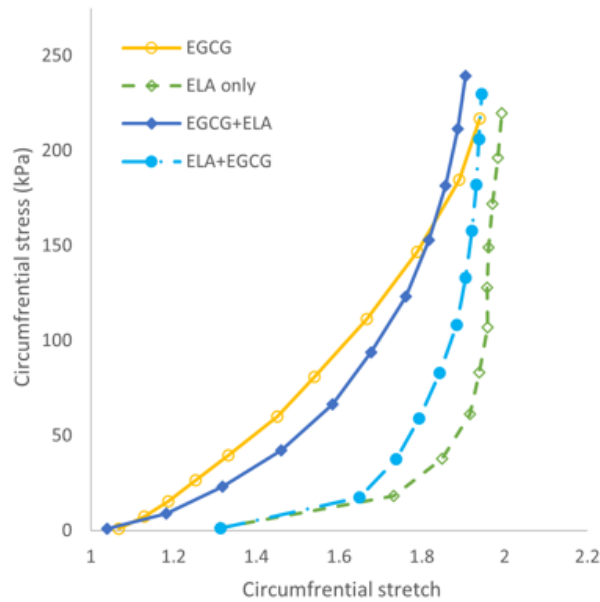


**Figure 2.** Material behavior of the cyclic pressurization protocol at the lowest constant axial stretch. Circumferential stress-circumferential stretch is shown for experimental groups. Error bars are not shown for clarity as stress and stretch values vary for each ATA at each pressure. N=3-5/group

## **Acknowledgements (Optional)**

## **References (Optional)**

1. Aronow WS. Treatment of thoracic aortic aneurysm. *Ann Transl Med.* 2018 Feb;6(3):66. doi: 10.21037/atm.2018.01.07. PMID: 29610755; PMCID: PMC5879515.
2. Crandall, C. L., Caballero, B., Viso, M. E., Vyavahare, N. R., & Wagenseil, J. E. (2022). Pentagalloyl glucose (PGG) prevents and restores mechanical changes caused by elastic fiber fragmentation in the mouse ascending aorta. *Annals of Biomedical Engineering.* <https://doi.org/10.1007/s10439-022-03093-x>
3. Sapuła P, Bialik-Wąs K, Malarz K. Are Natural Compounds a Promising Alternative to Synthetic Cross-Linking Agents in the Preparation of Hydrogels? *Pharmaceutics.* 2023 Jan 11;15(1):253. doi: 10.3390/pharmaceutics15010253. PMID: 36678882; PMCID: PMC9866639.
4. Setozaki S, Minakata K, Masumoto H, Hirao S, Yamazaki K, Kuwahara K, Ikeda T, Sakata R. Prevention of abdominal aortic aneurysm progression by oral administration of green tea polyphenol in a rat model. *J Vasc Surg.* 2017 Jun;65(6):1803-1812.e2. doi: 10.1016/j.jvs.2016.06.003. Epub 2016 Jul 26. PMID: 27473778.

## Introduction

Thoracic aortic aneurysm (TAA) is a condition characterized by aortic dilation affecting 5.3 per 100,000 people per year. Despite its prevalence, there are limited drug therapy treatments that prevent or restore the mechanical changes associated with the condition.<sup>2</sup> A common histopathological finding in TAAs is elastic fiber fragmentation (Fig. 1). Elastic fibers are essential to the aorta as they provide the elastic properties that allow the aorta to respond to large pressure and volume changes.<sup>1</sup> Epigallocatechin gallate (EGCG) is a polyphenol that has been found to increase elastin fiber deposition, making it potentially useful in treating TAA.<sup>3</sup> The mechanical effects of EGCG on the aortic wall are unknown. We hypothesize that EGCG, in a chemical TAA model, can restore or prevent mechanical changes caused by elastic fiber fragmentation

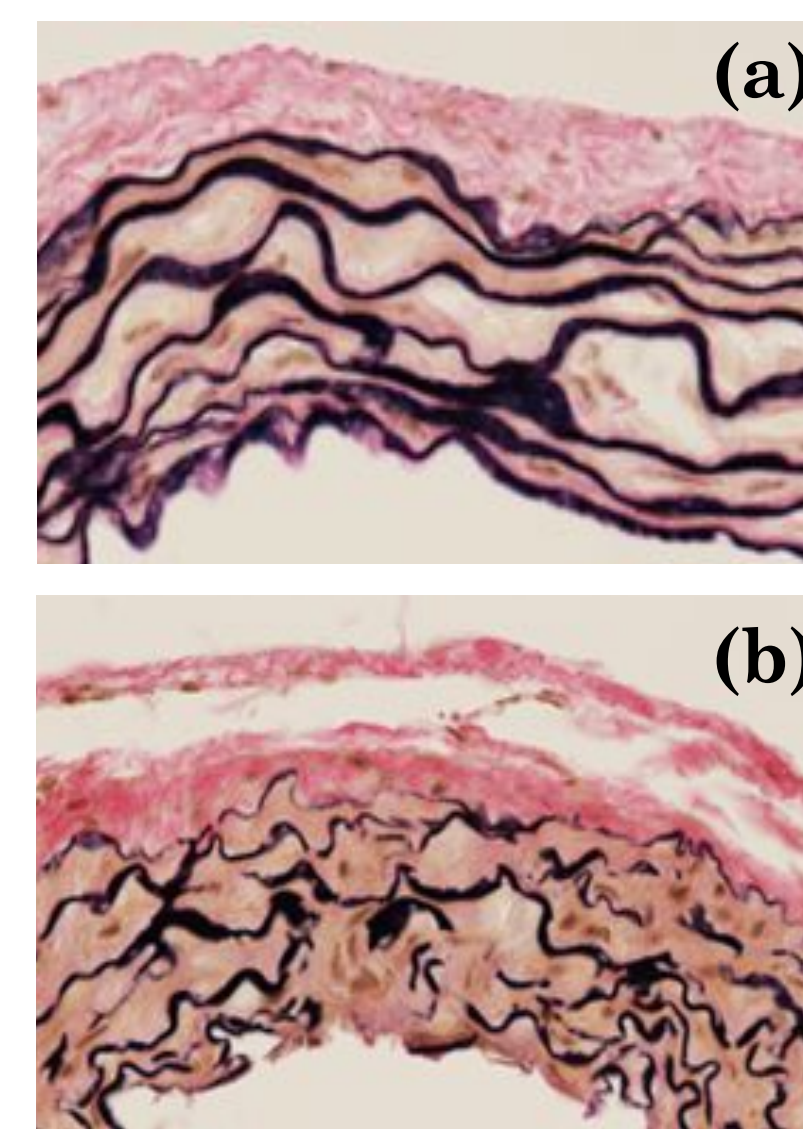


**Fig 1: VVG-stained cross sections of ATA that show elastin fiber structure of wild-type (a) and genetic aneurysm model (b).**

## Materials and Methods

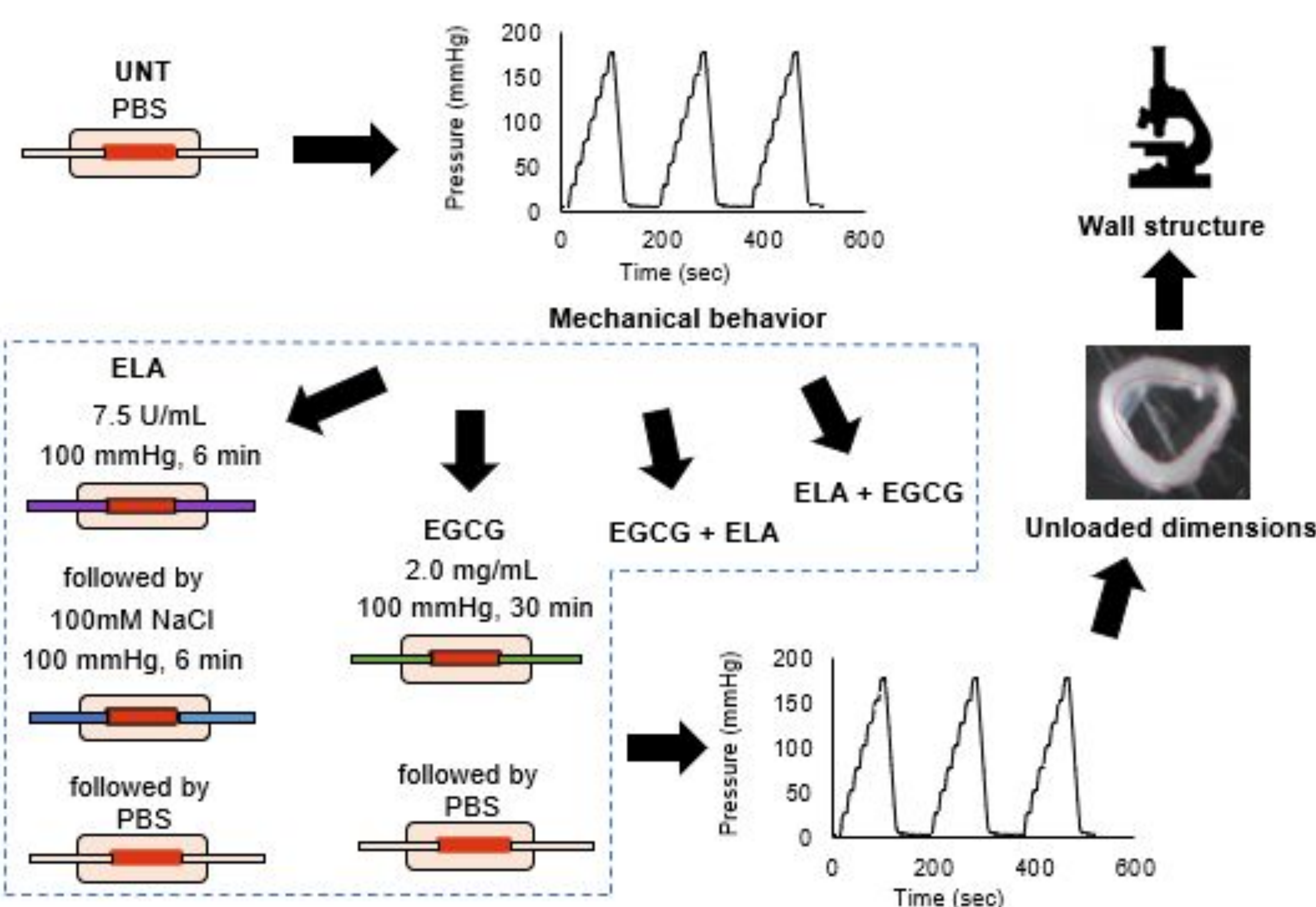


**Fig 2: Ascending thoracic aortas (ATAs) were dissected and cannulated onto a pressure myograph. Each ATA served as its own untreated control (UNT) and was mechanically tested before treatment to collect pressure, diameter, axial and circumferential force data. Then the ATA was treated with one of four protocols: ELA, EGCG, EGCG+ELA, or ELA+EGCG. Intraluminal pressure during treatment was maintained using a static pressure column. After treatment, ATAs were mechanically tested again, and horizontal cross-sections were cut to measure unloaded dimensions. Then, the cross-sections were fixed, sectioned, and imaged using a multi-photon microscope (excitation: 880 nm) to image elastin and collagen by autofluorescence (emission: 495-540 nm) and second harmonic generation imaging (emission: 420-460 nm).**

## Results

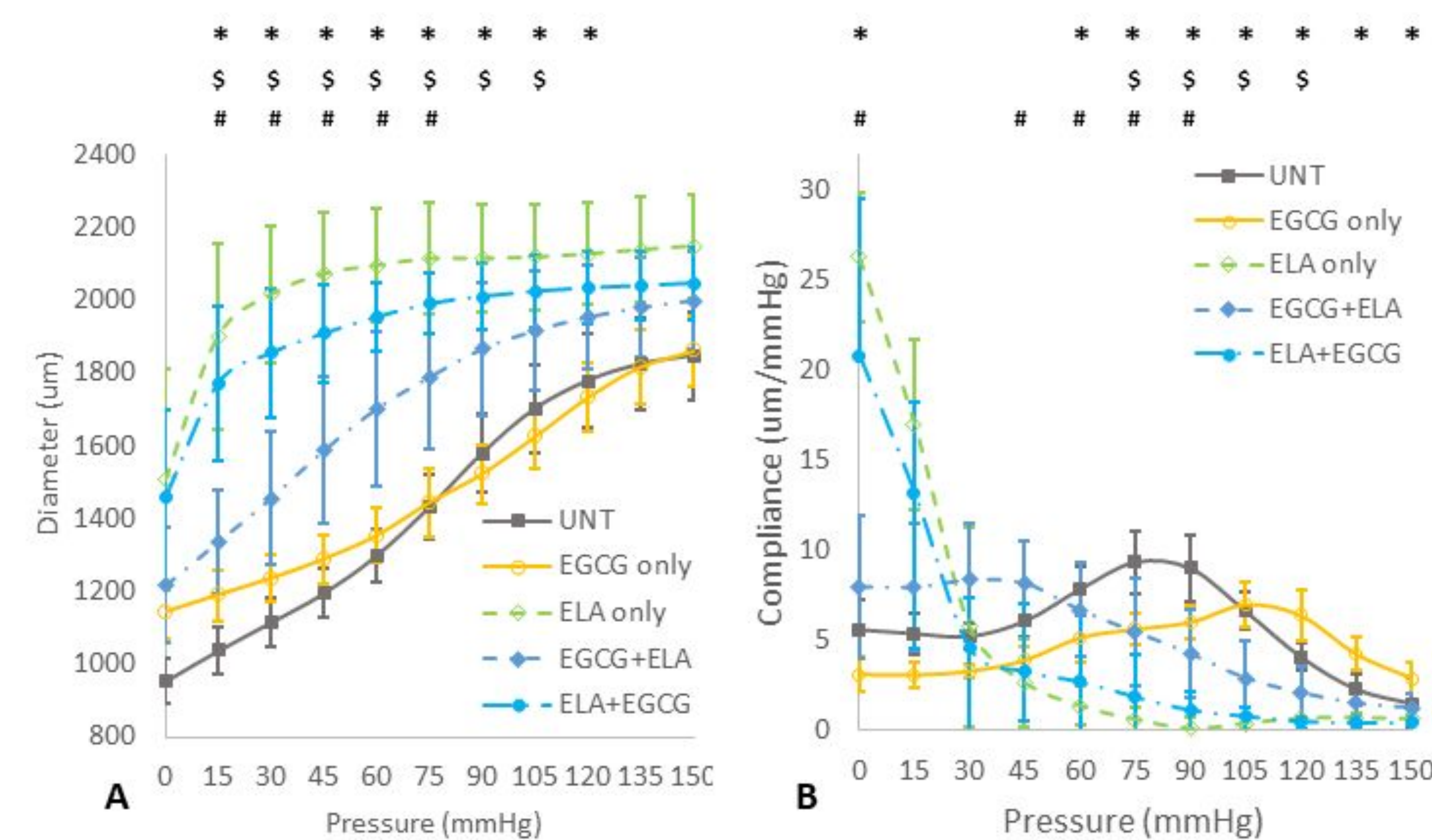


**Fig 3: Average data from the cyclic pressurization protocol at the lowest constant axial stretch. Diameter-pressure (A) and compliance-pressure ( $\Delta D/\Delta P$ ) (B) for experimental groups. Comparisons are made to the UNT and ELA group using one-way ANOVA and t-tests. P-values <0.05 are noted by \*,\$,#, for UNT vs ELA, UNT vs EGCG+ELA and ELA vs EGCG+ELA, respectively. N=17 for UNT, N=3-5/group for all others.**

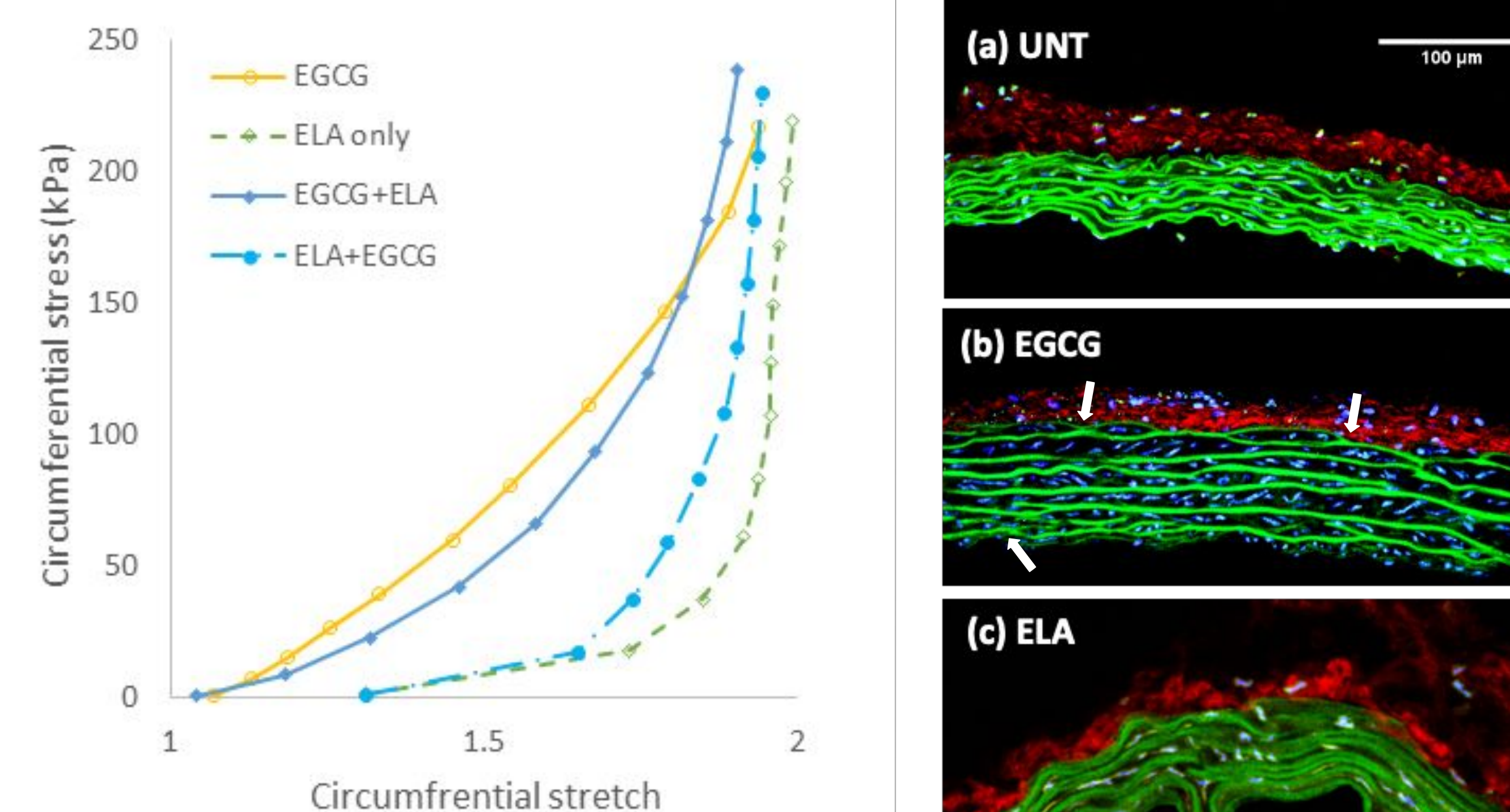


**Fig 4: Material behavior of the cyclic pressurization protocol at the lowest constant axial stretch. Circumferential stress vs circumferential stretch is shown for experimental groups. Error bars are not shown for clarity as stress and stretch values vary for each ATA at each pressure. UNT is not shown as unloaded dimensions could not be collected. N=3-5/group.**

**Fig 5: Multiphoton images of ATA cross-sections: UNT (a), EGCG (b), ELA (c), EGCG + ELA (d), and ELA + EGCG (e). Elastin is shown in green, collagen in red, and cell nuclei in blue. Scale bar = 100 µm. There seems to be an increase in laminae adhesions after EGCG treatment (arrows) while there is buckling in the elastic fiber layers after ELA treatment (\*).**

## Conclusions & Impact

### Intraluminal treatment of EGCG before ELA prevents mechanical changes associated with elastin fiber degradation.

- The results show ELA treated groups had significant increase in diameter at lower pressures and lower circumferential compliance at higher pressures compared to UNT.
- The preventative (EGCG+ELA) treatment successfully maintained diameter compliance in the physiological pressure range (90-120 mmHg).
- The restorative (ELA+EGCG) treatment results are not significantly different from the ELA group in diameter response to pressure and compliance.
- Stress-stretch analysis shows similar results that preventative (EGCG+ELA) is closer to EGCG (which resembles UNT) while restorative (ELA+EGCG) is closer to ELA.
- Multiphoton imaging shows visual degradation of elastin laminae in ELA, EGCG+ELA, and ELA+EGCG groups, as well as adhesion of elastin laminae in the EGCG group. Further imaging to confirm consistency of initial results is required.
- Comparing the mechanical behavior and imaging results of EGCG+ELA and ELA+EGCG treatments, the EGCG+ELA results are closer to UNT while the ELA+EGCG results are closer to ELA.

**These results show that preventative treatment of the ATA with EGCG was successful in preventing some mechanical changes. This suggests that EGCG may be an effective pharmaceutical treatment option for TAA.**

## Future Work

Ongoing research includes constitutive modeling to further characterize the biaxial mechanical changes and histological staining of polyphenols to visualize EGCG in the vessel wall. Next steps are to assess the efficacy of EGCG in vivo by delivering of EGCG to treat fragmented elastic fibers in genetic models of TAA. Additionally, further research on the mechanism of EGCG can help researchers develop drug therapy treatments for TAAs.

## References

1. Crandall, C. L., Caballero, B., Viso, M. E., Vyavahare, N. R., & Wagenseil, J. E. (2022). Pentagalloyl glucose (PGG) prevents and restores mechanical changes caused by elastic fiber fragmentation in the mouse ascending aorta. *Annals of Biomedical Engineering*. <https://doi.org/10.1007/s10439-022-03093-x>
2. Aronow WS. Treatment of thoracic aortic aneurysm. *Ann Transl Med*. 2018 Feb;6(3):66. doi: 10.21037/atm.2018.01.07. PMID: 29610755; PMCID: PMC5879515.
3. Sinha, A., Nosoudi, N., & Vyavahare, N. (2014). Elasto-regenerative properties of polyphenols. *Biochemical and Biophysical Research Communications*, 444(2), 205-211. <https://doi.org/10.1016/j.bbrc.2014.01.027>

### Acknowledgements:

Special thanks to all the members of the Wagenseil Vascular Mechanics Laboratory for all their guidance and assistance with this project.

Funding provided by the National Science Foundation NSF award number CMMI-1548571



### **3D Printed System for Simultaneous Stretch and Imaging of Engineered Microtissues**

Maya Evohr<sup>1,2</sup>, Riya Bhakta<sup>2</sup>, Ghiska Rhamadita<sup>2</sup>, Ari Rapalino<sup>2</sup>, Nathaniel Huebsch<sup>2</sup>

<sup>1</sup>Worcester Polytechnic Institute, <sup>2</sup>Washington University in St. Louis

#### **Introduction**

Cardiac hypertrophy is a condition which can lead to arrhythmias and heart failure. While genetics and chemical stress are partly responsible, mechanical stress also contributes to this pathological condition (1). In order to investigate how mechanics interacts with genetics, we require systems to apply mechanical stresses, like stretch, to genetically defined engineered heart tissues. To capture the impact of stretch on cardiac physiology using optocardiography, this system must be small enough to easily fit under a microscope and must be easily replicated. This allows researchers to determine the consequences of mechanical load by studying how cells remodel their physiology and structure during tissue formation as well as comparing them to non-stretched tissues after tissue formation is complete. This knowledge can help researchers to develop better models of cardiac hypertrophy, leading to better approaches to manage related genetic diseases including hypertrophic and arrhythmogenic cardiomyopathy.

#### **Materials and Methods**

The stretch device and stretch chamber were created using Fusion360 computer aided design software (Figure 1). The stretch device was prototyped with polylactic acid using a fused deposition modeling technique. Hardware (bearing, screw, insert) was added to enable the device to stretch 0.2mm per revolution of the screw (Figure 2).

The stretch chambers consisted of four mounting holes around the edges and a recessed area containing four microdevices (circular wells with four upright posts each). The stretch chambers were fabricated using Hydrogel Assisted Stereolithographic Elastomer prototyping (HASTE) using agar to cast the chamber out of Sylgard 184 polydimethylsiloxane (PDMS) with a base-to-crosslinker ratio of 18:1 (2).

To begin to test the effects of stress on tissue and cell morphology, NIH 3T3 fibroblasts were seeded into collagen gel (Figure 3). The final cell concentration is  $2 \times 10^7$  cells/mL and the final collagen (rat tail derived Collagen I, Gibco) concentration is 1.5mg/mL; each device holds 7 $\mu$ L of gel/cell suspension. Trials were done to optimize the volumetric ratio of media to cell-laden gels to ensure cell viability and tissue formation. NucSpot Live 488 was used with a Keyence BZ 9000 E microscope to visualize the cell nuclei as the tissue developed.

#### **Results, Conclusions, and Discussions**

A stretch system composed of a PLA stretch device and PDMS stretch chamber was successfully created. Fusion 360 modeling showed that forces exerted on the stretch chamber by the device were applied evenly and there was an equal stress distribution during the stretch process (Figure 1). The total system cost is under \$30 and the system allows for live imaging of microtissues during the stretch. The system can be stretched to  $77 \pm 20\%$  strain before failure, well above the range of typical commercial strain devices. A successful prototype for the stretch system was developed and has the potential to enhance research on the linkage between mechanical stretch and genotype-phenotype differences in genetic conditions causing cardiac hypertrophy and fibrosis.

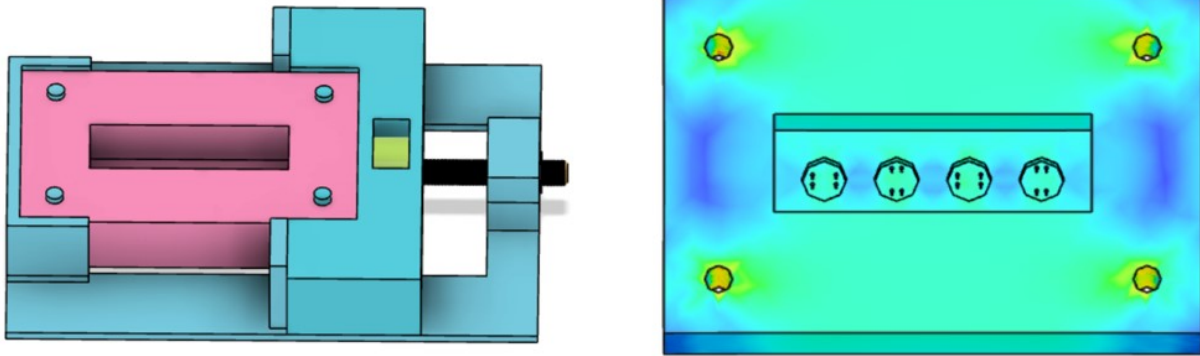


**Figure 1** Left: CAD renderings of stretch system with stretch chamber (pink), bearing (green), stretch device (blue), and screw (black). Right: Distribution of stress exerted on stretch chamber during stretch. Note, stress within each microwell area is equivalent.

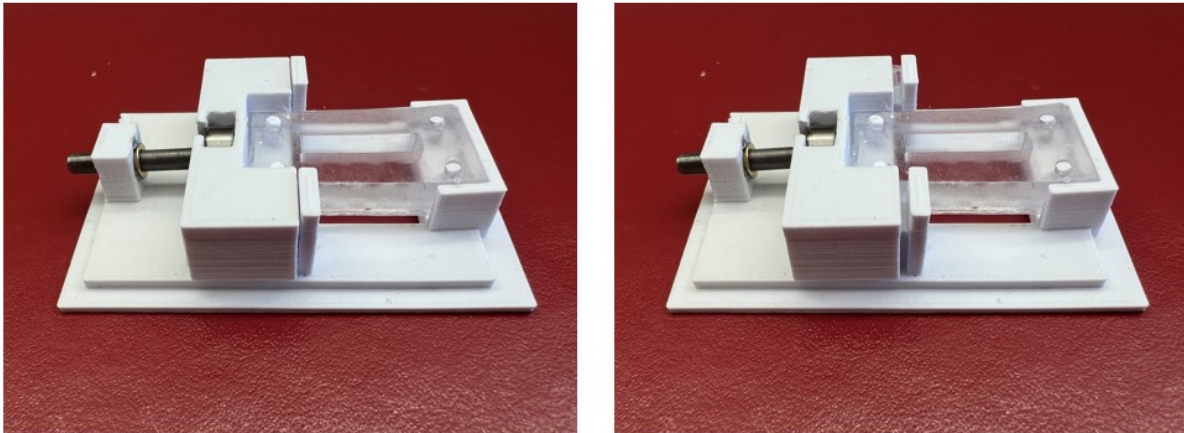


**Figure 2** Stretch Device with PDMS Stretch Chamber. Chamber is unstretched (left) and stretched by turning the screw (right). Stretch system dimensions are 61.5 mm x 45.25 mm x 10mm.

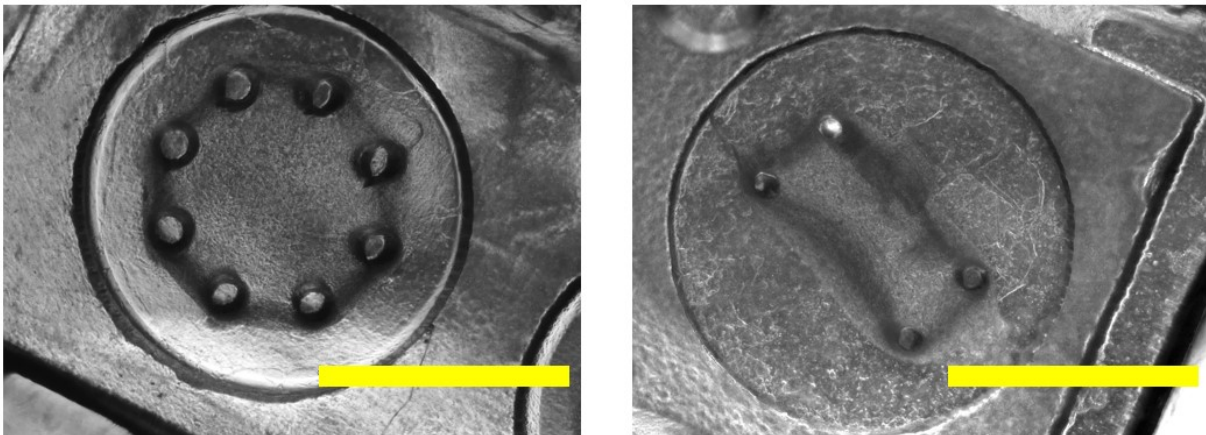


**Figure 3** NIH 3T3 Fibroblast microtissues cultured in device well. Eight post design shown on left and four post design shown on right. Scale bars: 2mm.

### Acknowledgements

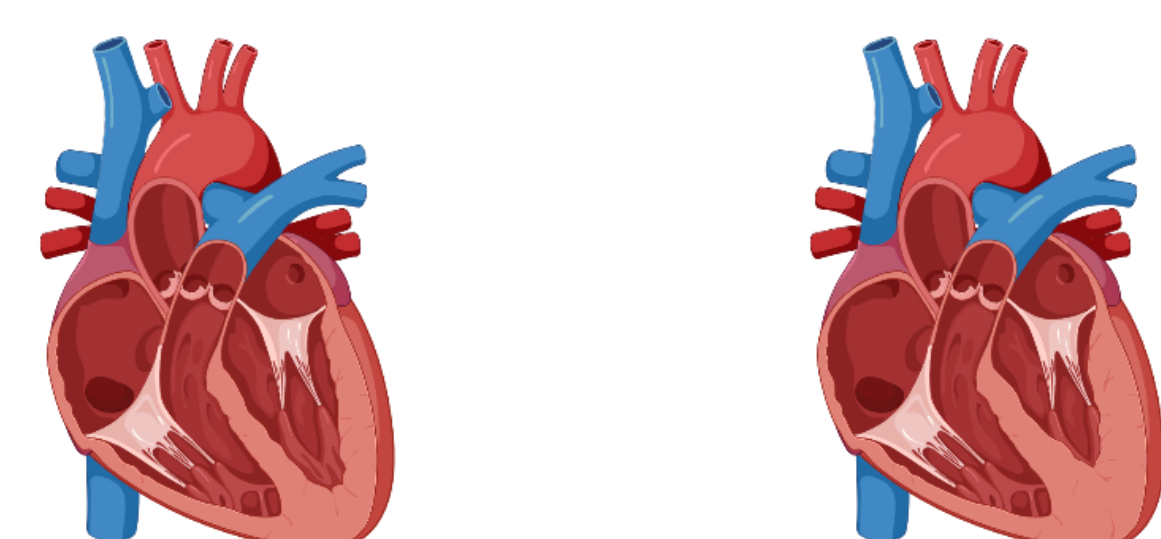
This work was supported by the NSF Center for Engineering Mechanobiology (CMMI:15-48571)

## References

1. Ruwhof, C., & van der Laarse, A. (2000). Mechanical stress-induced cardiac hypertrophy: mechanisms and signal transduction pathways. *Cardiovascular research*, 47(1), 23–37.  
[https://doi.org/10.1016/s0008-6363\(00\)00076-6](https://doi.org/10.1016/s0008-6363(00)00076-6)
2. Simmons, D. W., Schuftan, D. R., Ghiska Ramahdita, & Huebsch, N. (2023). Hydrogel-Assisted Double Molding Enables Rapid Replication of Stereolithographic 3D Prints for Engineered Tissue Design. *ACS Applied Materials & Interfaces*, 15(21).  
<https://doi.org/10.1021/acsami.3c02279>

## OBJECTIVE

Cardiac hypertrophy is a condition which can lead to arrhythmias and heart failure. While genetics and chemical stress are partly responsible, mechanical stress also contributes to this pathological condition (1).



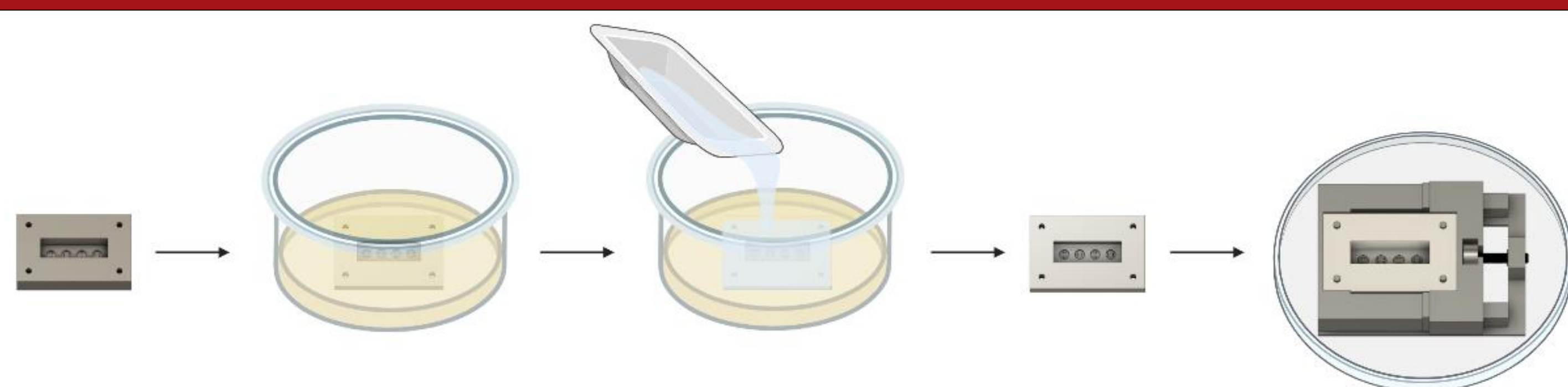
Unaffected heart (left) and hypertrophic heart (right)

A system is needed to allow researchers to determine the consequences of mechanical stretch as well as comparing them to non-stretched tissues after tissue formation is complete.

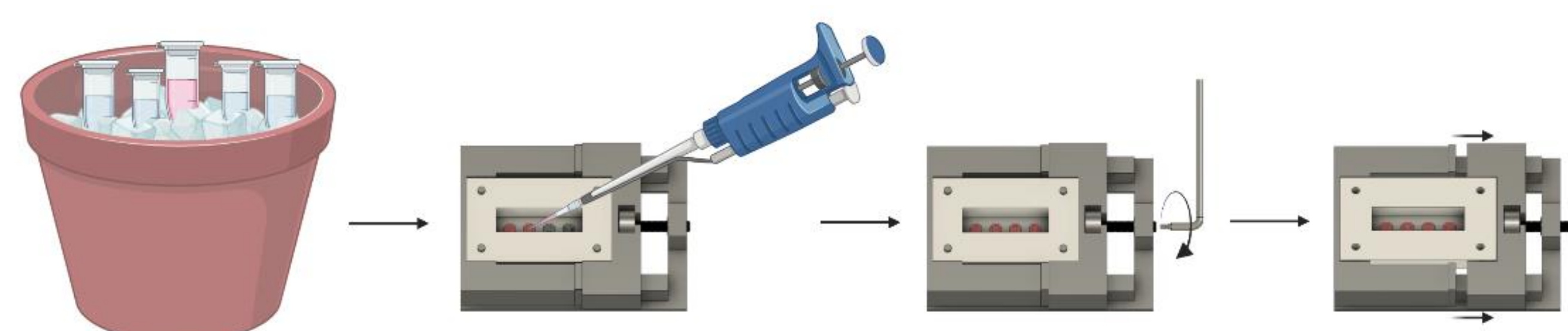
This knowledge can help researchers to develop better models of cardiac hypertrophy, leading to better approaches to manage related genetic diseases including hypertrophic and arrhythmogenic cardiomyopathy.

**We created a small, easily replicable system to apply uniaxial stretch to genetically defined engineered heart tissues in order to study how cells remodel their physiology and structure during tissue formation.**

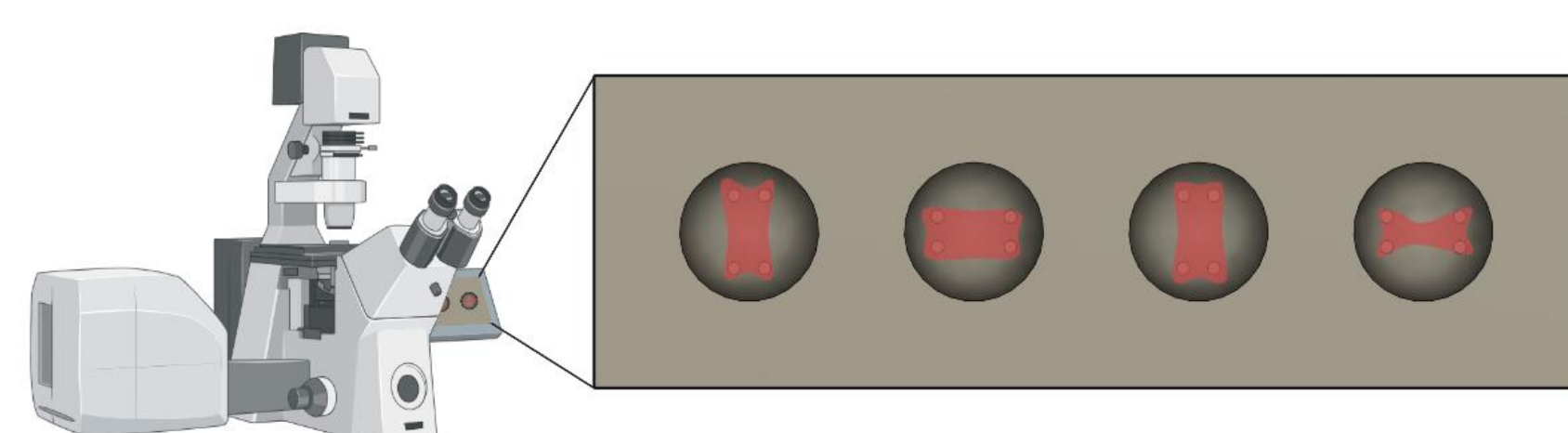
## METHODS



Stretch chamber was SLA printed on a Form3 3D printer. A negative was made using 2.5% agar with 0.4% TritonX. From this, a positive was made from Sylgard 184 PDMS in an 18:1 base to crosslinker ratio. The stretch chamber was then placed onto the stretch device, which was 3D printed with PETG using a Prusa MK3i3 printer. [2]



NIH3T3 Fibroblasts were seeded with a cell concentration of  $2 \times 10^7$  cells/mL into a collagen gel containing dPBS, 10x DMEM, HEPES, Collagen I derived from rat tail, and NaOH. 7  $\mu$ L of cell-seeded gel was placed into each well of the device. A percentage of cells were labeled with R18 or Vybrant DiO stain in order to visualize cellular positioning.



Samples formed tissues after 24 hours and were imaged using a Nikon Eclipse Ts2R equipped with a digital CMOS camera and Aura II Epifluorescence source with single LED light sources. When not being imaged or stretched, samples were immersed in DMEM with 10% FBS and incubated at 37°C.

## RESULTS & DISCUSSION

**A uniaxial stretch system capable of precise stretch (0.1mm increments) was developed. The system costs less than \$30 USD, fits in a standard 70mm Petri dish, and allows for live imaging of tissues during stretch.**

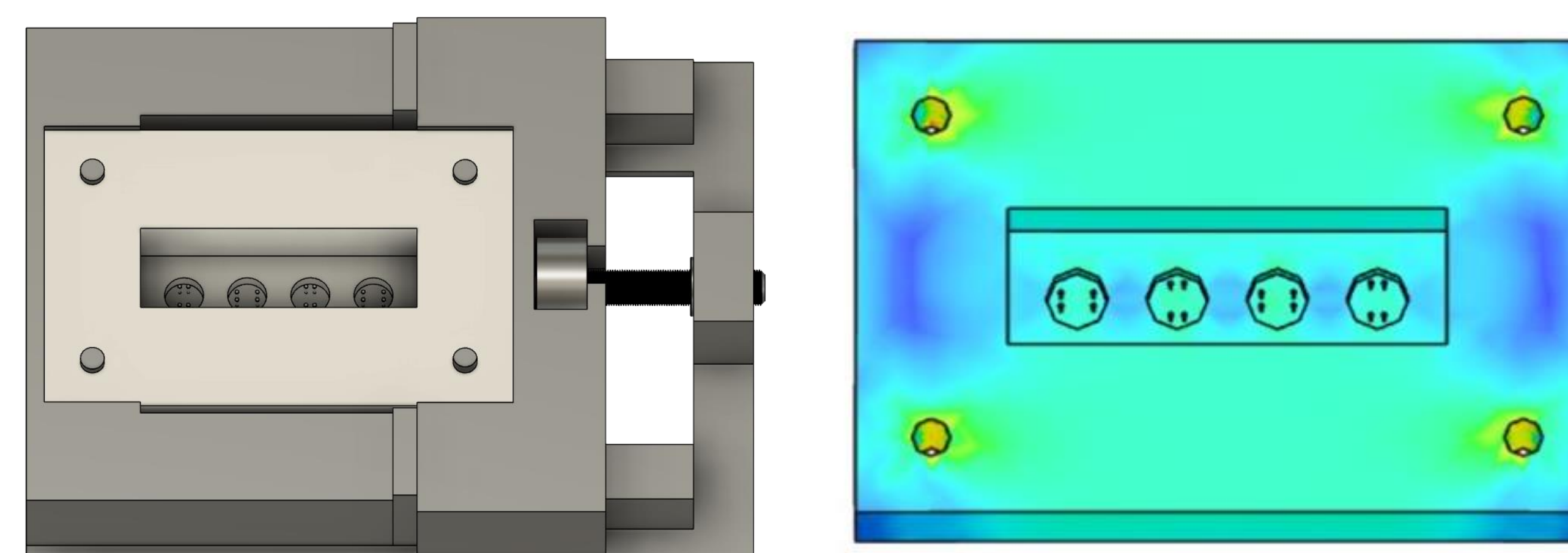


**Figure 1** Left: CAD rendering of stretch system with stretch chamber (tan), stretch device (grey), bearing (silver), and attached screw (black). Right: Distribution of stress exerted on stretch chamber during stress. Note, stress within each microwell area is equivalent.

The final device dimensions are 60.5mm by 43.25 mm by 10mm (Figure 1). Fusion 360 modeling showed that forces exerted on the stretch chamber by the device were applied evenly and there was an equal stress distribution during the stretch process (Figure 1). The system allows for reuse, as each PDMS chamber is removable from the PETG stretch device (Figure 2).

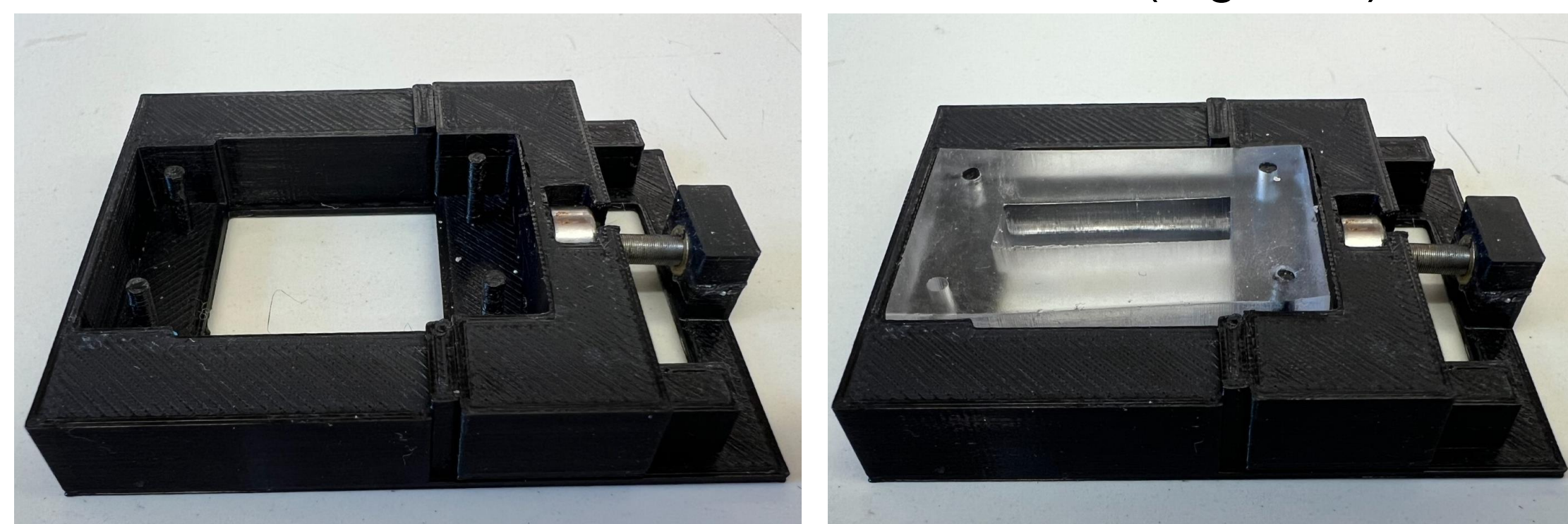


**Figure 2** Left: Stretch device without stretch chamber. Right: Completed stretch system.

### Fibroblast-based Tissue Formation and Stretch

Fibroblast-derived tissues were successfully formed, imaged, and stretched using this system (Figure 3). Stretch was applied once every 24 hours after imaging at a rate of 10%, 20%, or 30% per day.

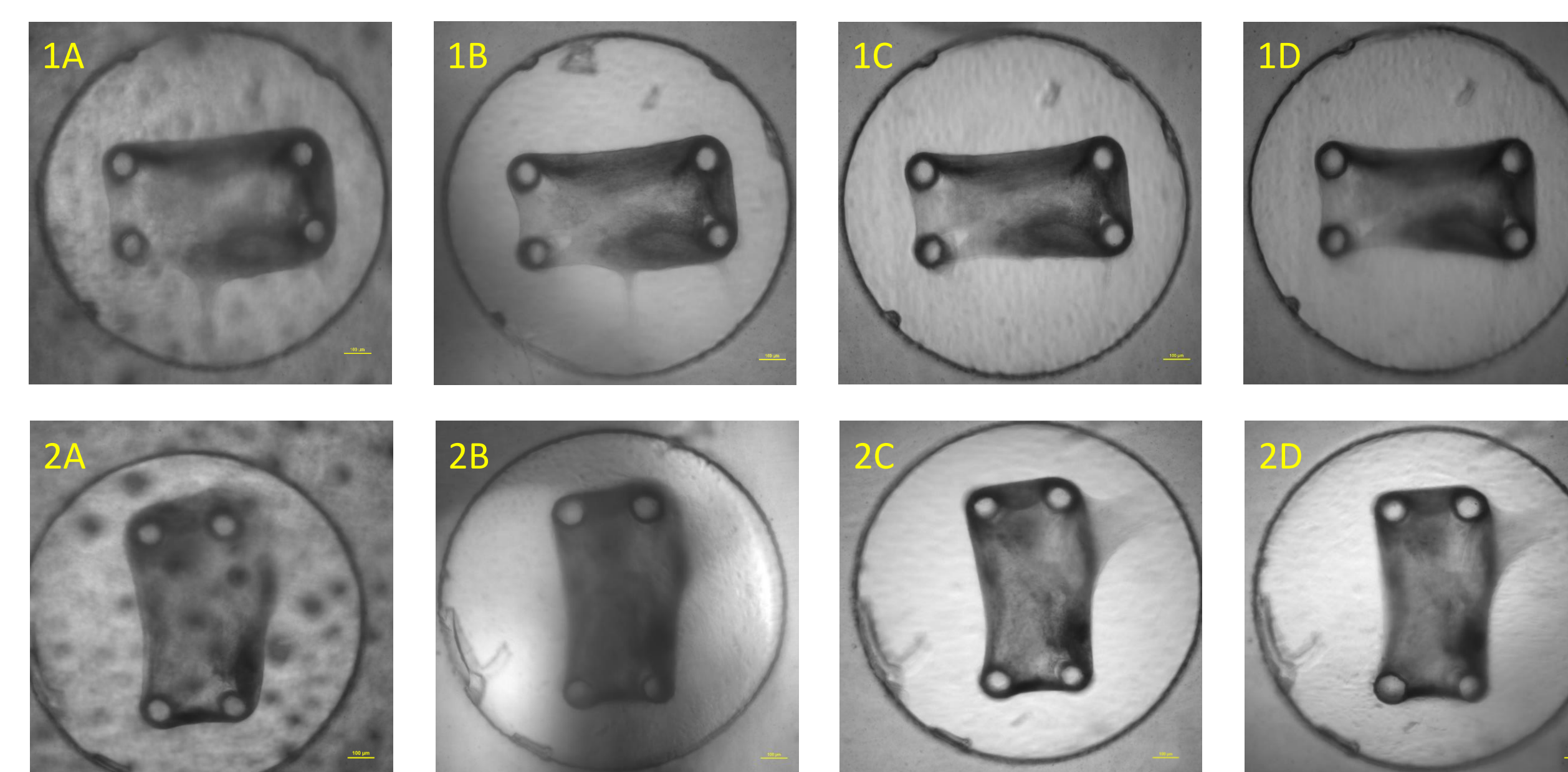


**Figure 3** Compaction of tissues around 4 post microdevice from day 2 to day 5 (A-D) with 10% vertical stretch applied per day. Tissues were oriented with the long axis perpendicular to the direction of stretch (top) or parallel to the direction of stretch (bottom). Diameter of circular well is 3.25 mm.

## RESULTS & DISCUSSION cont.

### Effects of Uniaxial Stretch on Fibroblast Tissues

As the fibroblast tissues were stretched, they appear to compact along the axis of stretch. In Figure 4 (below), tissues were stretched horizontally.

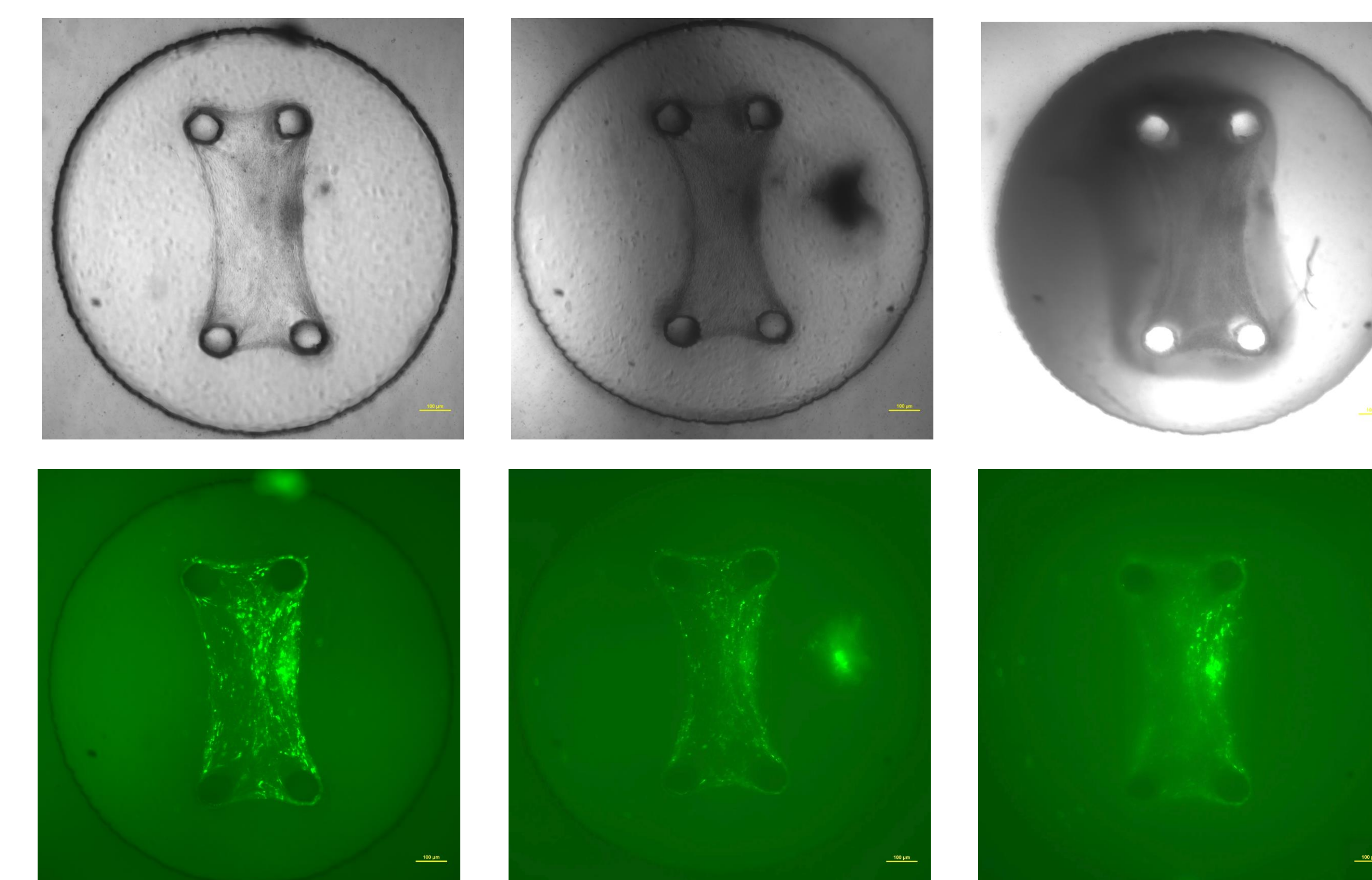


**Figure 4** Compaction of tissue around 4 post microdevice from day 2 to day 4 (left to right) with 30% horizontal stretch applied per day. 5% of cells were stained with Vybrant DiO. GFP fluorescence imaging shown on bottom. Diameter of circular well is 3.25 mm.

This system allows for study of stretched tissues both in brightfield and in fluorescence microscopy. This is crucial to understanding cellular alignment and response to stretch.

## CONCLUSION & FUTURE WORK

A successful prototype for the stretch system was developed and has the potential to enhance research on the linkage between mechanical stretch and genotype-phenotype differences in genetic conditions causing cardiac hypertrophy and fibrosis. Future work may include refining this design for quick and efficient production and eliminating the need for soldering the screw to the bearing. Additionally, studies using this system with cardiomyocytes or iPSC-derived heart cells will be completed.

## REFERENCES

- [1] Ruwhof, C., & van der Laarse, A. (2000). Mechanical stress-induced cardiac hypertrophy. *Cardiovascular research*, 47(1), 23–37.
- [2] Simmons, D. W., Schuftan, D. R., Ramahdita, G. & Huebsch, N. (2023). Hydrogel-Assisted Double Molding Enables Rapid Replication of Stereolithographic 3D Prints for Engineered Tissue Design. *ACS Applied Materials & Interfaces*, 15(21).

## ACKNOWLEDGEMENTS

This work was supported by the NSF Center for Engineering MechanoBiology CMMI-1548571. Thank you to all the members of the Huebsch Lab for your guidance and mentorship. Thank you to Biorender for use of their graphics software.



# **Novel 3D Ex-Vivo Model for Delivering Radial Compressive Stress**

Calvin Paulsen<sup>2,3</sup>, Ye Lim Lee<sup>1</sup>, Akash Shaji<sup>2</sup>, Miranda Gamino-Ornelas<sup>1</sup>, Amit Pathak<sup>1,2</sup>

1. Washington University, Dept. of Biomedical Engineering, St. Louis, MO; 2. Washington University, Dept. of Mechanical Engineering & Materials Science, St. Louis, MO; 3. Clemson University, Dept. of Bioengineering, Clemson, SC

## **Introduction**

Breast cancer is a leading cause of cancer-related deaths worldwide. In 2020, it surpassed lung cancer as the most diagnosed cancer globally, with 2.3 million cases. The 5-year survival rate for women diagnosed with late-stage, distantly metastasized breast cancer is only 30%. Research into understanding why cancerous breast epithelial tissue becomes aggressive and invasive is critical to improving patient outcomes.

Abnormal cell migration can contribute to the spread of cancer cells and the development of metastases. There is growing evidence that physical cues play a significant role in tumor progression and metastasis. As a tumor progresses, two types of stresses develop in the tumor microenvironment (TMI): solid stresses from either abnormal growth or external stress, and stress from interstitial pressure. These stresses can cause blood and lymphatic vessels at the center of the tumor to collapse, creating a hypoxic and acidic TMI that can lead to more invasive phenotypes. However, the effect of these stresses on tumor phenotype is not well understood.

We are developing a novel ex-vivo method for testing compressive radial stresses on a three-dimensional cell suspension in a collagen matrix, which expands upon current two-dimensional models. By studying how normal and breast cancer cells respond to these stresses, we hope to gain insights into how physical cues contribute to tumor progression and

metastasis, potentially leading to new treatments that improve patient outcomes.

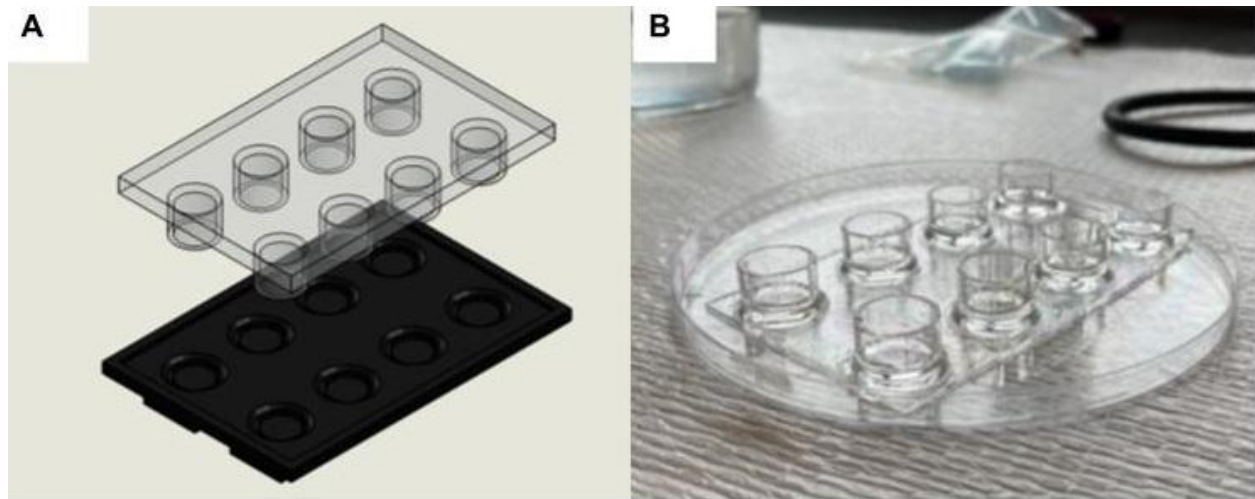


Figure 1: A) PDMS cell culture plate and mold SolidWorks rendering; B) PDMS cell culture plate removed from mold.

## Materials and Methods

Prototyping was achieved using SolidWorks® to create a negative mold ( Fig. 1) made of TPU-95A filament. The mold was printed on a LulzBot Taz Workhorse Edition Printer with a 0.2 mm layer height and 20% infill density. We sprayed MG Chemicals® Silicone Modified Conformal Coating Spray to ensure the PDMS was fully cured. SYLGARD™ 184 Silicone Elastomer (Dow Corning®) was mixed at a 10:1 wt. % ratio and placed in the desiccator for an hour. MCF10A breast epithelial cells with nuclear GFP spheroids were seeded at 1.5k cells with 20  $\mu$ l of volume in an ultra-low adhesion (ULA) 96-well plate (Eppendorf®) and allowed to form overnight. The PDMS was cured at 65°C for two and half hours and then bonded to the surface of a 12-well plate lid using an oxygen plasma treatment for five minutes. PDMS was cleaned using 1X PBS and 10 minutes of UV crosslinking, plasma cleaning for 5 minutes. 50  $\mu$ l of 2 mg/ml collagen was deposited and allowed to polymerize for 30 minutes at 37°C. Then, two spheroids were seeded into the gel with the remaining 50  $\mu$ l of collagen, allowing 45 minutes for polymerization (Fig. 2). 500  $\mu$ l of cell culture media was then added into the wells and 4-inch zip ties were secured around the wells and pulled until taut. Cells were imaged using a Zeiss

AxioObserver microscope (Carl Zeiss Microscopy, Germany).

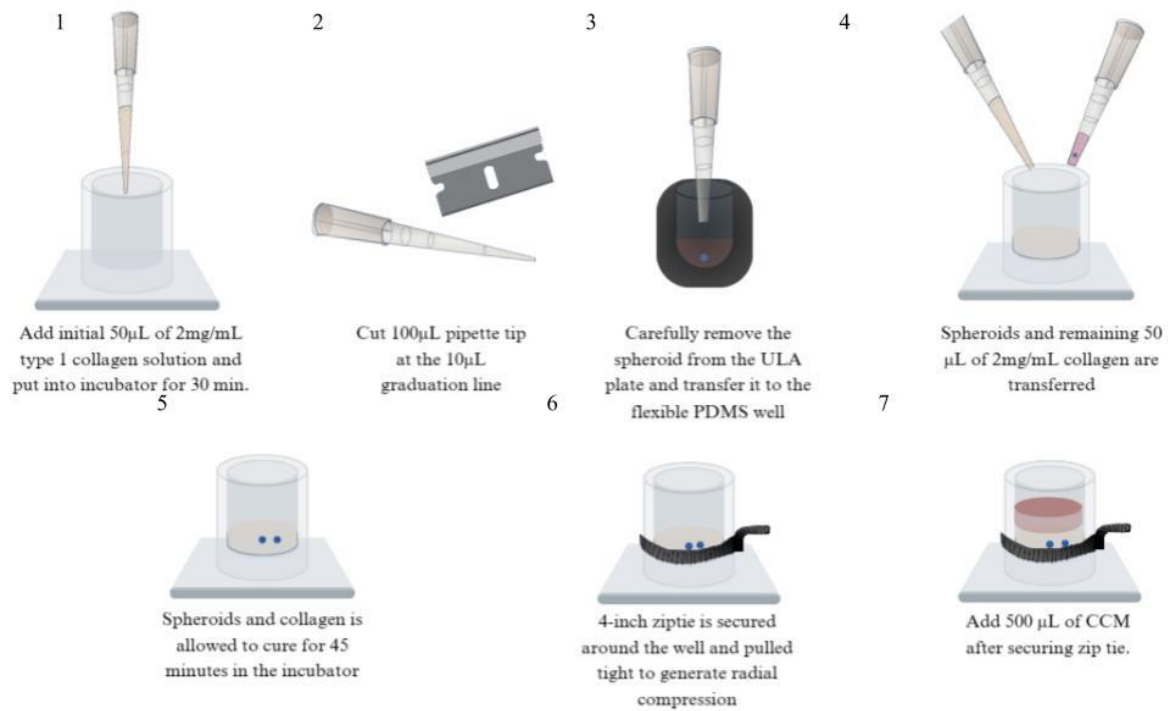


Figure 2: General procedure for preparing the flexible cell culture plate for imaging

## Results, Discussion, and Conclusions

3D printing has revolutionized prototyping, allowing for rapid and cost-effective methods for creating models from CAD files. Fused deposition modeling enabled testing of multiple models before refining the mold. Experiments were conducted to determine the best method for generating the cell culture well plates. We tested PETG, PLA, and TPU-95A 3D-printing filaments with three treatment groups: no treatment, oxygen plasma treatment, and silanization. A flexible TPU-95A filament with silanization worked best to release the PDMS well

plate (Table 1).

Material	Treatment**	Outcome
PLA*	None	Failed to Release from mold
PLA*	Oxygen Plasma	Failed to Release from mold
PETG	None	Failed to Release from mold
PETG	Plasma Treatment	Failed to Release from mold
PETG	Silianization	Failed to Release from mold
TPU-95A	None	Released, but PDMS curing issue
TPU-95A	Plasma Treatment	Released, but PDMS curing issue
TPU-95A	Silianization	Released with fully cured PDMS

\* PLA was eventually no longer tested as it had too low of a glass transition temperature and would begin to soften at the curing temperatures used.  
 \*\* All samples were cured at 65°C

Table 1: Results of Mold Release Study

We aimed to create spheroid clusters of MCF10A cells by testing different cell groups and volumes to determine optimal conditions for spheroid formation. We first tested 10K cells at 35  $\mu$ L, but they were fragmented. Thus, we decided to lower the amount of cells used in the plate, testing 1.5k and 1k cells per spheroid in 20, 25, and 35 microliters of media each (Fig. 3A). A Countess 3 Automated Cell Counter (Thermo Scientific®) was used to determine the live cell count and proper dilutions. After forming the spheroids, we carefully transferred them using a cut 100  $\mu$ l pipette tip (Fig. 3B). We found that seeding 1.5K cells at 20  $\mu$ l was optimal for forming spheroids using ULA plates and MCF10As.

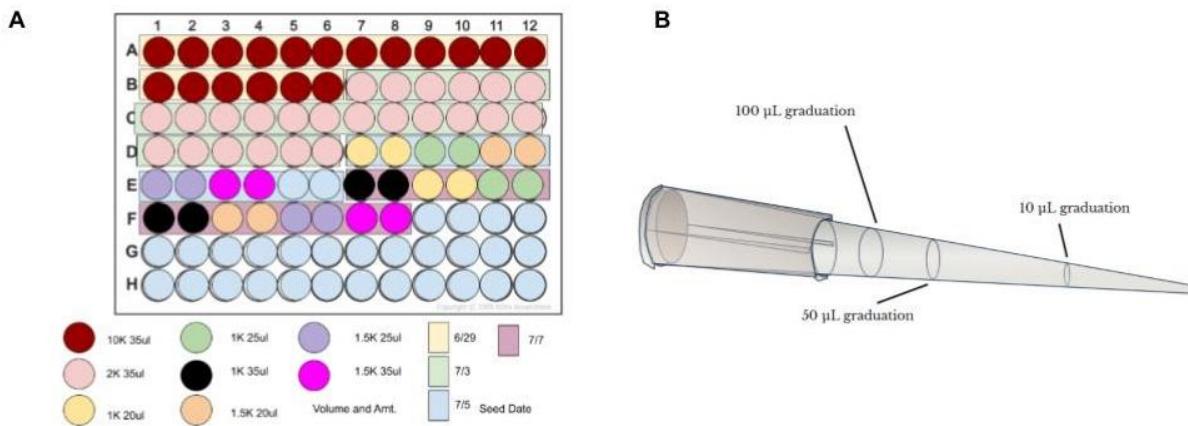


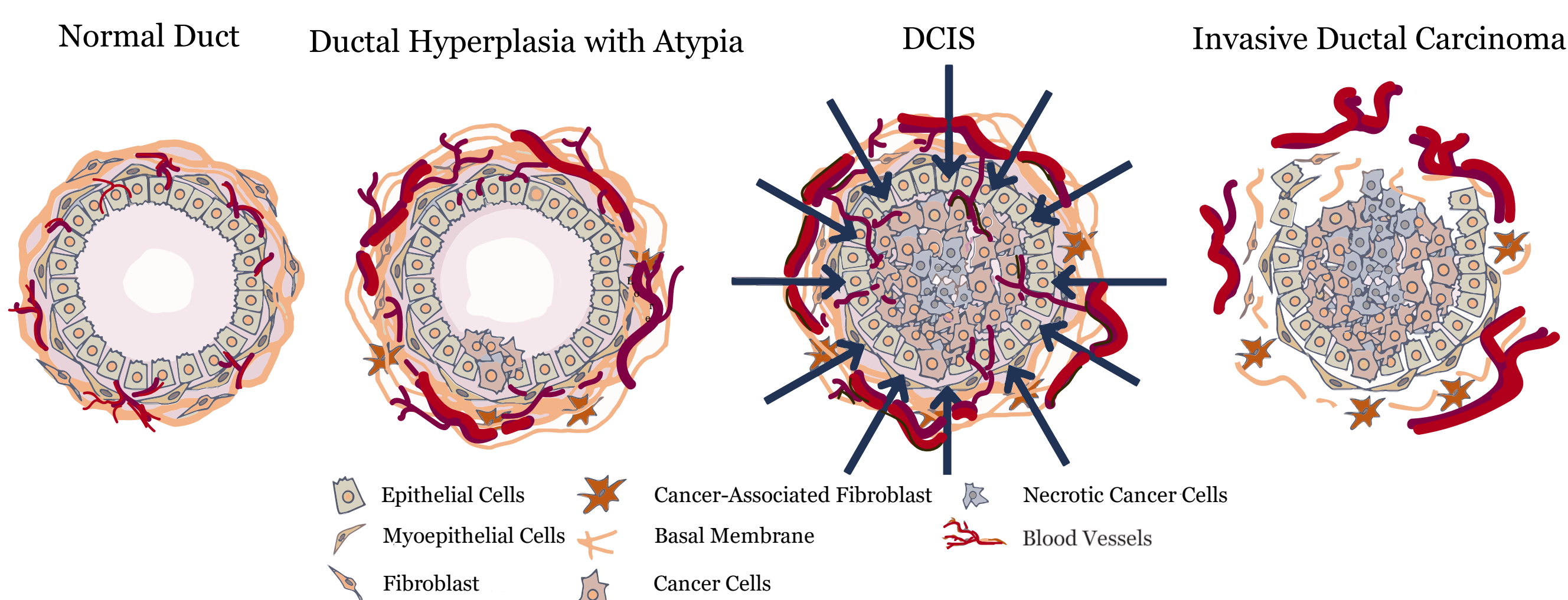
Figure 3: A) 96 well plate experimental set up. B) 100 $\mu$ L pipette tip

The eventual purpose of our model is to apply specific amounts of compression to normal and cancerous cell spheroids within a 3D collagen matrix, observing their behavior using time-lapse microscopy allowing us to study the effects of radial compression on tumor progression and metastasis in a three-dimensional environment. We are currently collecting data of compressed/uncompressed systems using zip ties to identify any morphological and/or migratory changes in the cells. Future iterations of the device will incorporate tunable radial compression through compressed air, along with improving the imageability of the PDMS wells.

With these experiments, we plan to examine ECM deposition; cross-linking; fiber alignment, length, and size; cellular changes to actin, myosin, and Rho-ROCK signaling; and traction forces in response to varying compression with fluorescent beads and PIV. These studies will provide valuable insights into explaining the mechanisms by which radial compression contributes to cell behavior.

## Introduction

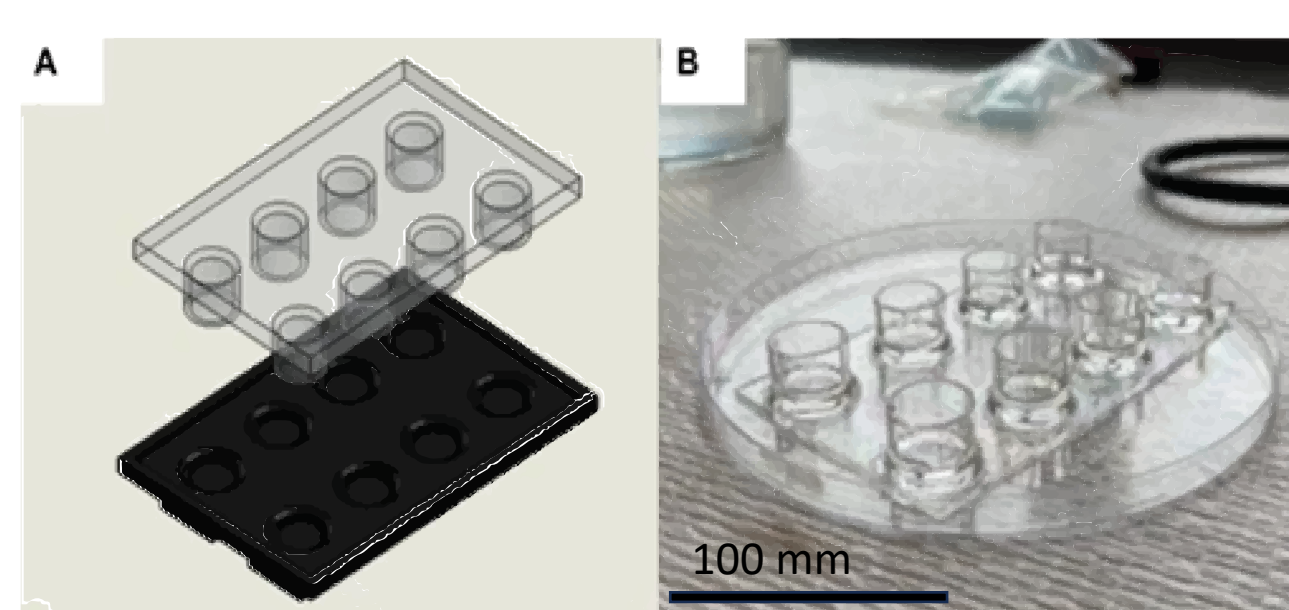
Lobular and ductal subtypes make up 40-75% of all breast cancers, and 80% of invasive breast cancers are a ductal subtype.<sup>1</sup> It is believed that ductal carcinoma follows a linear type progression. As the cancer progresses, it begins to develop solid stresses that result in radial compression to the center of the tumor. This can cause the collapse of delicate vessels at the interior of the tumor. This leads to a hypoxic and acidic environment at the interior of the tumor, as well as greatly increases the risk of more invasive phenotypes.



However, less understood is the cellular response to the resulting radial compression. We are developing a novel ex-vivo method for testing compressive radial stresses on a three-dimensional cell suspension in a collagen matrix, which expands upon current two-dimensional models. Utilizing the wide interactions of Cell-ECM binding, we can develop models to mimic in vivo mechanical conditions and treat cell behavior as an output. These outputs include observing spreading, migration, and cancer cell invasion.

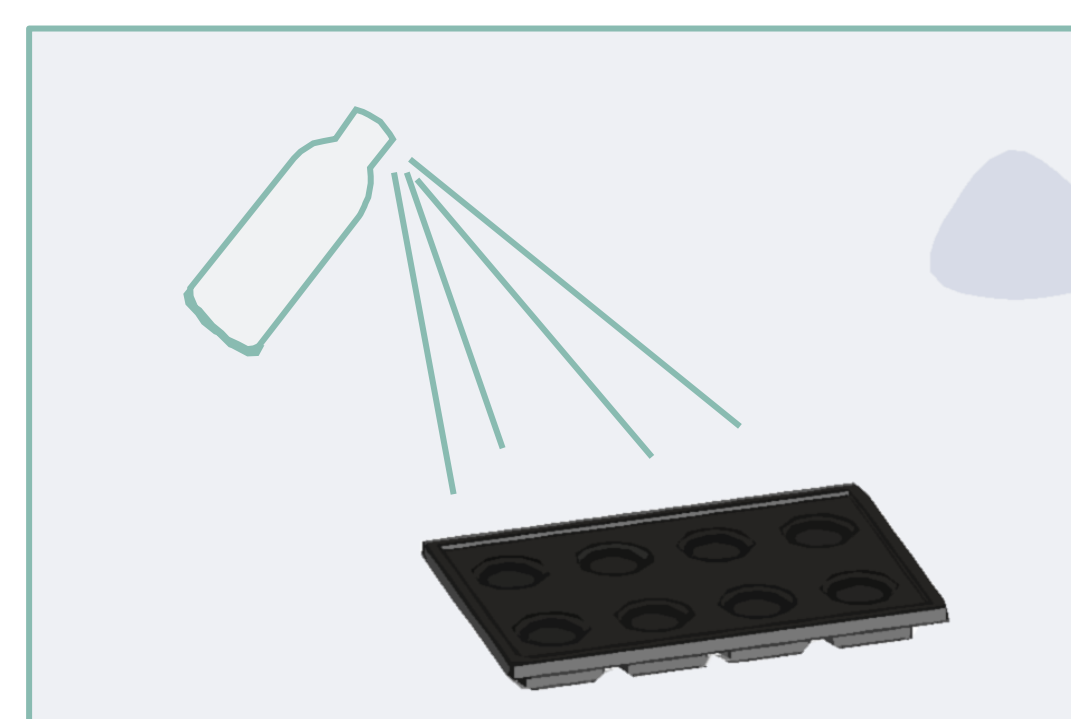
## Materials and Methods

### 1. Mold Master Design



- SolidWorks® used to create a negative mold.
- Material: Thermoplastic Polyurethane-95A (TPU-95A) filament.
- Printed on LulzBot Taz Workhorse Edition Printer.

### 2. Coating and Mixing

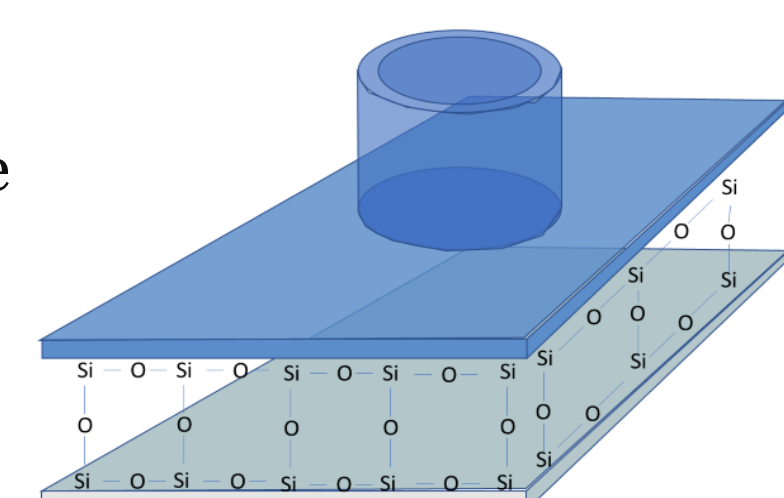


- MG Chemicals® Silicone Modified Conformal Coating Spray used to ensure Polydimethylsiloxane (PDMS) fully cured.
- SYLGARD™ 184 Silicone Elastomer mixed at 10:1 wt. % ratio and placed in desiccator for an hour.

### 3. Seeding and Curing

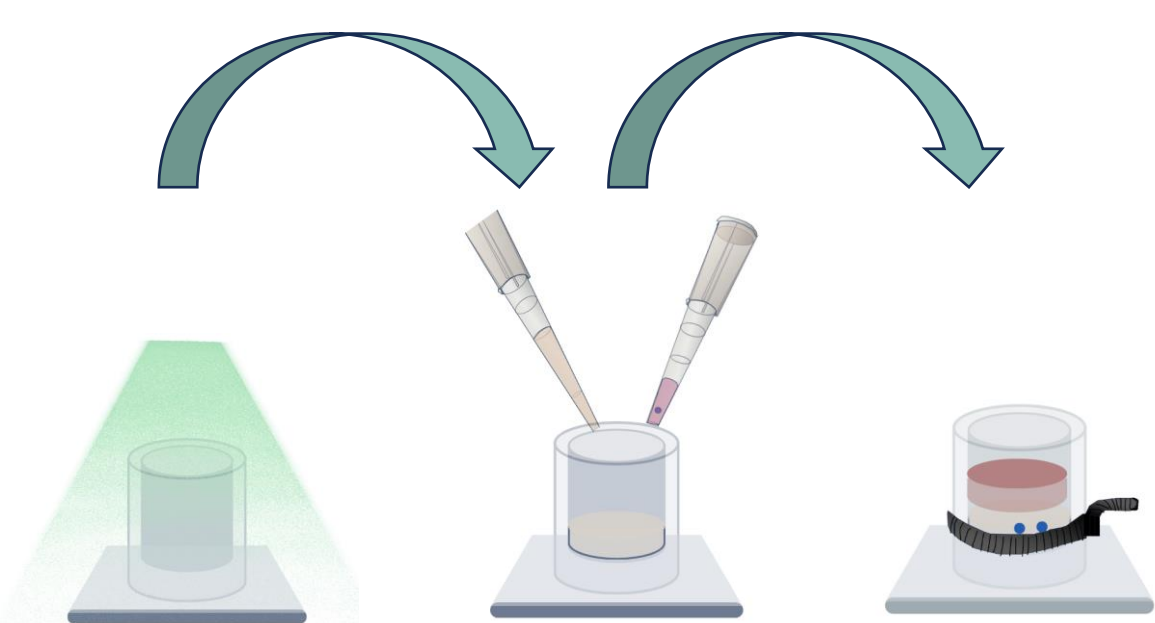


- MCF10A breast epithelial cells with nuclear GFP spheroids seeded at 1.5k cells in ULA 96-well plate and left overnight.
- PDMS cured at 65°C for two and half hours and bonded to 12-well plate lid using oxygen plasma treatment.



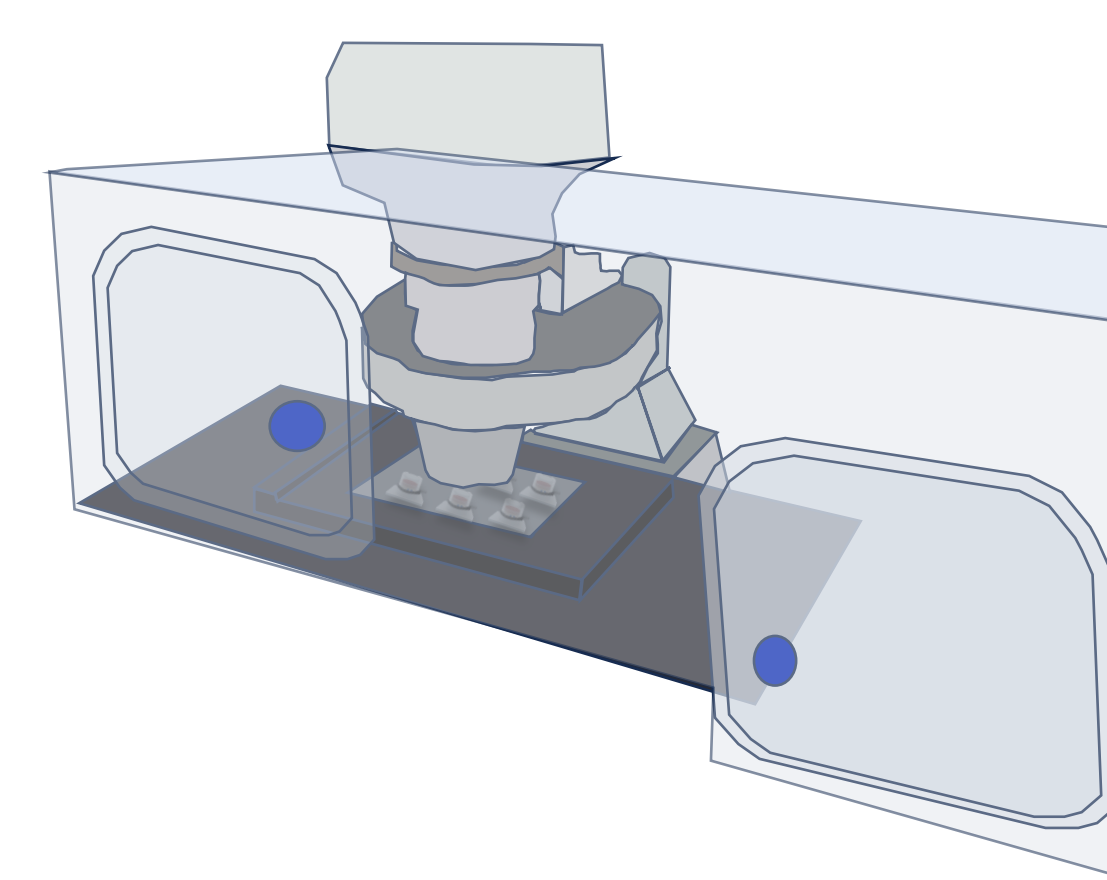
## Materials and Methods

### 4. Cleaning, Deposition, and Seeding:



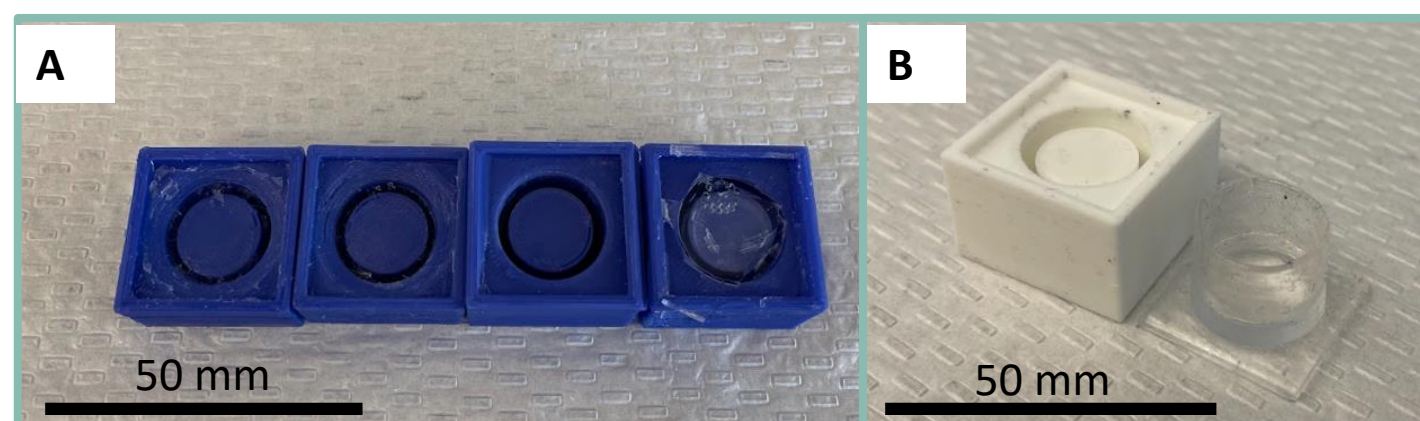
- PDMS cleaned using 1X PBS and UV crosslinking.
- plasma cleaning for 5 minutes.
- 50 µl of collagen deposited and allowed to polymerize for 30 minutes at 37°C.
- two spheroids seeded into gel with 50 µl collagen (45 min).
- 500 µl of CCM was added and the zip-tie was pulled tight.

### 5. Imaging



- Cells imaged using Zeiss AxioObserver microscope.
- We are modifying and improving our PDMS fabrication protocol to improve imaging capabilities.

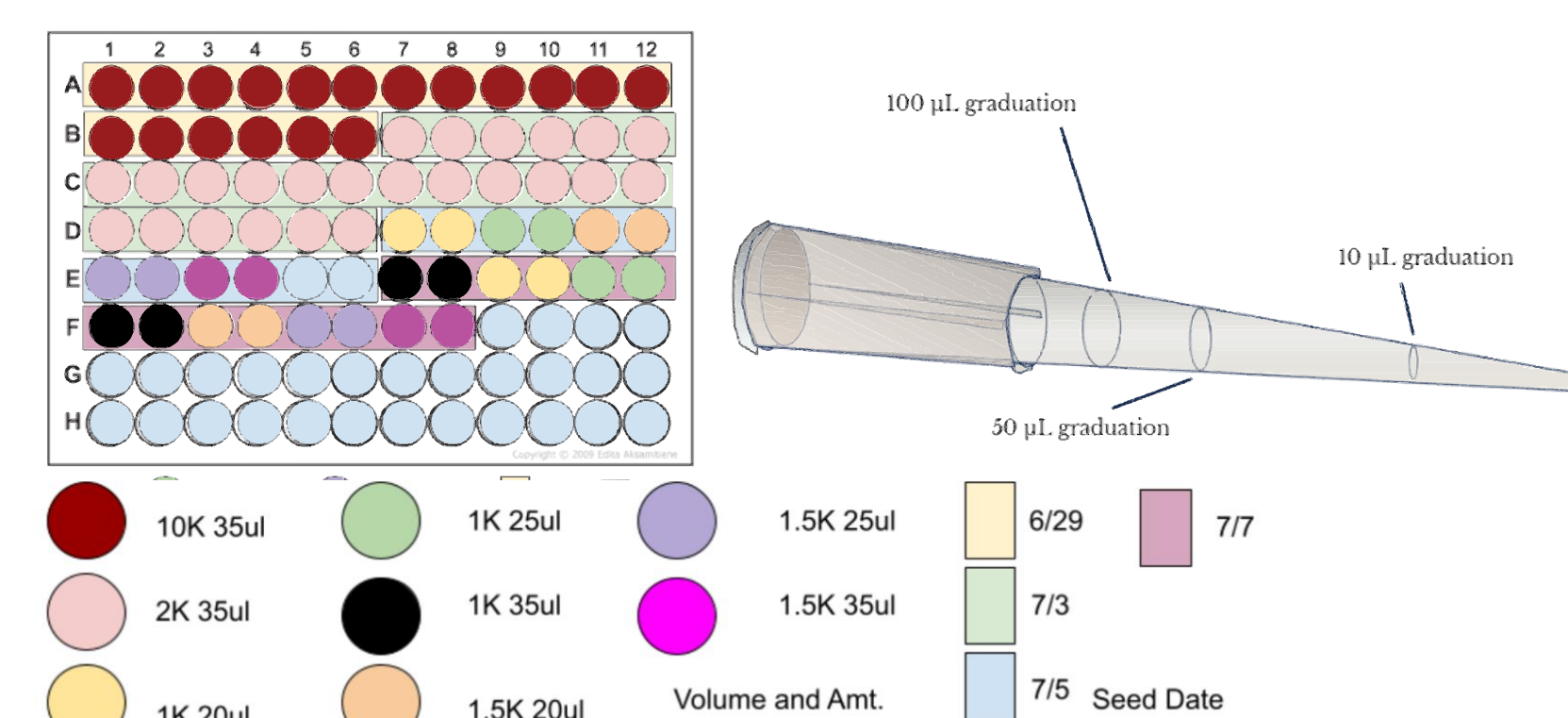
## Results



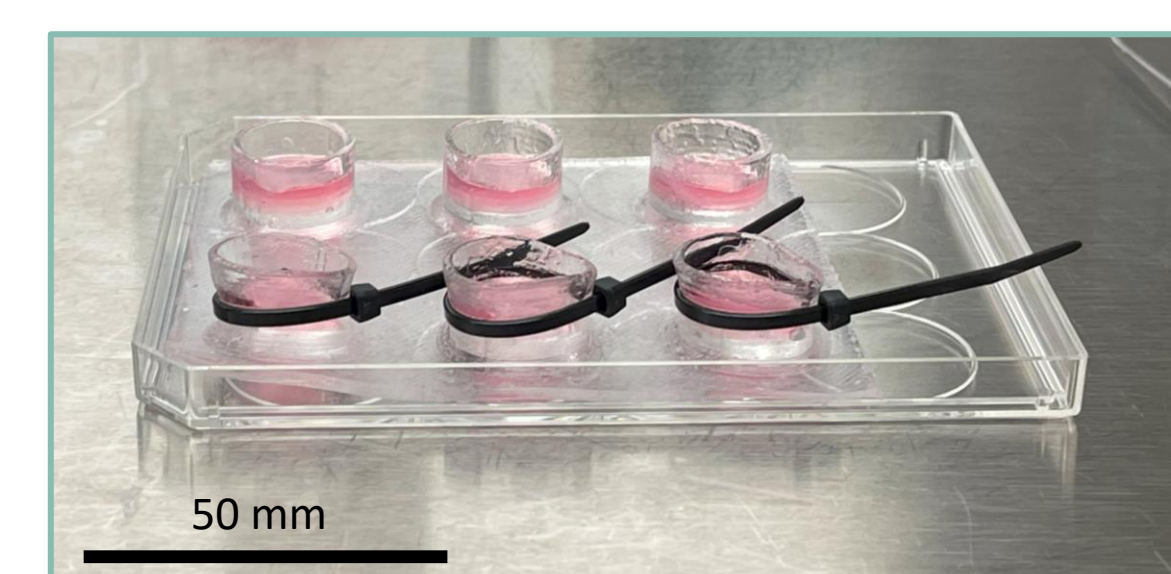
- **Filament Testing and Best Result:** Tested PETG, PLA, and TPU-95A filaments with no treatment, oxygen plasma treatment, and silanization. Flexible TPU-95A filament with silanization worked best to release PDMS well plate.

### •Spheroid Formation and Optimal Conditions:

Tested number of volume/cells for spheroid formation. Seeding 1.5K cells at 20 µl was most optimal for forming spheroids using ULA plates and MCF10As.

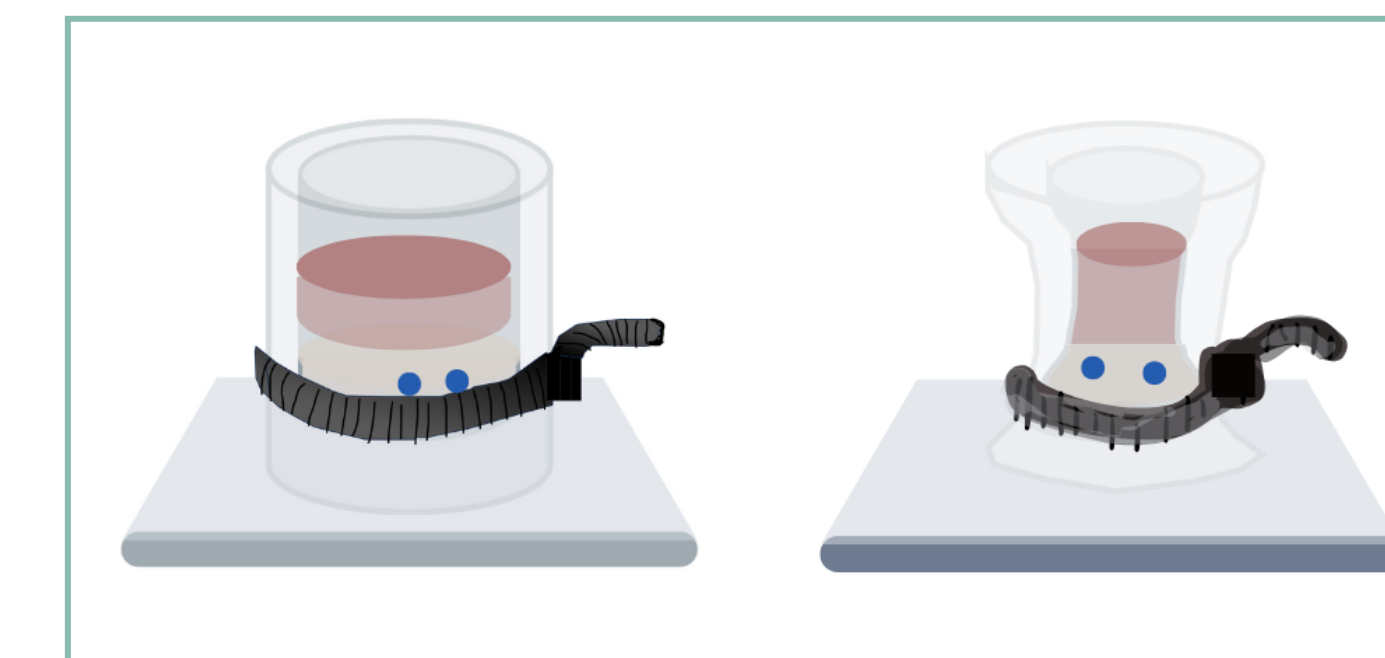


• **Imaging Results:** We are improving imageability of the well, including reducing the PDMS thickness at the bottom of the wells, using glass bottom single well plates to hold the PDMS, and seeding more spheroids into the collagen.



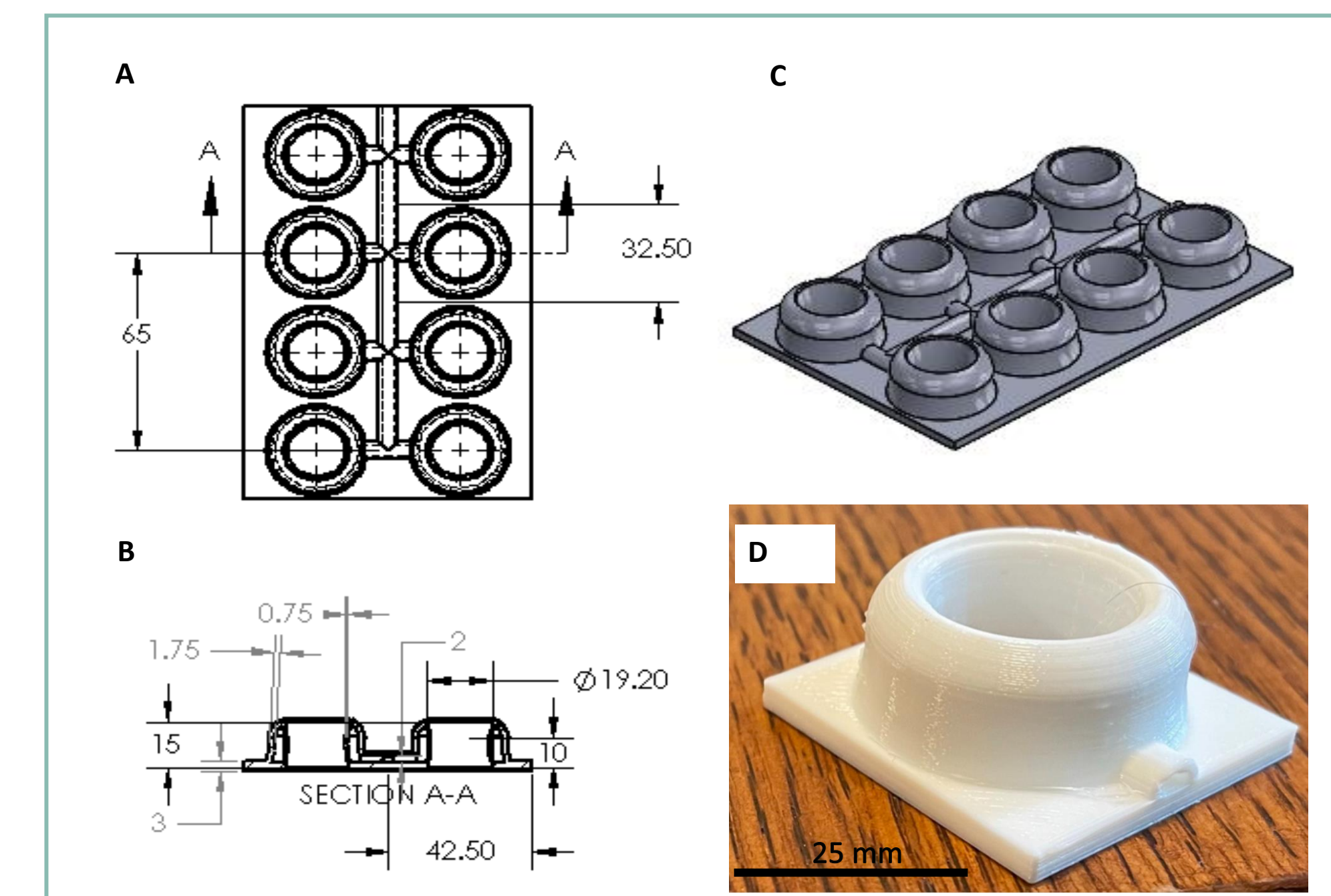
## Conclusion

- PDMS is a biocompatible, elastic silicone with good mechanical properties.<sup>2</sup>
- There are numerous descriptions of PDMS based devices that are used for novel cell compression on living cells, but many are microfluidic based.<sup>3</sup>
- Conventional cell culture methods in a bulk setting will provide more tools for studying living cells and the role of radial compressive forces in cancer mechanobiology.
- Currently, the only commercially available flexible cell culture plates available for conventional cell culture is BioFlex® from FlexCell, which are used for tensile testing.



## Future Work

- Eventually we will apply specific compression to normal and cancerous cell spheroids within a 3D collagen matrix, observing their behavior using time-lapse microscopy.



- With these experiments, we plan to examine:
  - ECM deposition and cross-linking
  - fiber alignment, length, and size
  - cellular changes to actin, myosin, and Rho-ROCK signaling.
  - Measuring traction forces
 These experiments will provide valuable insights into explaining the mechanisms by which radial compression contributes to tumor progression and metastasis.

## Acknowledgements

I would like to express my gratitude to everyone at the Pathak Lab for their warm welcome. I am also grateful to the Center for Engineering Mechanobiology (CEMB) and the National Science Foundation (NSF) for providing the funding that made this project possible. Also, a special thanks go to Patricia Widder and Huyen (Gwen) Nguyen for their excellent organization of this program.

## References

1. Bombonati, A., & Sgroi, D. C. (2011). The molecular pathology of breast cancer progression. *The Journal of pathology*, 223(2), 308-318.
2. Matsui TS, Wu H, Deguchi S (2018) Deformable 96-well cell culture plate compatible with high-throughput screening platforms. *PLoS ONE* 13(9): e0203448.
3. Onal S, Alkaiji MM, Nock V. Microdevice-based mechanical compression on living cells. *iScience*. 2022 Nov 9;25(12):105518. doi: 10.1016/j.isci.2022.105518

# Effects of Magnetic Field-Induced Alignment on Cellulose Nanocrystal and Soy Protein Nanocomposite Mechanical Properties

Daichi Kobayashi<sup>1</sup>, Jerry Wang<sup>1</sup>, Marcus Foston<sup>1</sup>

<sup>1</sup>Department of Energy, Environmental, and Chemical Engineering, Washington University in St. Louis

## INTRODUCTION

- Biocompatible protein-based films are potential alternatives to conventional plastics
- Protein films tend to have inferior mechanical properties compared to plastic films
- Incorporating cellulose nanocrystals (CNCs) from biomass into protein nanocomposite films enhances strength, stiffness, hydrophobicity, and barrier properties
- Suspended CNCs align perpendicularly to strong external magnetic fields, inducing anisotropic mechanical and optical properties while further enhancing barrier properties
- Applications range from food packaging to tissue engineering to biological sensors
- Goal: examine the effects of magnetic field exposure on CNC - Soy protein isolate (SPI) nanocomposite mechanical properties to confirm CNC alignment (and alignment effects) within nanocomposites

## MATERIALS AND METHODS

- CNCs were isolated from paper pulp via acid-catalyzed hydrolysis followed by centrifugation
- CNCs were analyzed via
  - FTIR to verify chemical identity
  - Atomic force microscopy (AFM) to characterize morphology and size
  - DLS to determine zeta potential (dispersive properties)
- Nanocomposite suspensions were made from CNCs, SPI, glycerol, and water
- Nanocomposite suspensions were poured into dog bone-shaped molds
- Nanocomposite suspensions were left to dry either inside or outside MRI
- Molds in MRI were oriented perpendicular and parallel to MRI axis
- Dry nanocomposite films were analyzed via
  - SEM to determine surface morphology
  - Uniaxial mechanical testing to determine Young's modulus (stiffness) and ultimate tensile strength

## PROJECT OVERVIEW

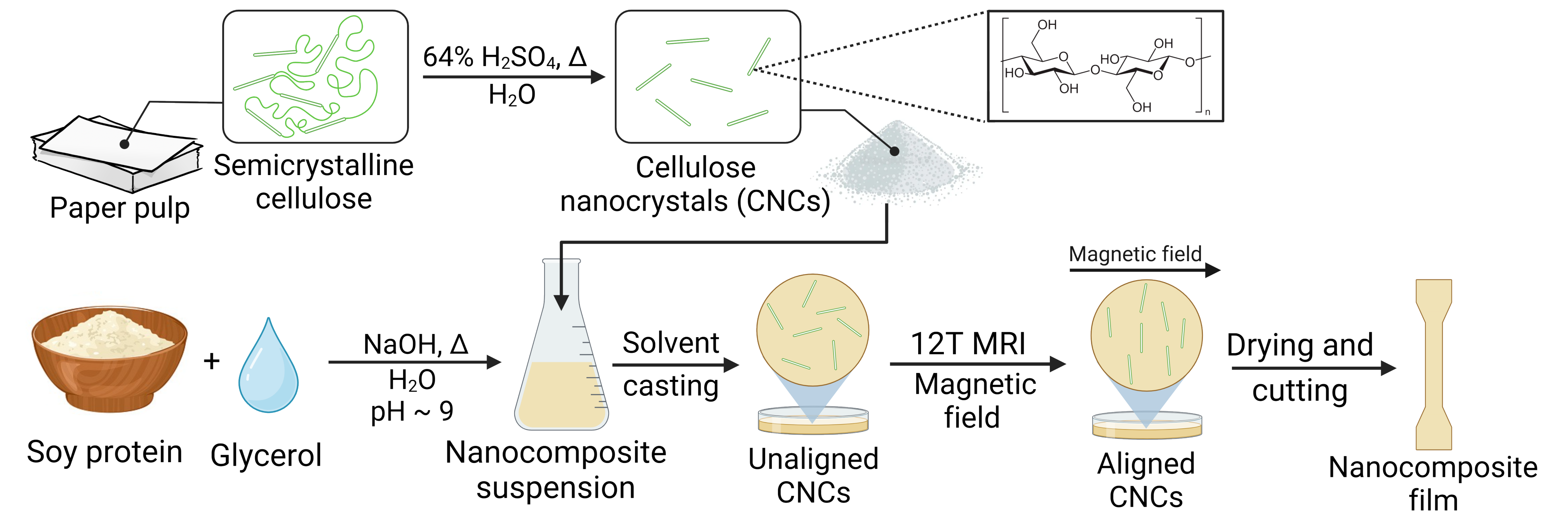


Figure 1: Overview of CNC synthesis and nanocomposite production.

## RESULTS - CNC CHARACTERIZATION

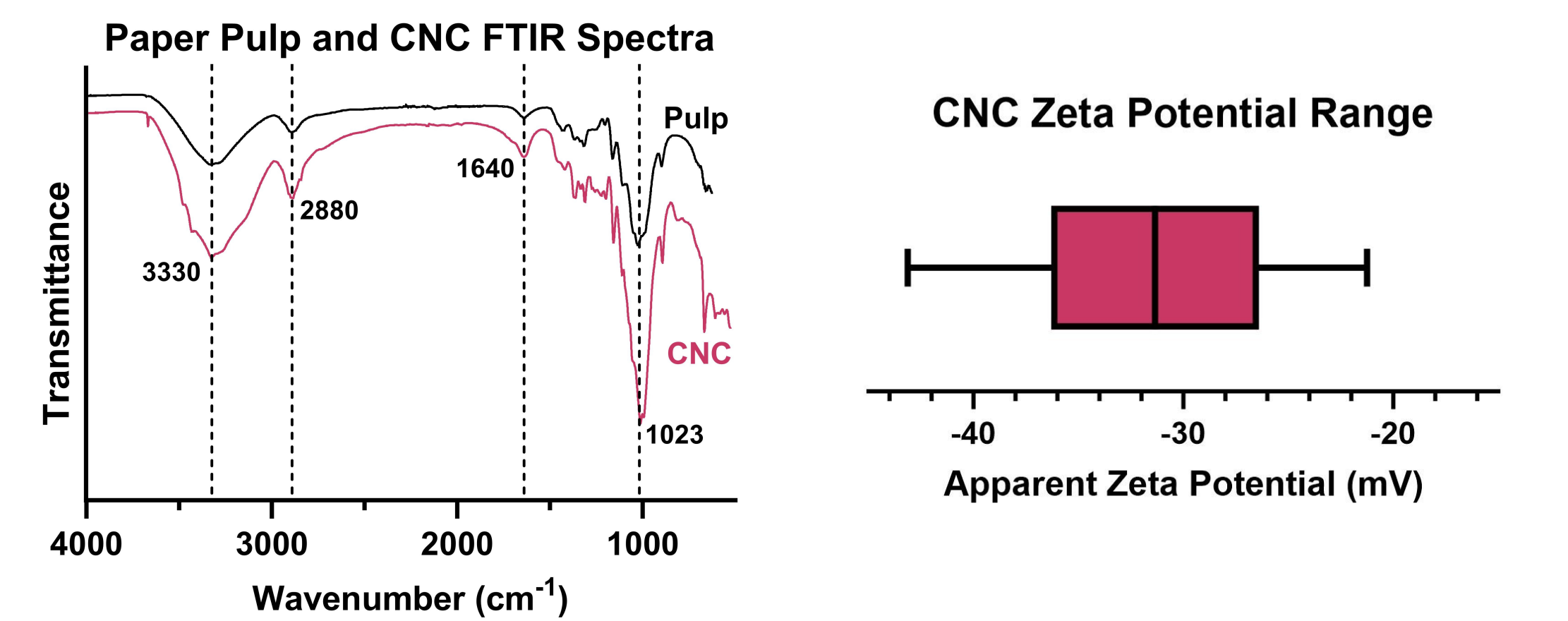


Figure 2: FTIR spectra of CNCs and feedstock paper pulp.

Figure 3: Zeta potential of CNCs. The magnitude of zeta potential can indicate dispersive properties.

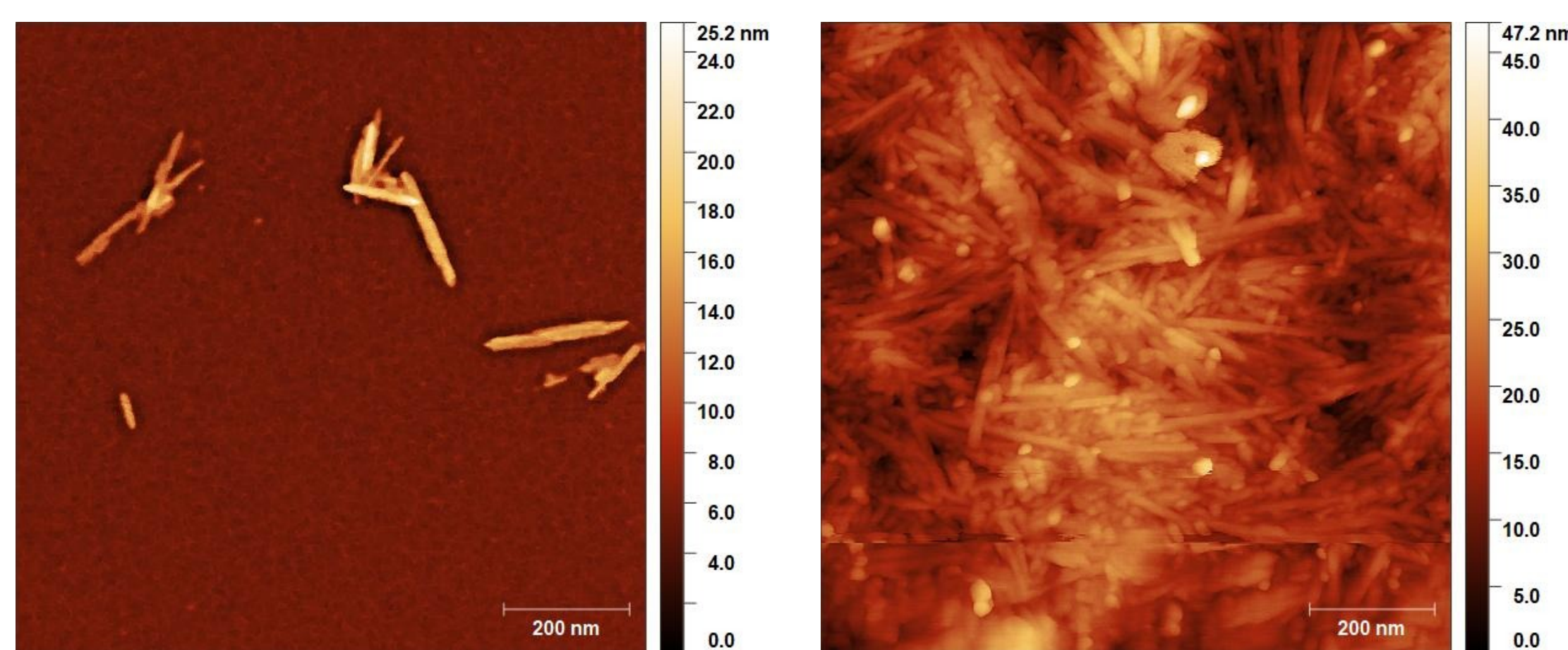


Figure 4: AFM micrograph of individual CNCs

Figure 5: AFM micrograph of CNC clusters

### FTIR

- CNCs have expected chemical properties, strongly resembling feedstock cellulose pulp

### DLS

- Negative zeta potential indicates presence of sulfate groups resulting from H<sub>2</sub>SO<sub>4</sub> hydrolysis
- In suspension, CNCs have good dispersibility

### AFM

- CNCs are rodlike and between 100 - 1000 nm in length

CNC properties conform with expectations from literature; CNCs should thus be capable of reinforcing nanocomposites.

## RESULTS - ALIGNMENT IMAGING

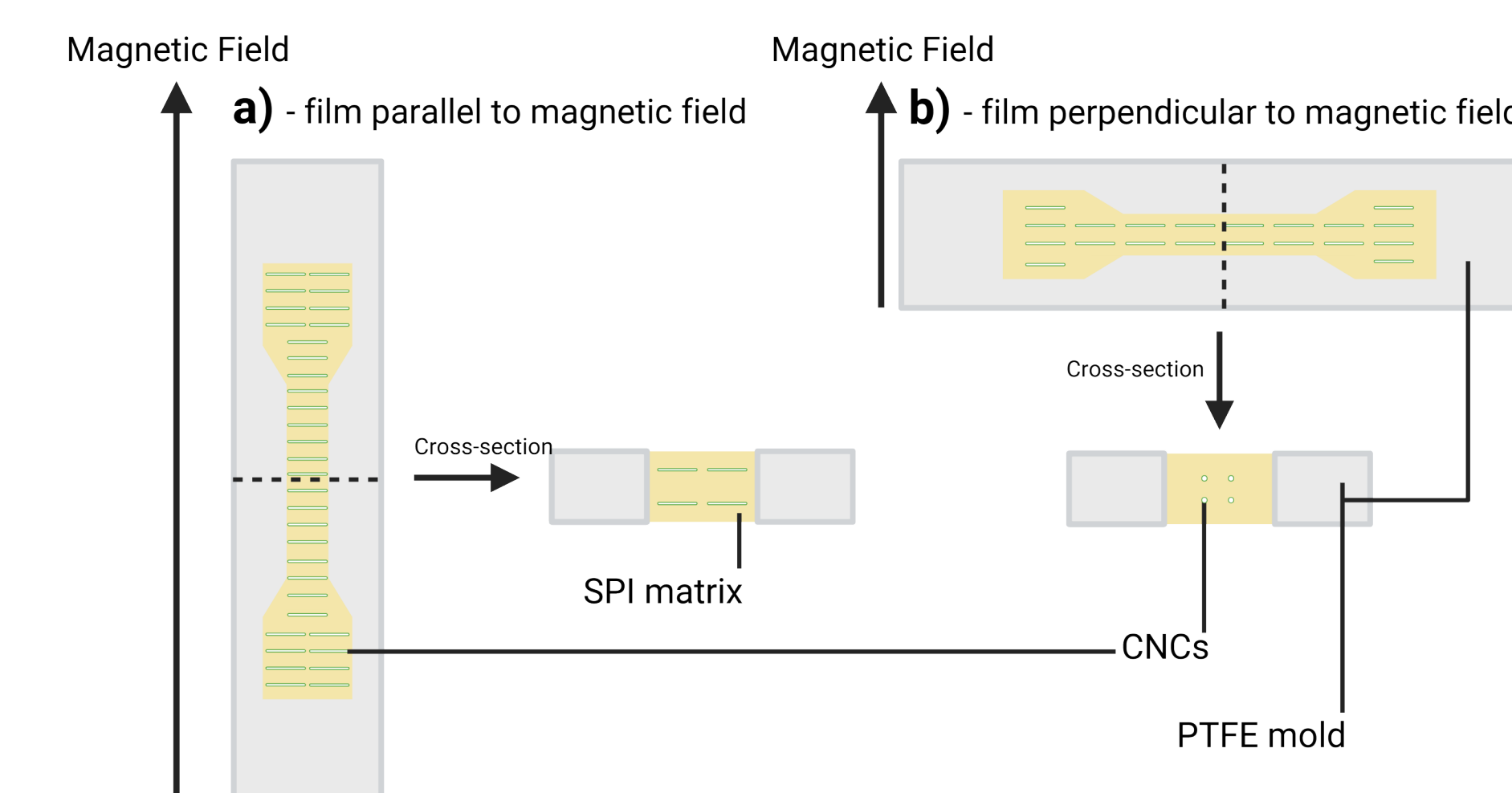


Figure 6: Diagram illustrating expectations of CNC appearances in SEM micrographs if alignment were to occur. CNCs appear as more visible rods in case (a), while CNCs appear as less visible specks in case (b)

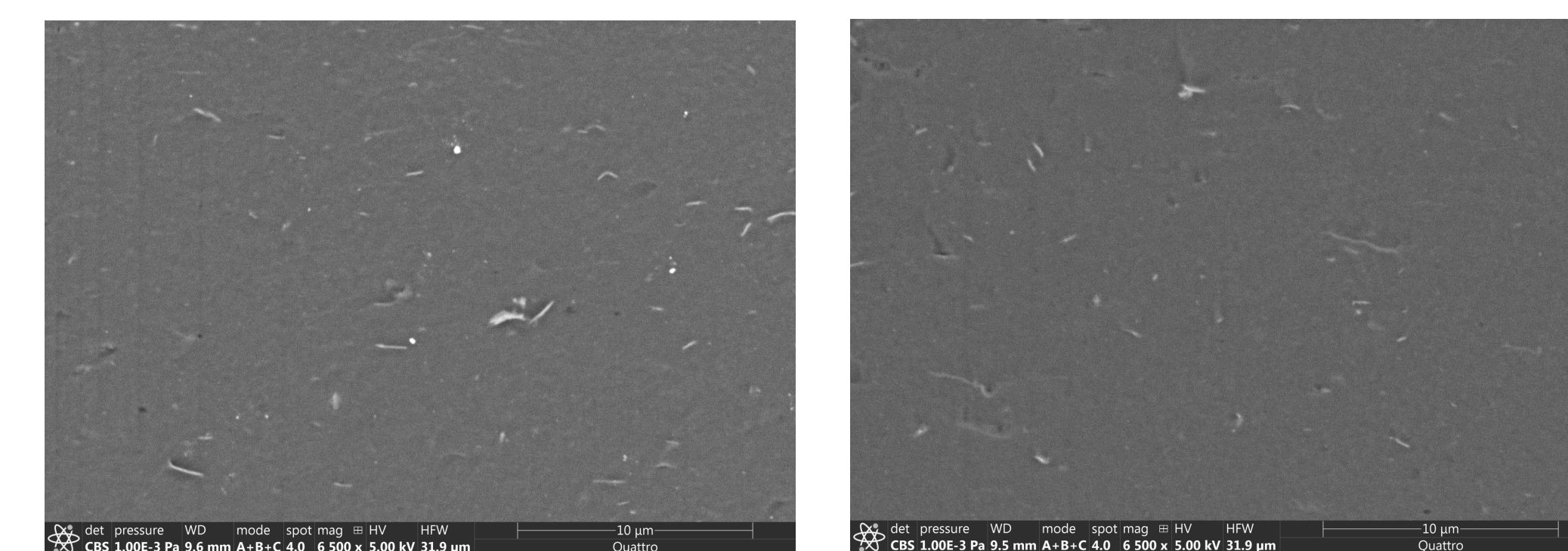


Figure 7a: SEM micrograph of an equatorial cross-section of a film cast parallel to the magnetic field, corresponding to (a) from Figure 6

Figure 7b: SEM micrograph of an equatorial cross-section of a film cast perpendicular to the magnetic field, corresponding to (b) from Figure 6

- Visual differences between SEM micrographs provide weak support for CNC alignment
- More images and quantitative image analyses will be needed to verify the viability of SEM images as direct evidence of alignment

## RESULTS - MECHANICAL DATA

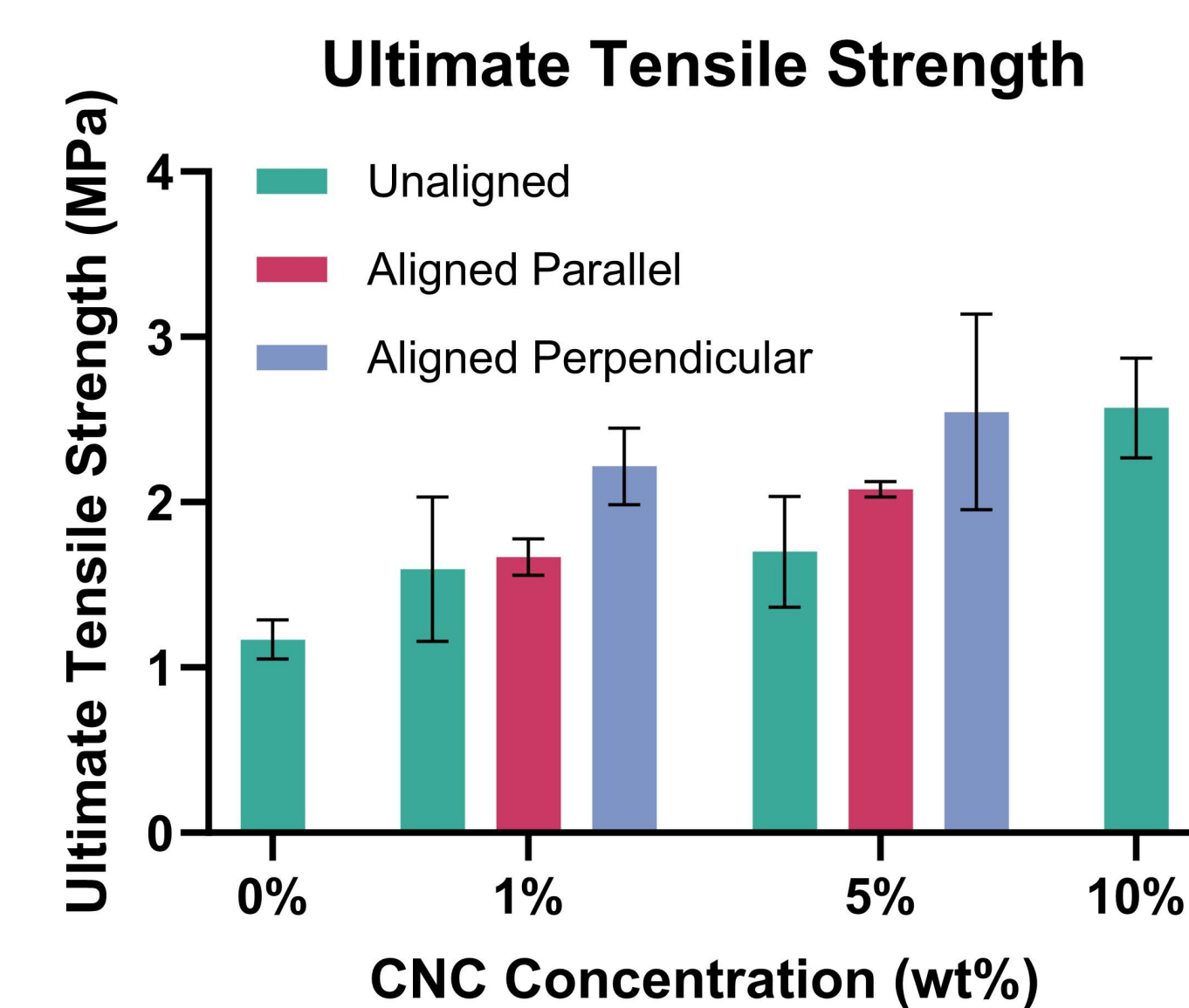


Figure 8: Ultimate tensile strength of CNC films dried with and without magnetic field exposure.

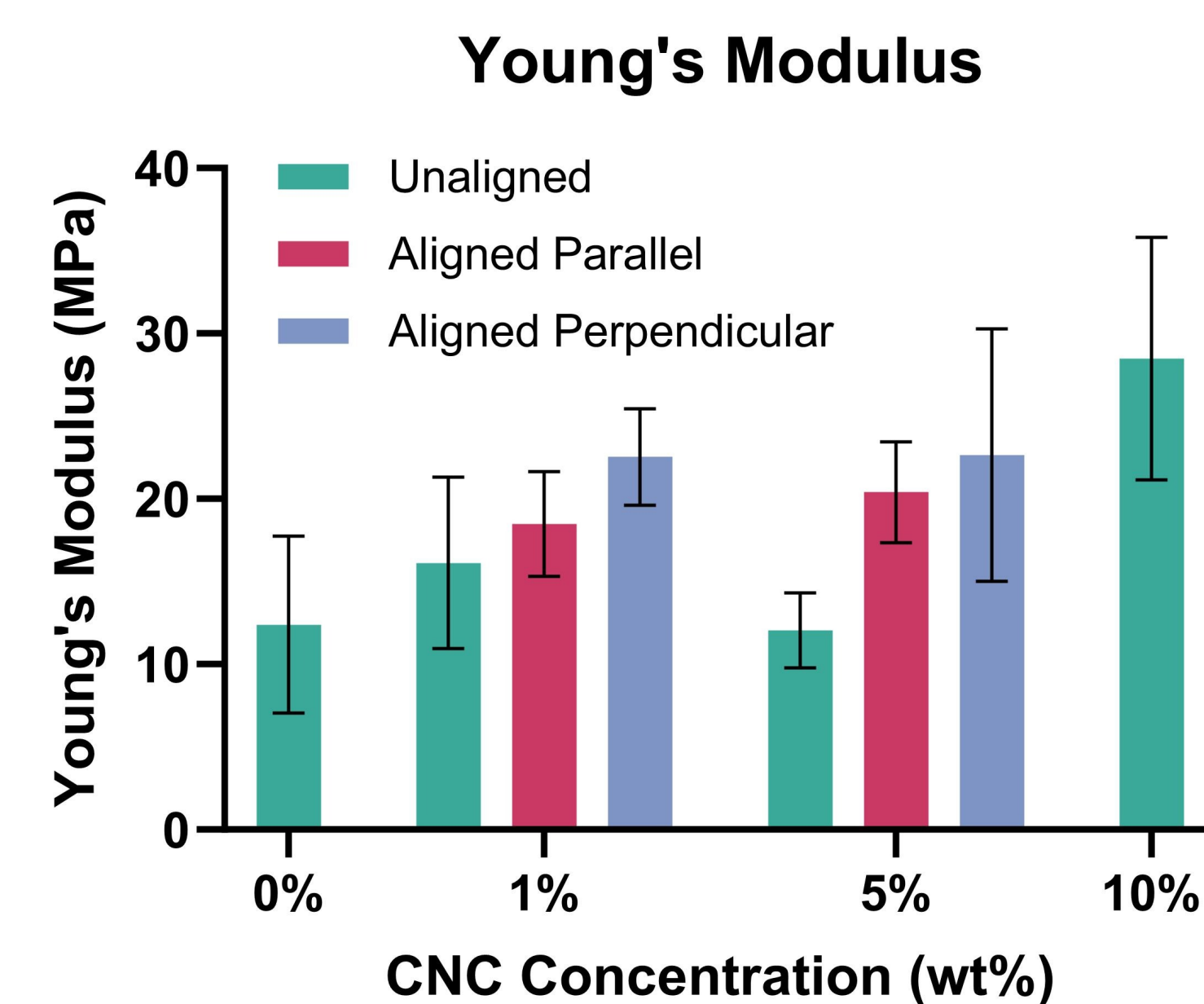


Figure 9: Young's modulus of CNC films dried with and without magnetic field exposure.

## DISCUSSION

### Mechanical Properties

- Increased CNC concentration tends to increase mean ultimate tensile strength (UTS) and Young's modulus
- UTS increases significantly between the 1% parallel and perpendicular conditions, by approximately 30%
- Mean UTS increases by approximately 20% between the 5% parallel and perpendicular conditions
- Mean Young's modulus tends to increase between the parallel and perpendicular conditions
- Mean parallel and perpendicular UTS and Young's modulus tends to increase between the unaligned and aligned conditions
- Different mechanical properties for parallel and perpendicular conditions suggest mechanical anisotropy, which is an indicator of successful alignment

### Future Work

- Improving film processing protocols is necessary to reduce standard deviation and minimize batch effects
- Water droplet contact angles of films should be tested to quantify hydrophobicity
- Water vapor permeability tests should be initiated to quantify gas barrier properties

## ACKNOWLEDGEMENTS

The author would like to thank the Center for Engineering MechanoBiology, Chemical and Environmental Analysis Facility, Institute for Materials Science and Engineering, Small-Animal Magnetic Resonance Facility, Dr. James Quirk, and Dr. Marcus Foston

## Flow fields in connector based vascular anastomosis

Alexandra Z. Pérez López<sup>1</sup>, Yuxuan Huang<sup>2</sup>, Xiaowei Li<sup>3</sup>, Justin M. Sacks<sup>3</sup>, Guy Genin<sup>2</sup>

University of Puerto Rico- Mayagüez<sup>1</sup>, Washington University in St. Louis<sup>2</sup>, Washington University School of Medicine in St. Louis<sup>3</sup>

**Introduction:** Vascular and reconstructive surgery often require vascular anastomosis, in which two severed blood vessels are reconnected to restore blood flow. The standard of care for anastomosis requires that the vessels be sutured around their periphery in such a way as to ensure continuous intimal contact. These procedures require extensive expertise and are highly time consuming even for expert surgeons. A possible approach that has been proposed for making these procedures more efficient is to insert a connector on the inner lumen of the two severed vessels, and lock this into place with a connector that passes around the outer diameter of the vessel (Figure 1). While substantially more efficient, the connector can cause perturbations to blood flow that lead to occlusion of the vessel connection by promoting thrombosis. The goals of this study were therefore to identify the features of flow that lead to the development of thrombosis, and to identify ways to possibly alleviate this complication.

**Materials and Methods:** Numerical simulations were performed to estimate the vessel distension associated with insertion of a connector between the free ends of two severed blood vessels, and to assess how the connector and distension affected flow fields and the likelihood of thrombosis. Vessels were modeled as cylindrical, incompressible, isotropic, linear elastic tubes, and connectors as rigid and rotationally symmetric. The outer diameter of the connector was greater than the inner diameter of the vessel, causing distension to a shape that was estimated using axisymmetric finite element analysis. This shape served as input for axisymmetric computational fluid dynamics simulation of blood flow through the vessel and connector. Blood rheology was approximated using the Bird-Carreau model, which accounts for shear-thinning and viscoelasticity. The size and shape of the connector were studied parametrically. The inlet condition was defined by a centerline velocity. The outlet boundary condition was prescribed by the two element Windkessel model. The likelihood of thrombus formation was assessed using previously published models that account for the time and spatial extent of exposure of blood to strain rates that are pathologically high (strain rate  $> 1000$  /s) and pathologically low (strain rate  $< 50$  /s). Equations were solved in the COMSOL Multiphysics environment (version 6.1, COMSOL, Burlington, MA) using scripts in Matlab and Simulink (version 2023a, MathWorks, Natick, MA), and standard convergence studies were performed.

**Results and Discussion:** After analyzing blood flow patterns, pressure distributions, and wall stresses, regions of abnormal flow and potential sites of thrombus formation were identified. The presence of a connector between ends of the severed vessel led to elevations of shear rates at the leading corner of the connector, and to reduced shear rates near the wall at that edge (Figure). These pathological flow fields could be attenuated by distending the vasculature sufficiently far. Effects were independent of the length of the connector, and with the thickness of the vessel over the physiologically relevant range. Rounding the edges of the connector reduced peak shear strain rates. The outlet of the connector was associated with flow stagnation and low shear rates, but not with pathologically high shear rates. In all cases, thickening of the connector worsened flow fields, while distension of the vessel improved flow patterns up to a limit beyond which the inner surface of the connector lay outside of the original inner diameter of the vessel. These results provide guidance for the selection and design of vasculature connectors.

**Conclusions:** Results demonstrate the significance of the choice of vascular connector on hemodynamics in vascular networks. Simulations revealed a strong negative effect of connector thickness, which can be attenuated by distension of the blood vessel. Results also show a secondary effect of the sharpness of the leading edge of the connector, and no effect of the length of the connector. Taken together, these results provide support for the feasibility of performing connector-based anastomosis and provide key guidance for the design of anastomosis connectors.

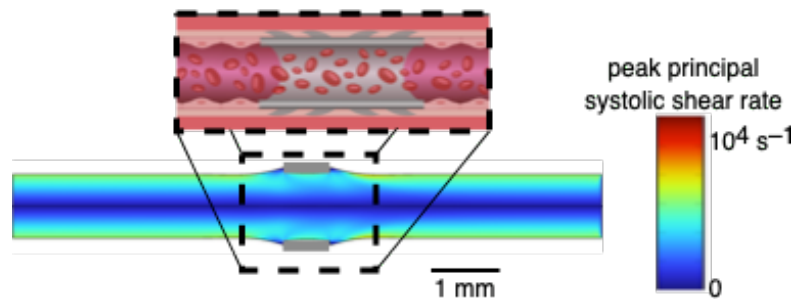
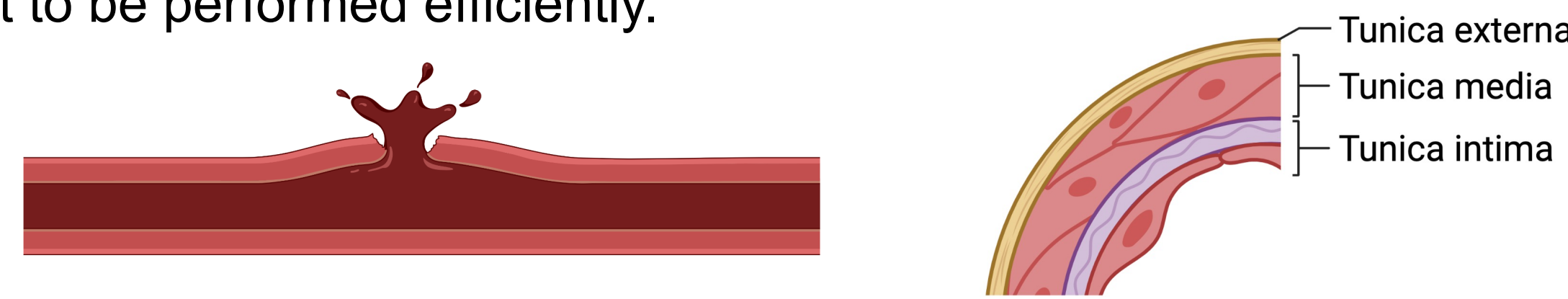


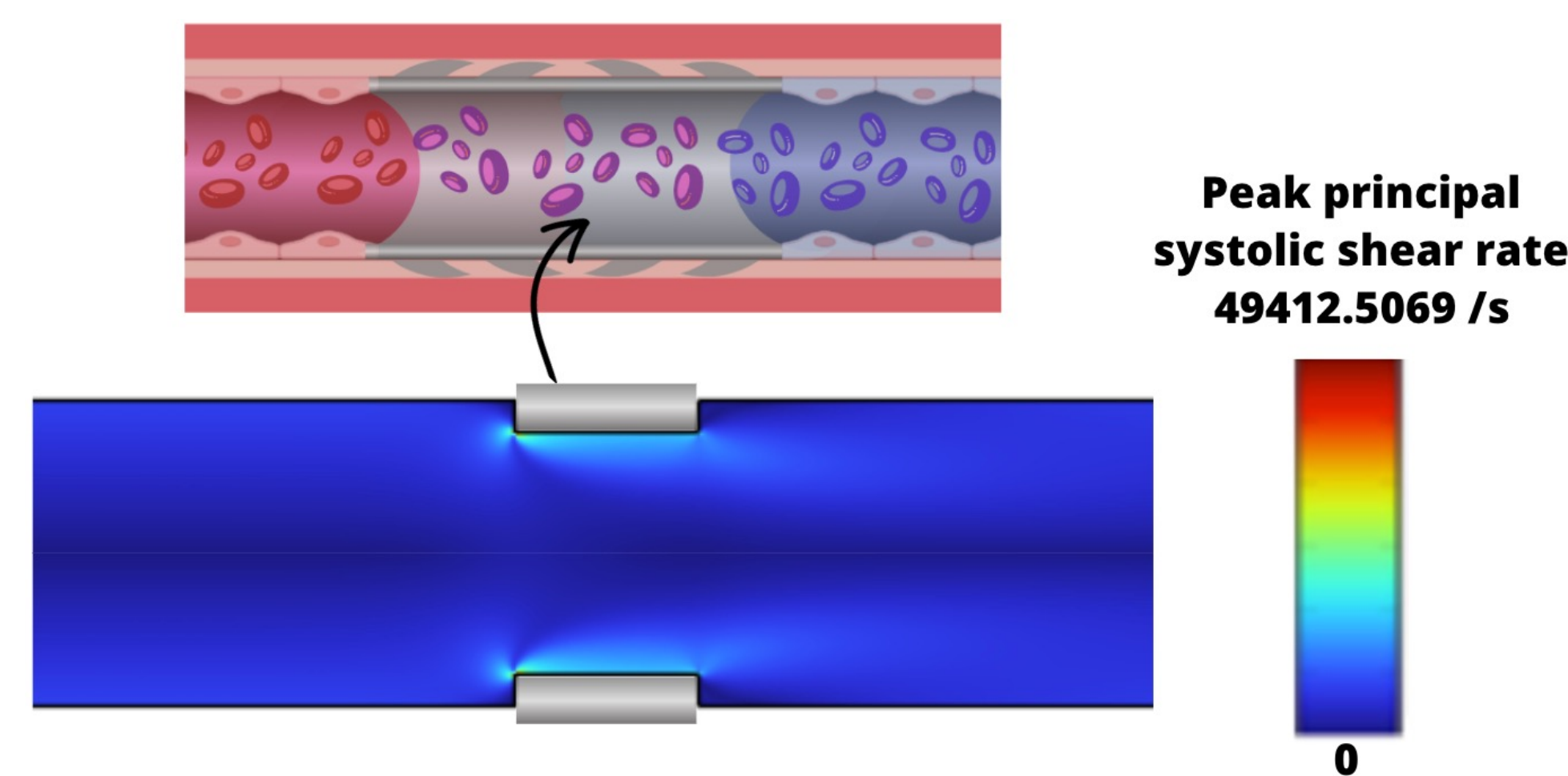
**Figure 1.** Vascular anastomotic connector, and representative flow fields arising from its insertion to connect two severed blood vessels.

## Introduction

- Anastomosis is a surgical practice essential in the performance of vascular and reconstructive surgery. Vascular anastomosis consists of the connection between two severed blood vessels with the purpose of restoring blood flow. This procedure requires exhaustive medical skill, expertise, and time from the surgeon for it to be performed efficiently.



- In an attempt of making these procedures more effective, a sutureless anastomotic device was proposed. This connector is inserted in the tunica intima of the blood vessels, enabling the connection of two free vascular ends. The main concern is that having the connector in the vasculature increases blood flow shear rate, which leads to perturbations and obstructions of the vessels and consequently possible thrombus formation. The goal of this research is to identify the aspects of blood flow that lead to the development of thrombosis, and to identify ways to reduce and ease this complication.



## Methods

The blood rheology for the vasculature was modeled with the Bird-Carreau constitutive law:

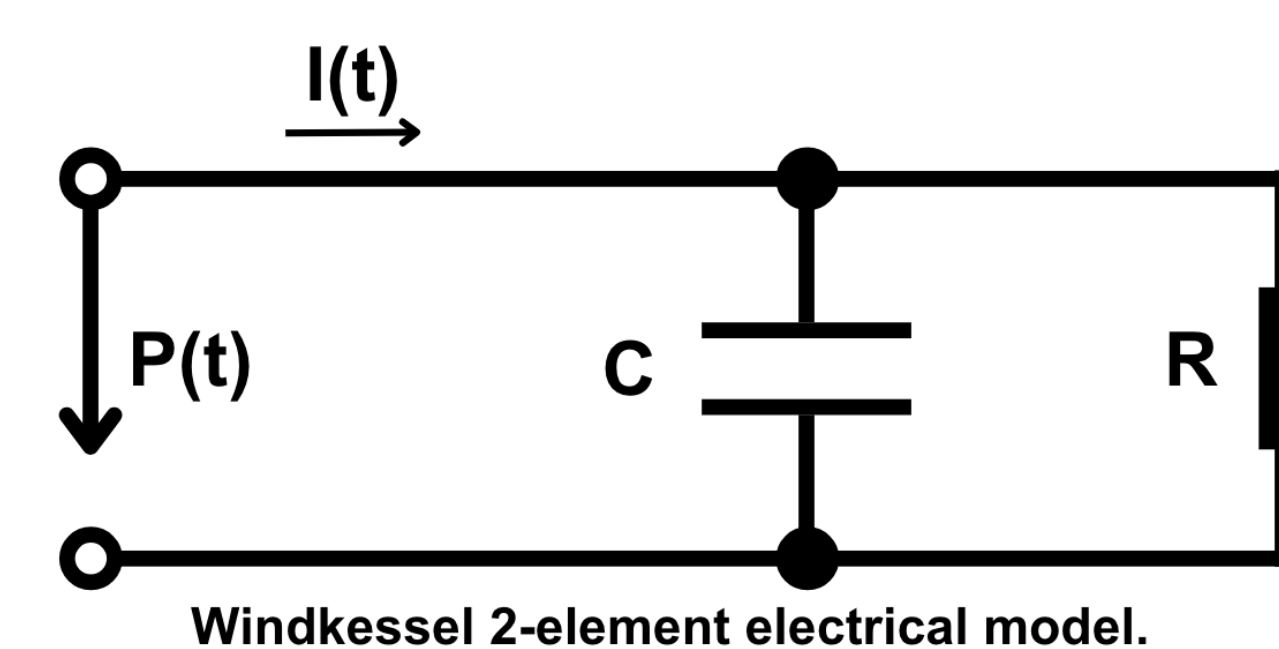
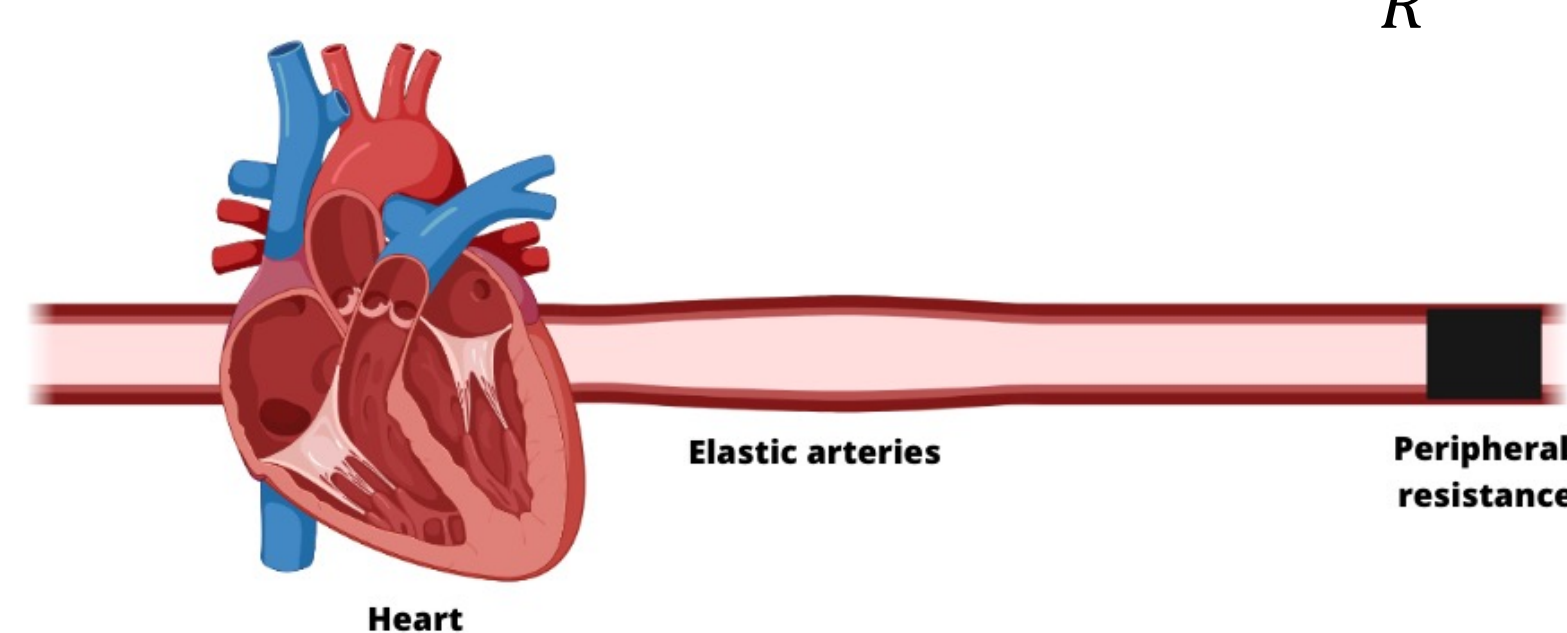
$$\mu_{eff} = \mu_{inf} + (\mu_0 - \mu_{inf}) [1 + (\lambda\dot{\gamma})^2]^{\frac{n-1}{2}}$$

The inlet boundary condition was defined by a centerline velocity function that simulated heart rate:

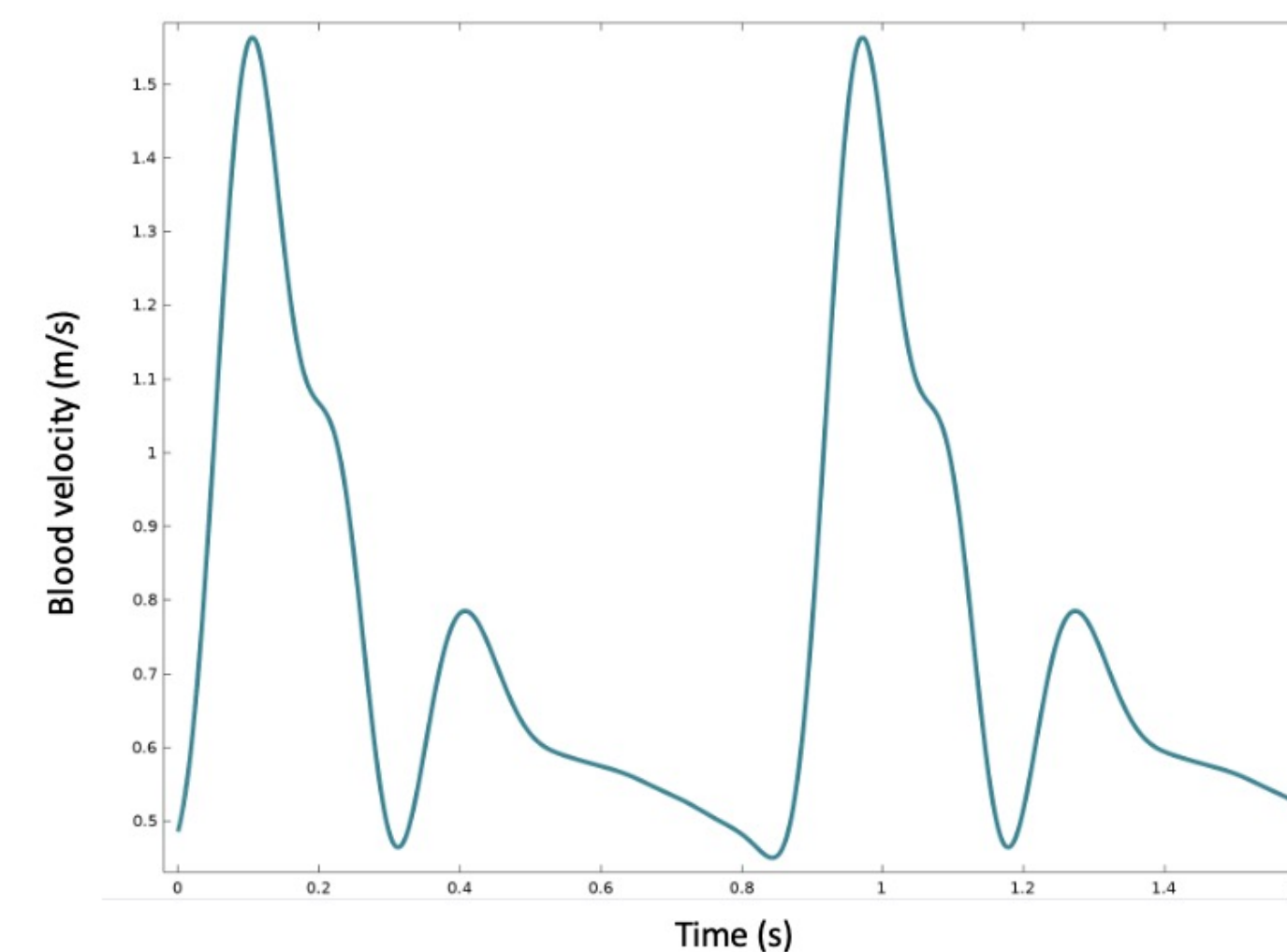
$$f(t) = a_0 + \sum_{n=1}^{\infty} a_n \cos(\omega n t) + \sum_{n=1}^{\infty} b_n \sin(\omega n t)$$

The outlet boundary condition was described using the Windkessel Model, which takes into consideration arterial compliance, peripheral resistance, and blood's inertia:

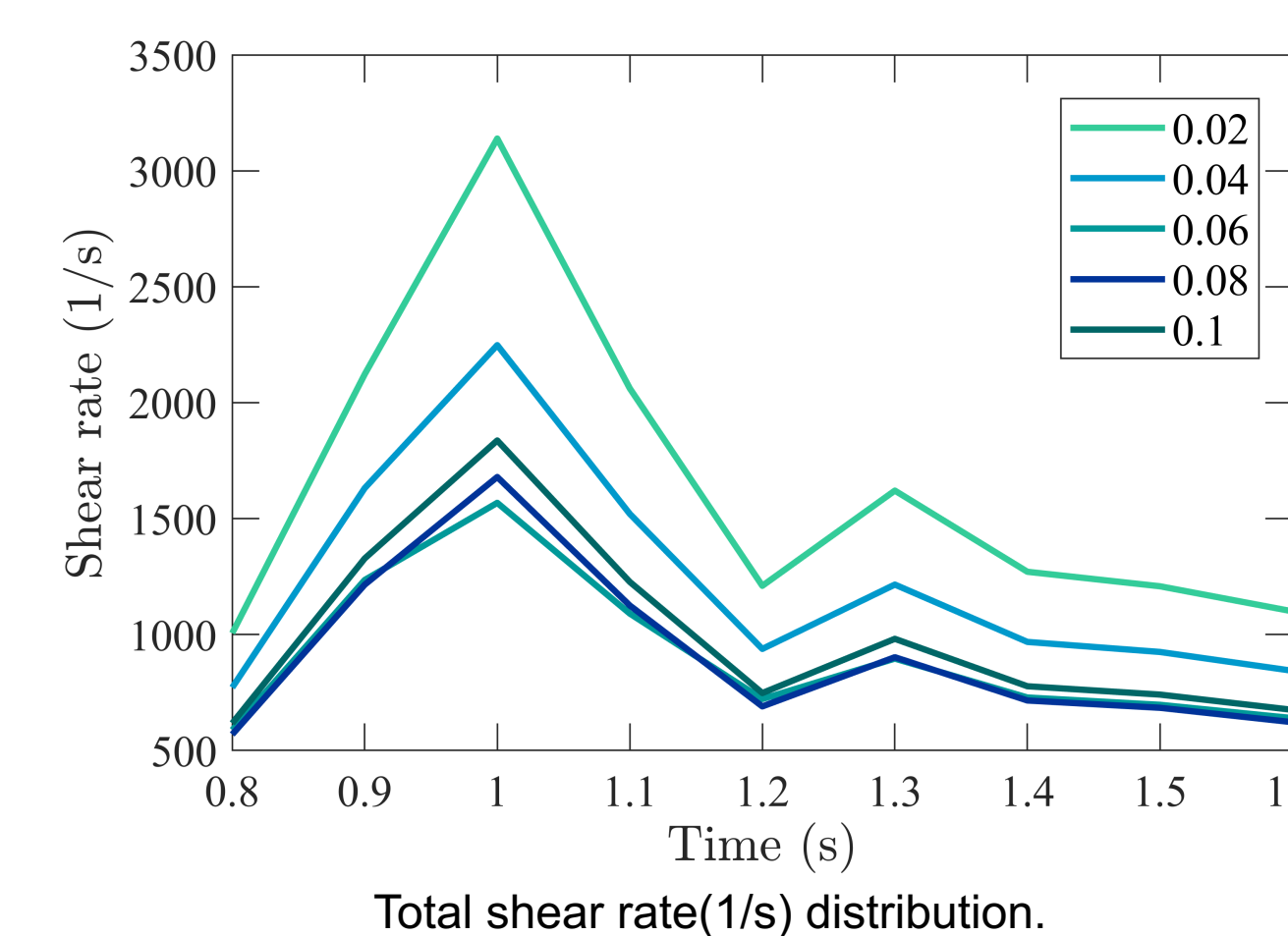
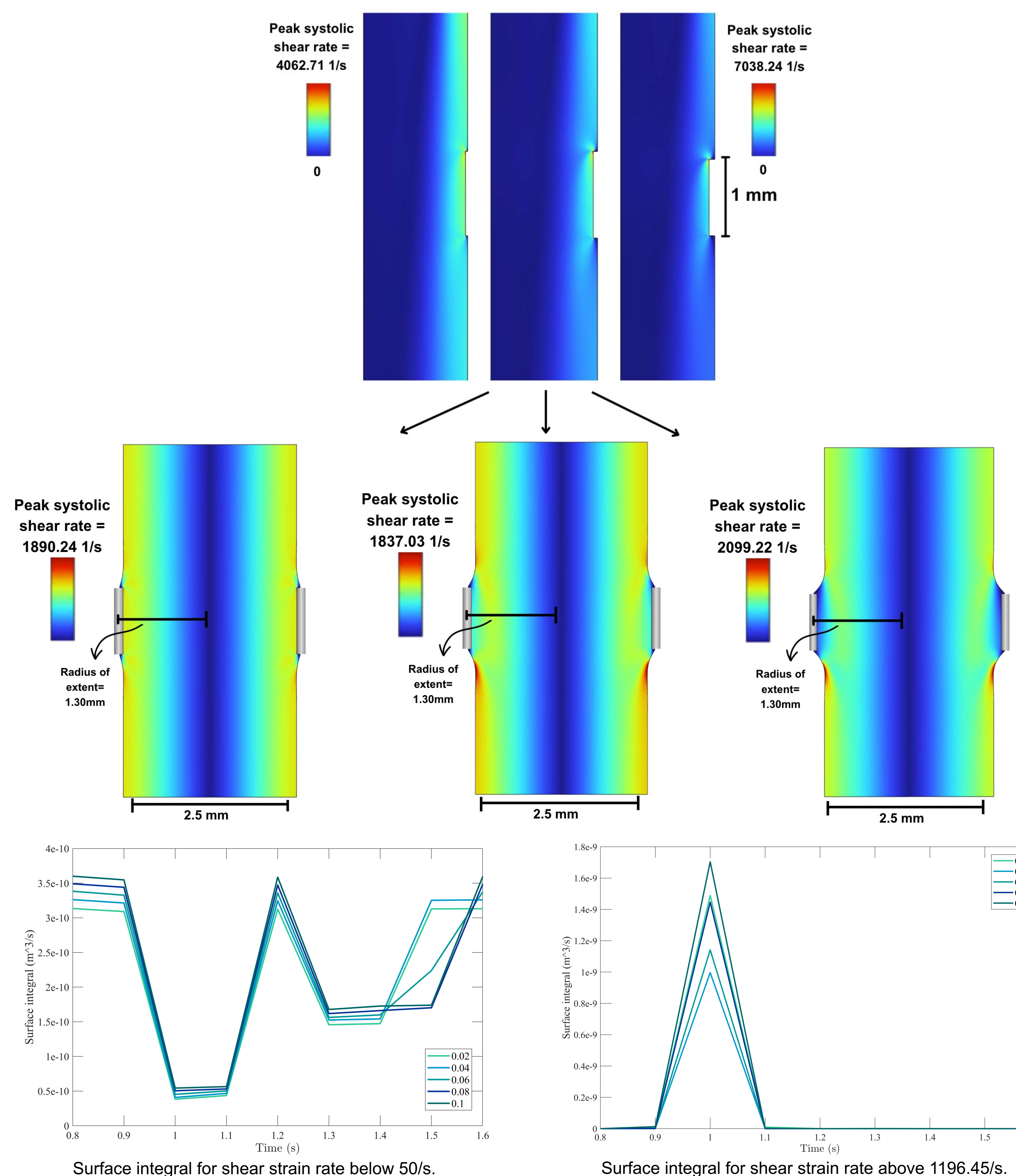
$$I(t) = \frac{P(t)}{R} + C \frac{dP(t)}{dt}$$



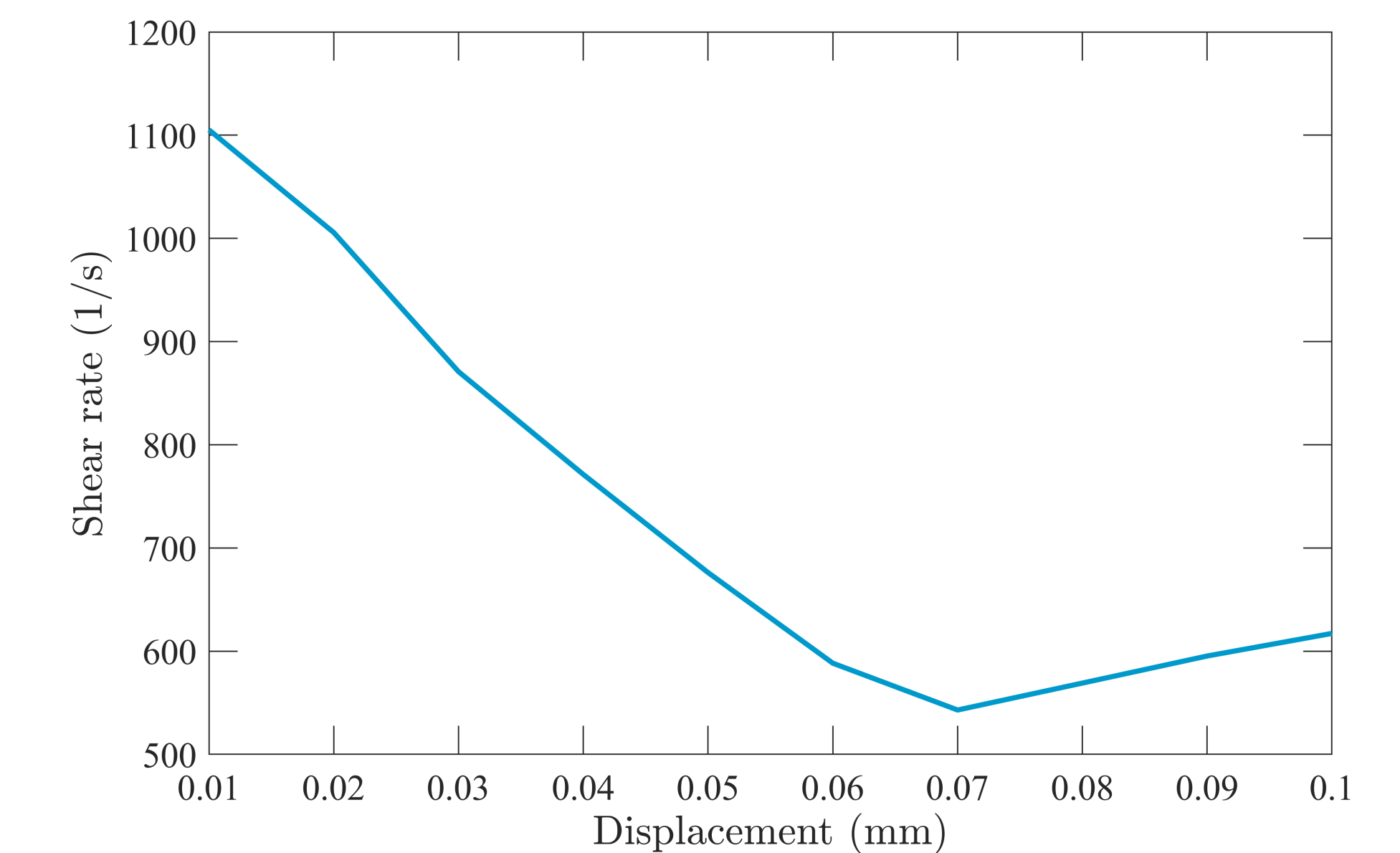
## Blood velocity



## Shear rate distributions



## Maximum shear rate versus displacement



Maximum shear rate at 0.8 seconds from 0.01mm-0.1 mm displacement.

## Discussion and conclusion

- Blood flow patterns, pressure distributions, and wall shear stresses were analyzed. Having the connector in the vasculature caused a perturbation in the blood flow, which led to significantly increased blood pathological shear rates.
- After studying the effects of distension of the vasculature in the flow shear rate, it was determined that it substantially reduced the pathological shear rate of the blood flow.
- A parameter sweep of the radius of the distension was performed and it showed that the shear rate was reduced as the inner surface of the connector was placed past the outside diameter of the vessel. However, distending the vasculature too far past the outer diameter of the vessel induced a higher shear rate. This could be attributed to the fact that the distension may have caused a possible sharper curvature.
- It was shown that increasing the thickness of the connector increased the blood flow shear rate and possible areas of recirculation in the corners of the connector arised.
- These simulations are key for the understanding of the viability of the connector and therefore the improvement of surgical competence of vascular anastomosis.

## References

- Williams, D., Leuthardt, E.C., Genin, G.M. *et al.* Tailoring of arteriovenous graft-to-vein anastomosis angle to attenuate pathological flow fields. *Sci Rep* 11, 12153 (2021). <https://doi.org/10.1038/s41598-021-90813-3>
- Guang, Y., Coccione, A.J., Crandall, C.L. *et al.* A multiphase model for determination of water and solute transport across the arterial wall: effects of elastic fiber defects. *Arch Appl Mech* 92, 447–459 (2022). <https://doi.org/10.1007/s00419-021-01985-3>

## Acknowledgements

This project is supported by the NSF Center for Engineering Mechanobiology CMMI-1548571. Thank you to the members of the Genin lab, especially Kenny Huang and Dr. Genin for the guidance through this project. I would also like to thank Patricia Widder and Gwen Nguyen for the support. Thank you Biorender for the use of its graphics software.



## Unraveling the Role of Formins in Podocyte Dynamics and Function

Nathalia Liu De Restrepo<sup>1,2</sup>, Shumeng Jiang<sup>2</sup>, Pongpratch Puapatanakul<sup>2</sup>, Hani Suleiman<sup>3</sup>

1. University of Puerto Rico Cayey, Dept. of Biology
2. Washington University at St. Louis, Dept. of Mechanical Engineering and Material Science
3. Division of Nephrology at Washington University School of Medicine

**Introduction:** Chronic kidney disease could progress to end-stage kidney disease which is lethal. Podocytes, with foot processes attaching to the glomerular basement membrane, play a crucial role in kidney filtration. Injured podocytes were recently found to develop sarcomeres-like structures (SLS) in response to injury, with formins likely responsible for elongation and rearrangements<sup>1</sup>. INF2, one of the formins, is widely expressed in kidney podocytes and tubules, with most mutations occurring there<sup>2</sup>., it is suggested that formin proteins like INF2 are involved in maintaining the dynamic structure and stability of podocyte foot processes and the filtration slits<sup>3</sup>. Maintaining the healthiness of podocytes and the integrity of the glomerular filtration barrier is crucial for overall kidney function, However, limited data exists on renal formins' role in podocyte dysfunction due to the hardships of studying podocytes outside of their native microenvironment, we therefore used a novel in vitro culture system of podocytes to study the functions of formins , with the use of both primary podocytes from mice and differentiated podocyte cell line, with the help of siRNA inhibition to determine their functionality in the cytoskeleton organization and maintenance of podocytes.

### Materials and Methods:

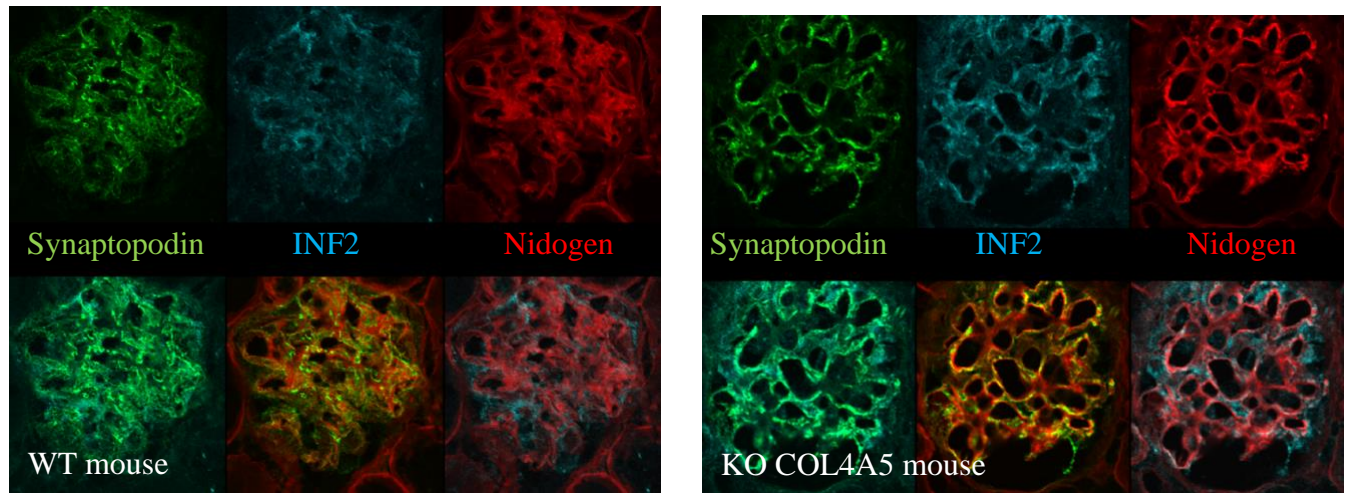
**Isolation of mouse glomeruli:** Mouse glomeruli were isolated using an established differential adhesion method with modifications. Briefly, kidneys were collected, minced, and digested. The suspension containing the dissociated kidney fragments was passed through a cell strainer and the glomeruli-enriched tissue fragments were collected on top of the 40- $\mu$ m cell strainer. These were then placed onto 10-cm tissue culture dishes to allow the segments to adhere before collecting the glomeruli left in suspension. Last, the suspension was spun down under 290g for 5 min, and the glomeruli were resuspended in primary podocyte culture medium.

**Podocyte cell line culture and differentiation;** To visualize the behavior of sarcomere like structures, podocyte cell lines were maintained at 33°C, and then incubated at 37°C for 7 days for differentiation. Last, the cells were trypsinized and seeded on glass bottom dishes for staining and imaging.

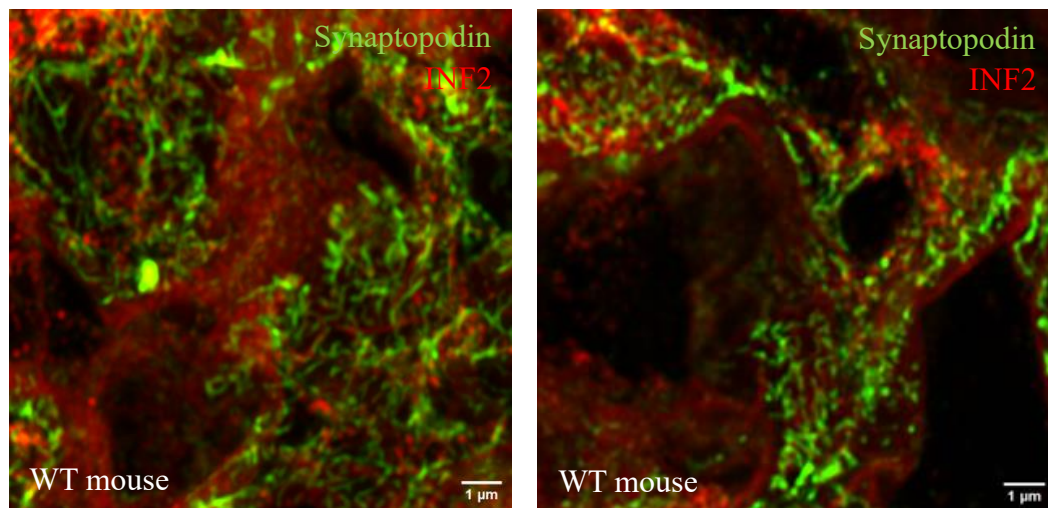
**Fluorescent staining and imaging;** Frozen mice unfixed kidney tissue was sectioned 7 micrometers thick using Leica cryostats, then were mounted on glass slides for immunostaining. The immunofluorescence staining consisted of using 2% BSA blocking solution to reduce nonspecific binding, then incubated overnight with primary antibodies, secondary antibodies were used to recognize the first antibody and its fluorescent dye for observation. Last, the samples were mounted and observed under fluorescent, confocal microscope.

SiRNA inhibition of Formins: Chemical transfection of SiRNA for INF2, FHOD3 and MDIA1 formins was employed on the differentiated podocyte cells lines using Lipofectamine 3000 Transfection Reagent to observe how silencing the formins affect the behavior of SLS's.

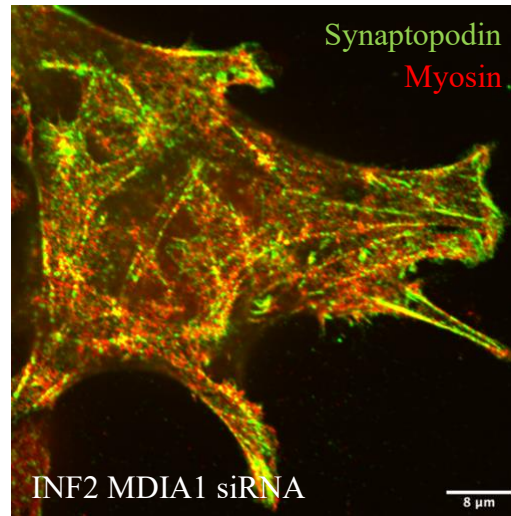
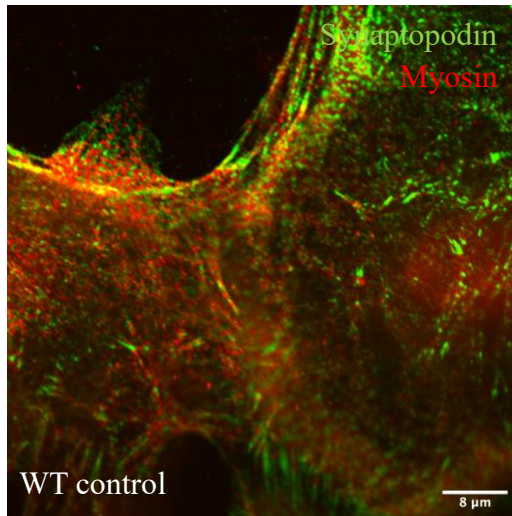
## Results and Discussion



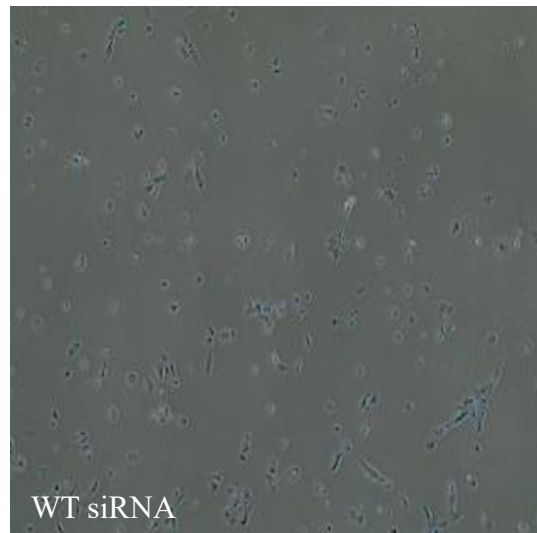
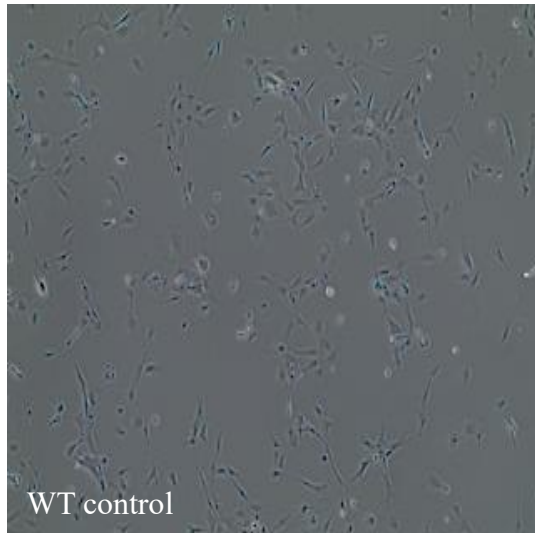
**Result 1:** Frozen mice unfixed kidney tissue was sectioned 7 micrometers thick using Leica cryostats, then were mounted on glass slides for immunostaining. Samples were analyzed under the confocal microscope to have an overview of the localization of the INF2 formin. The presence of the formin is higher in the injured tissue.



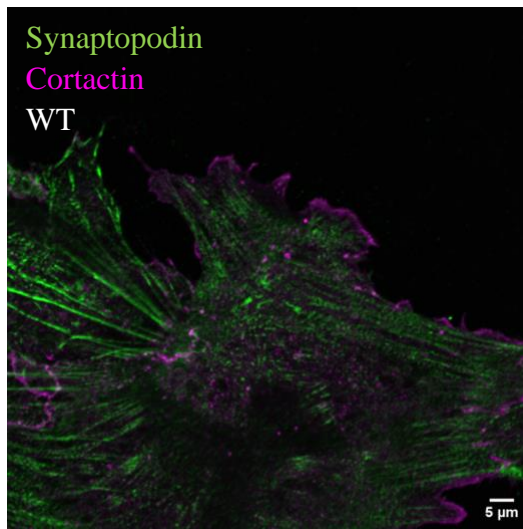
**Result 2:** After analyzing the samples in the Airyscan microscope, it is suggested that the INF2 formin is located at the periphery of foot processes.



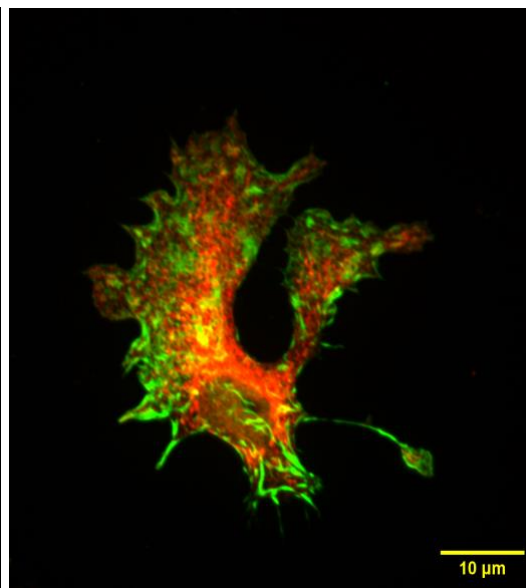
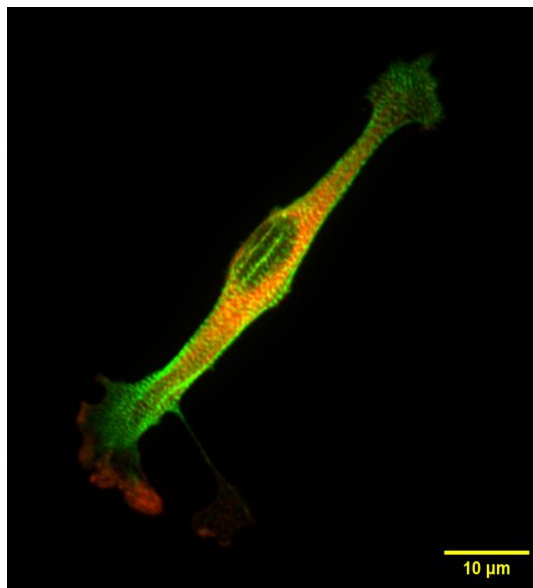
**Result 3:** After the chemical transfection of siRNA for INF2 and MDIA1 formins on differentiated podocyte cell lines, it is observed that the presence of formins in cells are not strictly required for SLSs development, meaning, that there is presence of actin-myosin arrangements even when formins are silenced.



**Result 4:** Chemical transfection of siRNA of INF2, MDIA1 and FHOD3 formins was employed in differentiated podocyte cell lines. After using the brightfield to compare the cell number, it is suggested that there is a potential role of formins in attachment as it heavily decreased in silenced cells.



**Result 5:** Chemical transfection of siRNA was employed of the INF2 formin on differentiated podocyte cell lines. Then, the samples were fixed for fluorescence staining. On the control sample, it was observed that there is a colocalization between cortactin and the INF2 formin as the cell spreads in the surface. A higher signal of INF2 was perceived whenever Cortactin, a marker for lamellipodia was present. At the same time, synaptopodin positive stress fibers were noticed to be avoiding the lamellipodia area, suggesting a potential role of INF2 for the early-stage formation of the SLSs.



**Result 6:** Primary podocytes were stained for INF2 and observed under the confocal microscope to confirm that the INF2 formin also localizes in the periphery of the cell. After using high concentration of Blebb, a myosin-actin inhibitor, the cells spreading mechanisms were heavily affected, implying a disruption of both the sarcomere-like structures and the localization of the INF2 formin.

## Conclusions

The results suggest that INF2 formin plays a role in the periphery localization of foot processes and may be involved in cell motility, early-stage SLSs formation, and cell attachment. However, the presence of formins is not essential for the development of sarcomere-like structures, as these structures can still form even when formins are silenced.

The potential of cortactin and INF2 for cell regeneration in a mechanobiological approach could be:

- **Gene Therapy:** Modulating the expression of cortactin and INF2 genes could be used to enhance or direct cell migration, proliferation, and tissue remodeling during regeneration.
- **Biomaterials Design:** Developing biomaterials that can release or interact with cortactin and INF2 could provide localized cues to promote cell attachment, migration, and differentiation at the site of tissue injury.
- **Tissue Engineering:** Incorporating cortactin and INF2 into tissue-engineered constructs may improve the functionality and integration of engineered tissues with the host tissue during regeneration.

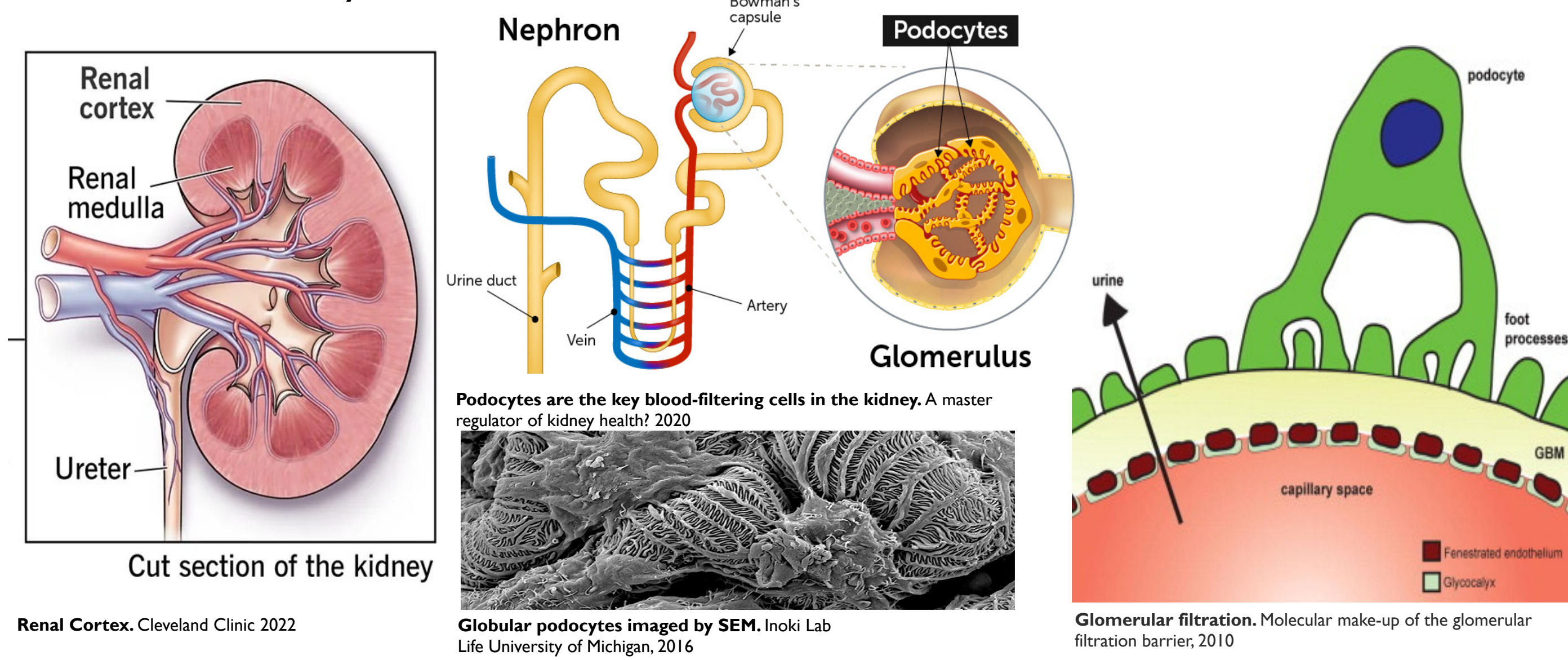
## References

1. Krendel, Mira; Pruyne, David. New Paradigm for Cytoskeletal Organization in Podocytes: Proteolytic Fragments of INF2 Formin Function Independently of INF2 Actin Regulatory Activity. *JASN* 31(2):p 235-236, February 2020. | DOI: 10.1681/ASN.2019121292
2. Gbadegesin RA, Lavin PJ, Hall G, Bartkowiak B, Homstad A, Jiang R, Wu G, Byrd A, Lynn K, Wolfish N, Ottati C, Stevens P, Howell D, Conlon P, Winn MP. Inverted formin 2 mutations with variable expression in patients with sporadic and hereditary focal and segmental glomerulosclerosis. *Kidney Int.* 2012 Jan;81(1):94-9. doi: 10.1038/ki.2011.297. Epub 2011 Aug 24. PMID: 21866090; PMCID: PMC3694501.
3. Shumeng Jiang et al., An ex vivo culture model of kidney podocyte injury reveals mechanosensitive, synaptopodin-templating, sarcomere-like structures. *Sci. Adv.*8, eabn6027 (2022). DOI:10.1126/sciadv.abn6027

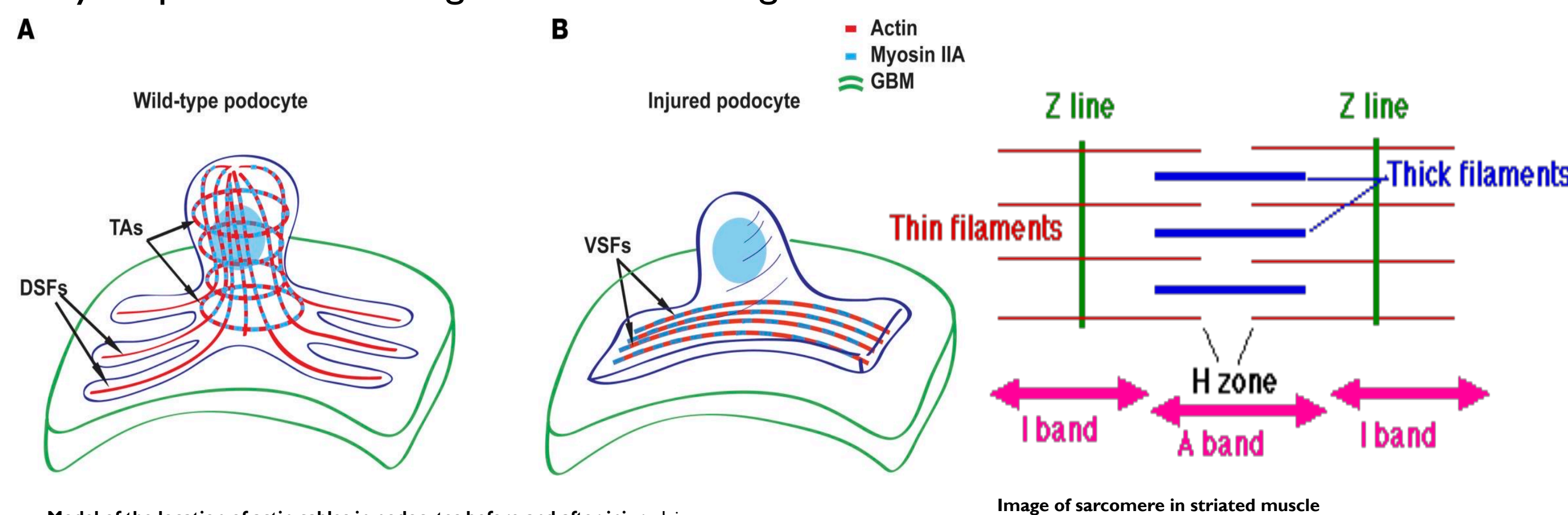
## INTRODUCTION

Chronic kidney disease could progress to end-stage kidney disease which is lethal.

Podocytes, with foot processes attaching to the glomerular basement membrane, play a crucial role in kidney filtration.

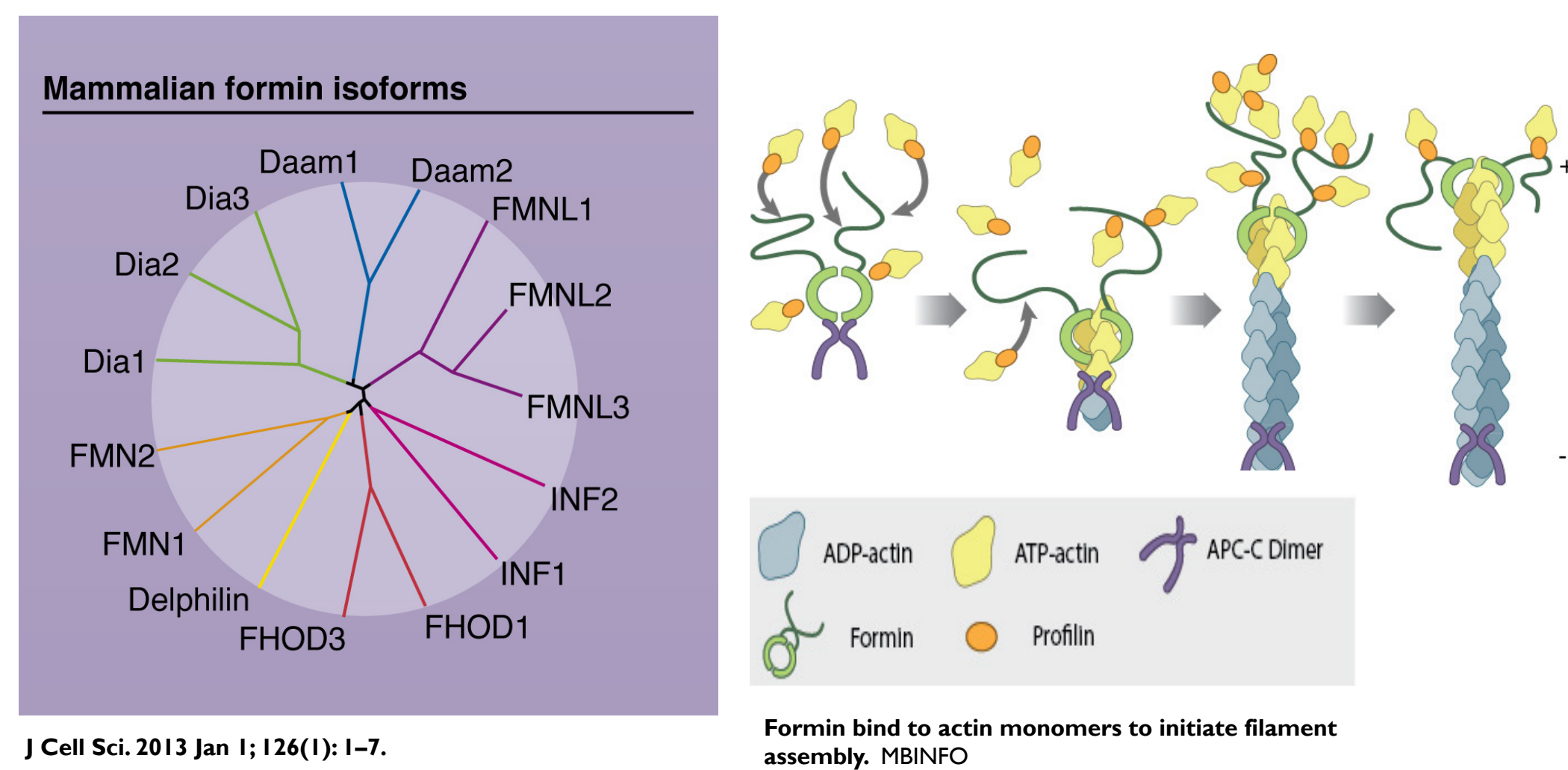


Podocytes develop sarcomeres-like structures (SLS) in response to injury, with formins likely responsible for elongation and rearrangements!

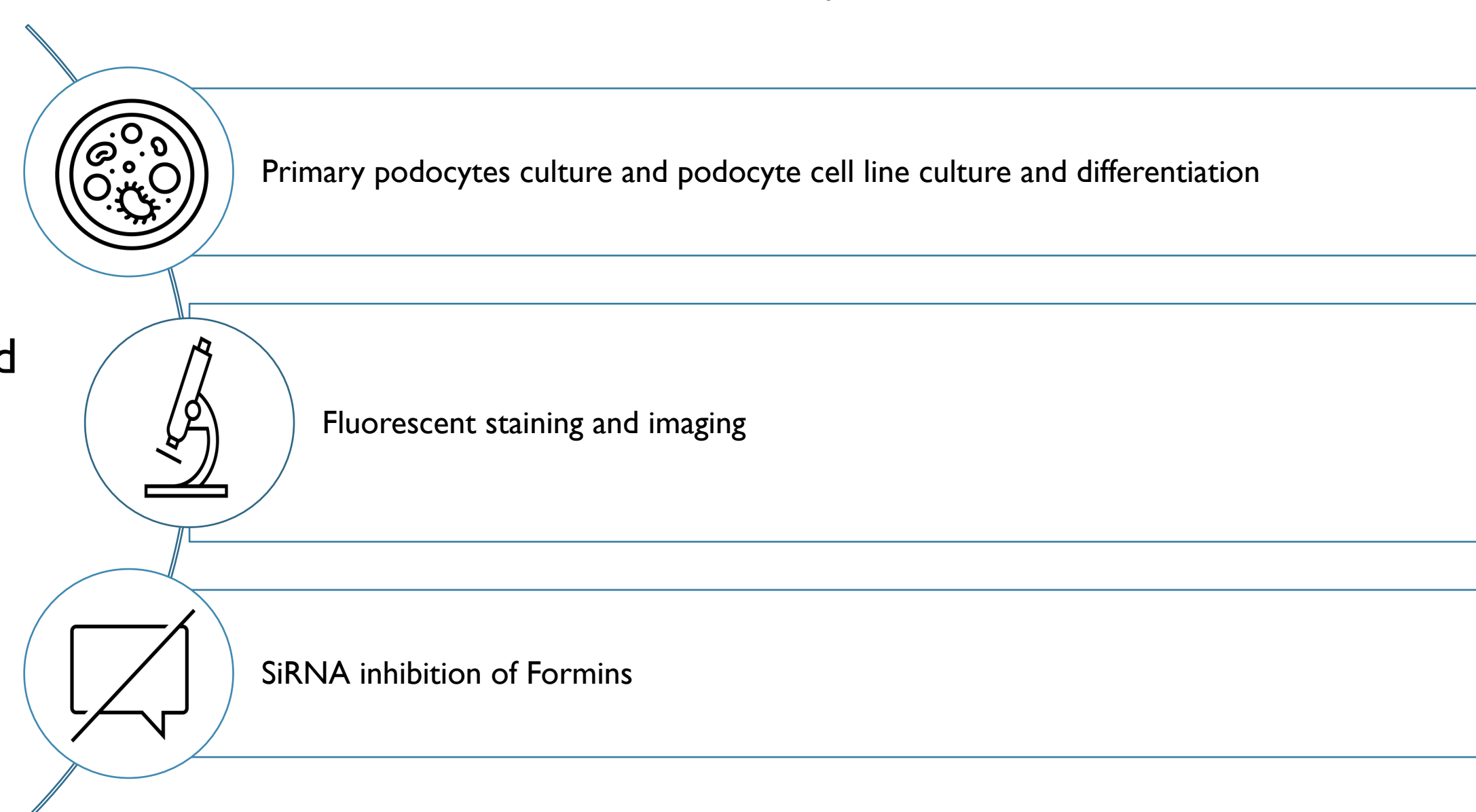


INF2, one of the formins, is widely expressed in kidney podocytes and tubules<sup>2</sup>.

It is suggested that formin proteins like INF2 are involved in maintaining the dynamic structure and stability of podocyte foot processes and the filtration slits<sup>3</sup>.



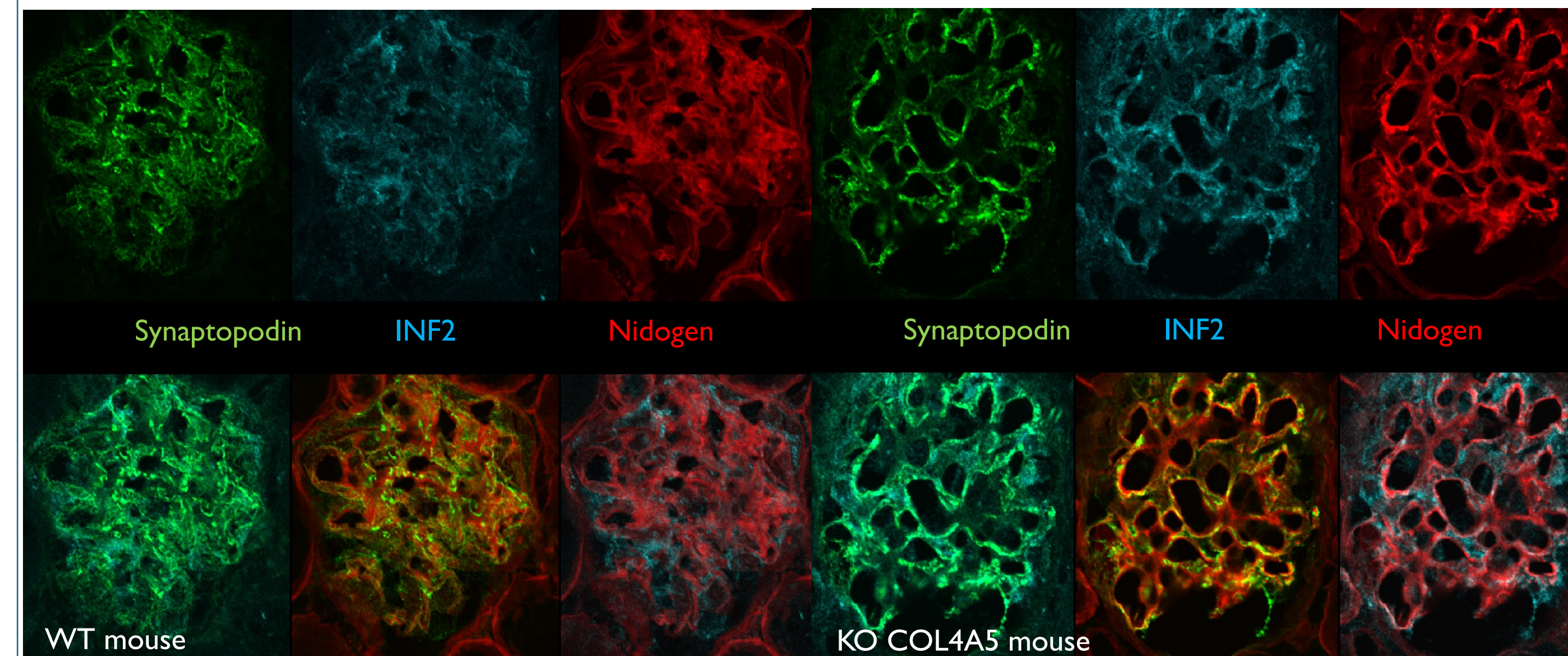
A novel in vitro culture system of podocytes was used to study the functions of formins.



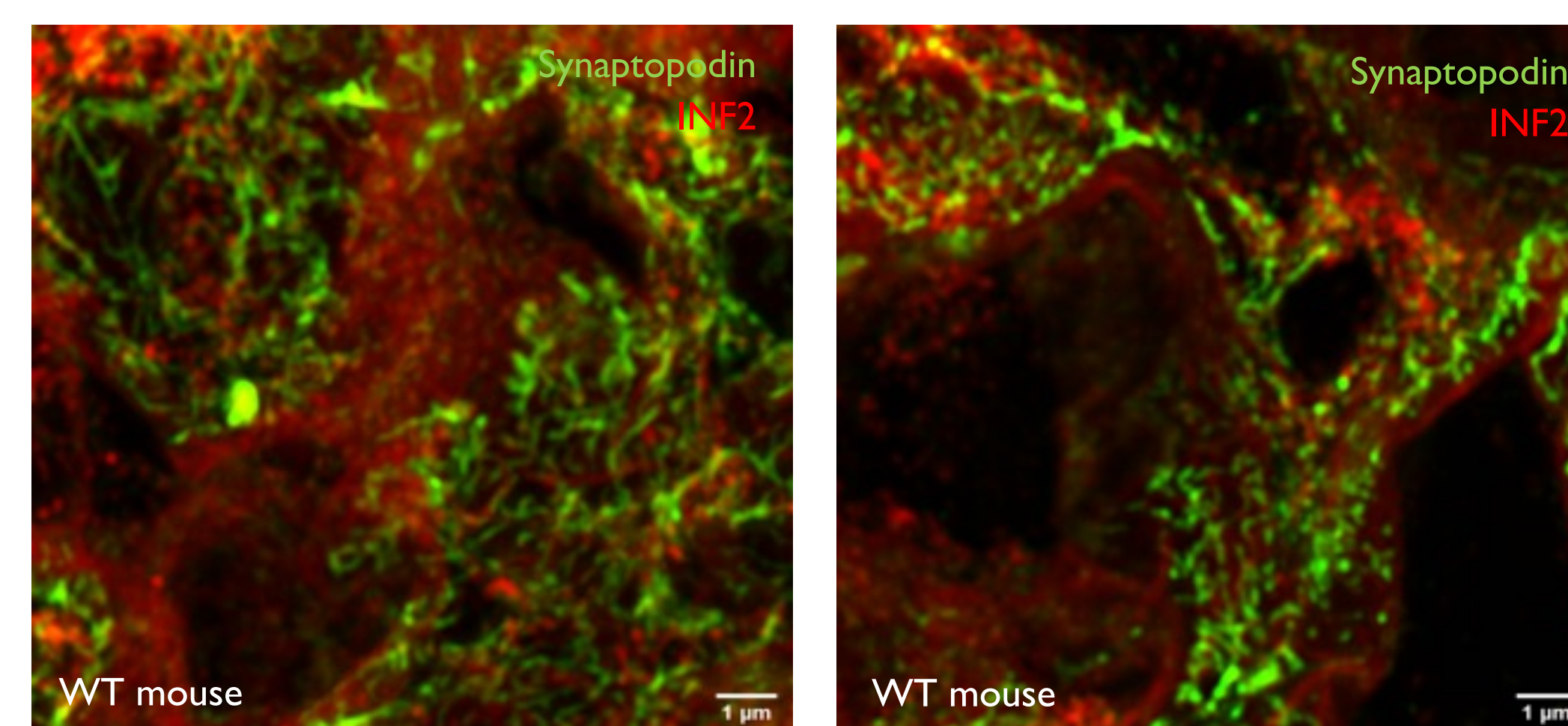
## RESULTS & DISCUSSION

### Mouse Tissue Staining

Overview of the localization of formin INF2

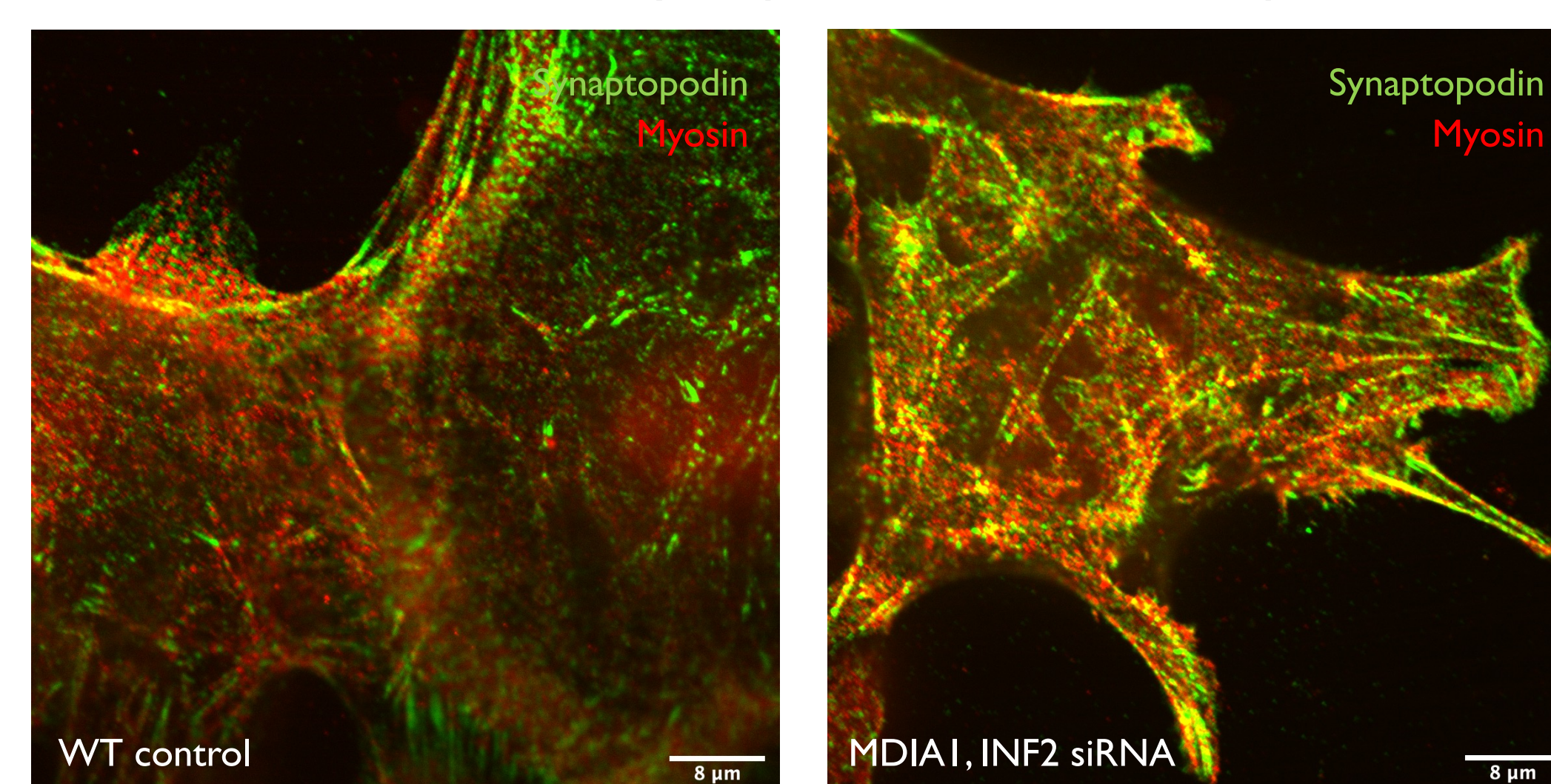


INF2 formin is located at the periphery of foot processes.

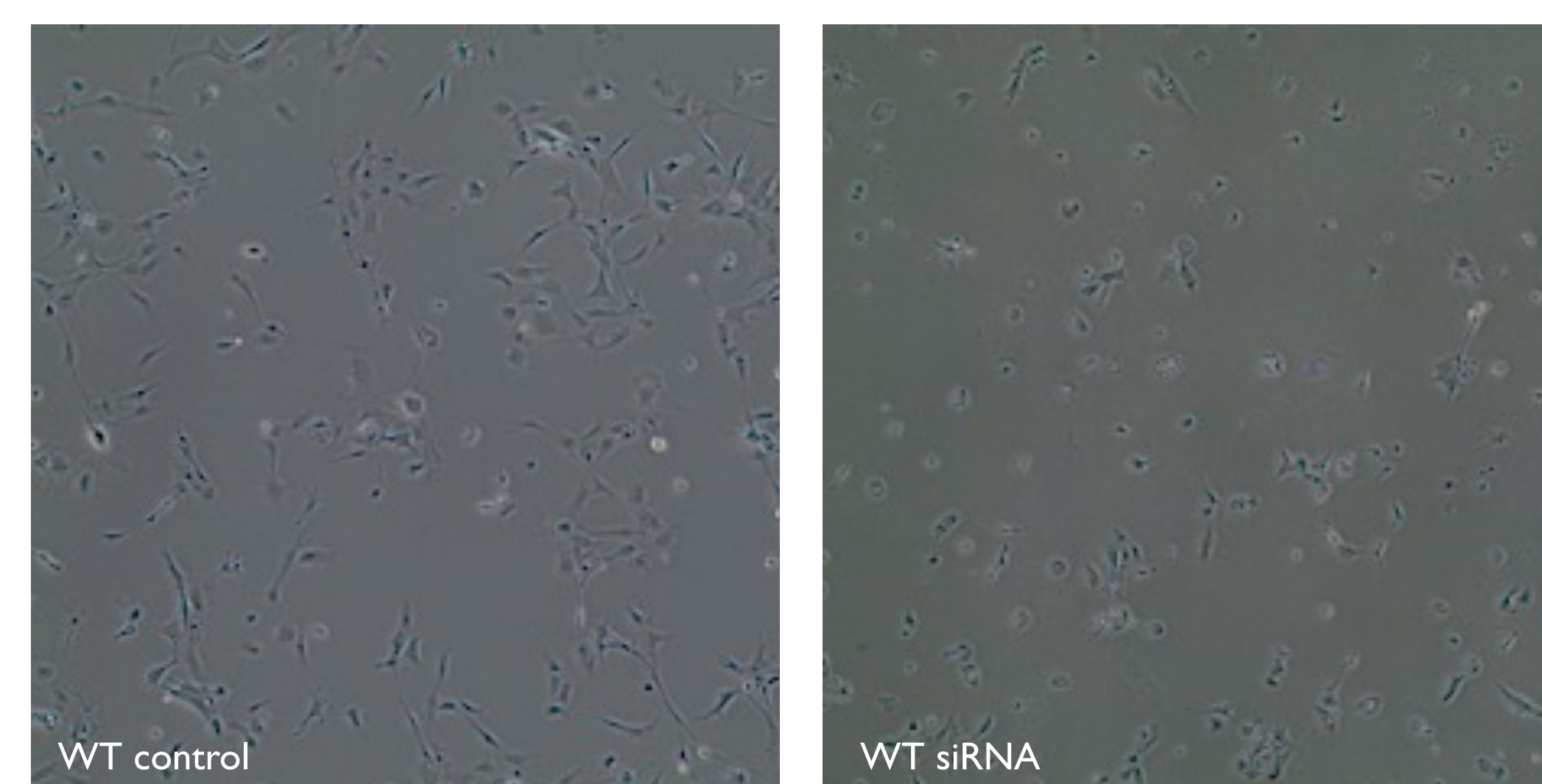


### Formin knockdown in differentiated podocyte cell line

The presence of formins in cells are not strictly required for SLSs development.



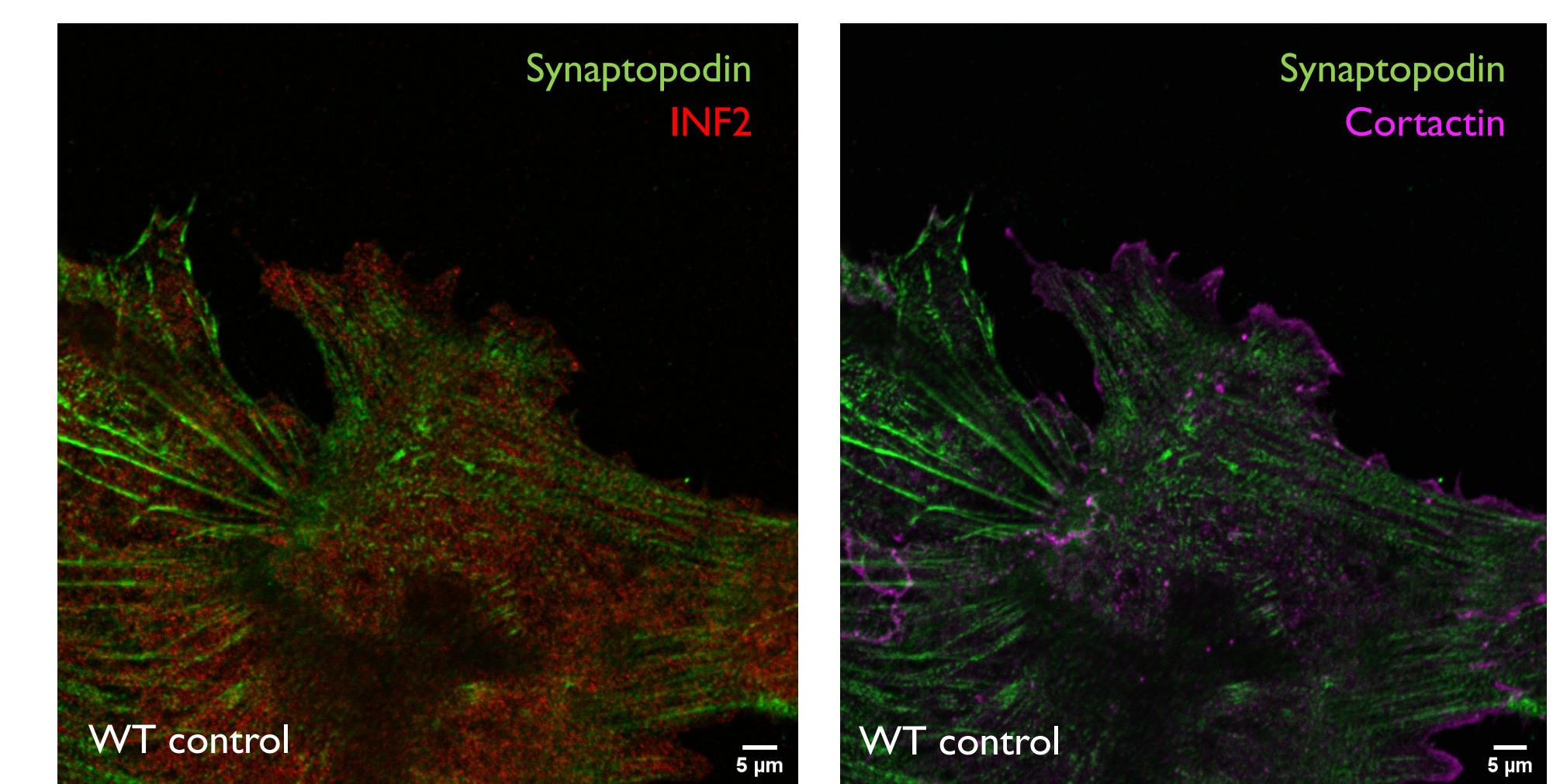
The use of siRNA for INF2, FHOD3, and MDIA1 led to a significant decrease in cell attachment.



## RESULTS & DISCUSSION

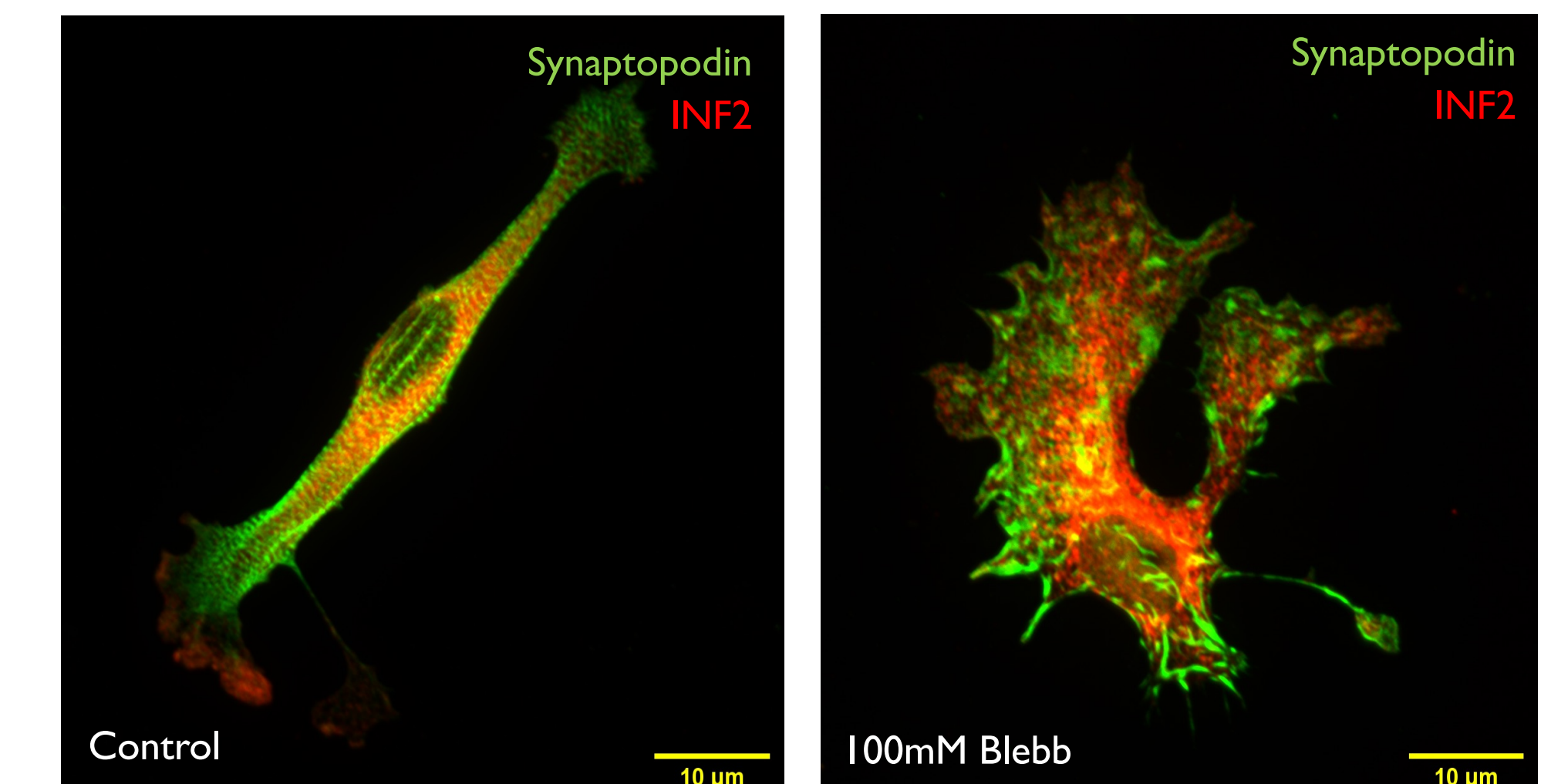
INF2 and Cortactin staining on differentiated podocyte cell line

A higher signal of INF2 was perceived whenever cortactin was present, suggesting a potential role of INF2 in cell motility and in the early-stage formation of the SLSs.



Synaptopodin and INF2 staining on primary podocytes

Primary podocytes were stained for INF2 and observed under the confocal microscope to confirm that the INF2 formin also localizes in the periphery of the cell.



## CONCLUSION

The results suggest that INF2 formin plays a role in the periphery localization of foot processes and may be involved in cell motility, early-stage SLSs formation, and cell attachment. However, the presence of formins is not essential for the development of sarcomere-like structures, as these structures can still form even when formins are silenced.

The potential of cortactin and INF2 for cell regeneration in a mechanobiological approach could be:

- Gene Therapy
- Biomaterials Design
- Tissue Engineering

## REFERENCES

- [1] Mira, K. New Paradigm for Cytoskeletal Organization in Podocytes: Proteolytic Fragments of INF2 Formin Function Independently of INF2 Actin Regulatory Activity. JASN 31(2):p 235-236, February 2020. | DOI: 10.1681/ASN.2019121292
- [2] Gbadegesin RA. Inverted formin 2 mutations with variable expression in patients with sporadic and hereditary focal and segmental glomerulosclerosis. Kidney Int. 2012 Jan;81(1):94-9. doi: 10.1038/ki.2011.297. Epub 2011 Aug 24. PMID: 21866090; PMCID: PMC3694501.
- [3] Jiang S. et al., An ex vivo culture model of kidney podocyte injury reveals mechanosensitive, synaptopodin-templating, sarcomere-like structures. Sci.Adv.8, eabn6027 (2022). DOI:10.1126/sciadv.abn6027

## ACKNOWLEDGEMENTS

We thank NSF REU grant CMM1-1548571 for this research. Additionally, we thank Kaye Brathwaite, Meei-Hua Lin, Jennifer Richardson.